# Investigating the Photodegradation of Organic Sunscreens in the Gas phase and in Solution: Towards Natural Alternatives as Means of Photoprotection

Maria Sereli

MSc (by Research)

University of York

Chemistry

January 2022

# Abstract

UV filters found in commercial sunscreens are an important group of molecules which play a key role in human health by reducing cases of melanoma. The development of better performing sunscreens is an active area of research, particularly as some sunscreens are photounstable. It is therefore important to develop new methods to measure the photostability of sunscreens and understand their photodegradation products better.

The first gas-phase study of the common UVB filter, octyl-methoxycinnamate (OMC), using laser-interfaced mass spectrometry (LIMS) was performed to probe the gaseous absorption profile and associated UV breakdown products. OMC was studied in its protonated form and displayed an absorption spectrum with increased absorption in the UVA and UVC regions, compared to the neutral species which absorbs primarily in the UVB region. Photofragmentation of protonated OMC across the UV was found to occur primarily with production of the thermal fragments that are observed upon heating of the electronic ground state. This indicates that protonated OMC decays statistically, in line with ultrafast excited state decay. A minor, photochemical photofragment was also observed, indicating that a triplet state is also being accessed following UV excitation.

The solution-phase photoproducts of OMC and 2-ethylhexyl 4-(dimethylamino) benzoate (OD-PABA) were explored using novel UVA and UVB LED photolysis cells. For OMC, the main photofragments produced match the ones identified via LIMS, indicating that it is a powerful tool for photoproduct detection. The photoproducts observed match those previously reported for the two molecules, hence validating our new methodology that has a lower energy requirement than previous ones. However, a potential, general issue was identified in the identification of photoproducts using mass spectrometry, since the collision induced dissociation experiments performed as part of this work suggest that the identified "photoproducts" are in fact thermal fragments produced during electrospray.

The thermal fragmentation and photodegradation pattern in solution for vanillin, a lignin monomer, was also explored. The solution-phase UV absorption profile of OMC-vanillin and avobenzone-vanillin mixtures was also investigated as a step towards understanding the synergistic effect between lignin and chemical UV filters. An enhancement was observed in the photostability of both organic sunscreens in the presence of vanillin.

# Contents

# List of Tables

# List of Figures

# Acknowledgements

# Declaration

I declare that this thesis is a presentation of original work and I am the sole author. This work has not previously been presented for an award at this, or any other, University. All sources are acknowledged as References.

# Chapter 1

## Introduction

### 1.1 Ultraviolet radiation and skin cancer

Exposure to ultraviolet (UV) radiation has been linked to the development of skin cancer.[1] Two common types of skin cancer are melanoma and non-melanoma, with the latter including basal cell carcinoma and squamous cell carcinoma.[2] Non-melanoma skin cancer in particular was estimated to be the 5th most prevalent type of skin cancer among men and women in 2018.[2] According to WHO,[3] there is a projected increase of 20% in the number of deaths as a result of melanoma skin cancer by 2025. UV radiation forms the high energy part of solar radiation that reaches the Earth's surface alongside visible light and infrared (IR) radiation.[4] It consists of three different components, UVA (315-400 nm), UVB (280-315 nm) and UVC (100-280 nm) radiation with UVC being the high energy component and UVA being the most abundant[5]. The ozone layer absorbs most of UVB and UVC radiation;[4] however, some manages to pass through this protective barrier and is able to access the different skin layers. More specifically, UVA radiation can get through to deeper layers of the skin compared to UVB radiation. This can lead to skin damage, skin ageing and even DNA damage, which could potentially lead to cancer.[4]

Skin pigmentation (tanning) is the human body's first reaction against the harmful effects of UV radiation.[4] Melanins are responsible for this effect, as they are able to absorb UV irradiation. There are two main types of melanins, eumelanin and pheomelanin, and they are synthesized inside melanocytes. These are found primarily in the lower level of the skin.[6] The role of sunscreen on inhibiting vitamin D synthesis has also been well-studied.[7–10] Vitamin D is synthesized in the body following exposure to UVB irradiation, when 7-dehydrocholesterol (7-DHC) is converted to 1,25-dihydroxyvitamin D [$1,25(OH)_2D$], through a series of chemical processes. This is the active form of the hormone in the body and what is measured to establish one's level of the hormone.[7] Vitamin D plays an important role in the body, as it helps regulate calcium levels and maintains bone health. Nevertheless, it has also been associated with a few diseases.[9,10]

## 1.2 Sunscreen composition and underlying mechanism

Sunscreens have commonly been used as the main artificial means of protection against UV radiation and are applied to the epidermis, the upper layer of the skin.[11] They consist of organic (or chemical) and inorganic filters, emollients, emulsifiers, photostabilisers[11,12] and possibly fragrances.[13] Chemical filters are molecules that absorb light in the UVA and/or UVB regions through $\pi \rightarrow \pi^*$ electronic transitions from the ground state of the molecule to an electronic excited state.[14,15] Once in the excited state, the species can follow three possible pathways. The first pathway involves losing the absorbed energy as heat to the surroundings (through internal conversion (IC), followed by rapid vibrational relaxation) and return to the ground state. In this case, the species is known as photostable. In the second pathway, the species breaks down or undergoes a structural change; therefore, losing the protective feature associated with its ground state electronic structure. This species is known as being photounstable. In the final pathway, the excited state species can react with oxygen or compounds found in skin to generate unwanted reactive species, such as singlet oxygen ($^1O_2$).[16] These species can be threatening for one's health, as they have been linked to conditions like lipid peroxidation, which can in turn cause tissue damage.[17,18] The filters' potential to either photodegrade or produce reactive species has generated the "sunscreen controversy", the idea that the means of protection from high energy UV rays could have a negative effect on skin.[14] Common chemical UV filters found in sunscreen formulations include cinnamate, benzophenone, *p*-aminobenzoic acid, salicylate, camphor, triazine, dibenzoylmethane, benzimidazole and benzotriazole, as well as their related compounds.[19] For the sunscreens studied in this thesis, i.e., octyl methoxycinnamate (OMC), butyl methoxydibenzoylmethane (avobenzone, AB) and ethylhexyl dimethyl PABA (OD-PABA) in particular, the maximum concentration allowed in end-product formulations is 10 %, 5 % and 8 % respectively, according to EU regulations.[20] In the US regulations differ, as the Food and Drug Administration (FDA) classifies sunscreens as over-the-counter drugs instead of cosmetics.[21] While the percentage concentration remains the same for OD-PABA, the maximum concentration allowed for the same filters is 7.5 % and 3 % for OMC and AB respectively.[22] Overall, UV filters account for 10-20 % of the sunscreen formulation and a choice of UVA and UVB filters is usually employed which allows for broader coverage against UV radiation.[12]

Inorganic filters are minerals and consist mainly of titanium dioxide ($TiO_2$) and zinc oxide (ZnO).[23] $TiO_2$ is a UVB absorber whereas ZnO is a UVA absorber so their combination in a sunscreen formulation provides effective protection against a wider range of UV radiation. In addition, both have an opaque colour and are used to improve the overall colour of the

sunscreen. These filters work by "reflecting and diffusing" UV radiation only when mixed with the other sunscreen ingredients.[16,24] The maximum concentration allowed in formulations for both filters is 25 %.[22] The use of nanoparticles (NPs) of $TiO_2$ and ZnO has become increasingly common in sunscreen formulation. Contrasting opinions on the safety of the NPs have emerged, as they can penetrate the upper layer of the epidermis (stratum corneum), as well as being integrated in hair follicles, where they can accumulate over time being potentially toxic.[24] However, other studies[25,26] suggest that the NP insertion does not occur beyond the stratum corneum and that it acts as a protective layer for the rest of the skin layers. Toxicity data[26] also show no correlation between skin damage and $TiO_2$ and ZnO insertion.

A sunscreen's efficacy is described by the sun protection factor (SPF). It is a measure of the amount of UV rays required to cause skin inflammation following sunscreen application compared to not using sunscreen.[27] According to the FDA, the UVA protection factor should constitute 1/3 of the total SPF.[24] Overall, the development of an efficient sunscreen requires the product to protect from UV radiation, be stable under UV radiation and high temperature conditions, have an appealing texture and odour, be easy to apply to prompt continuous application and meet safety regulations.[14,16]

It is therefore important to study the behaviour of sunscreen compounds on a molecular level, under UV radiation, to ensure that sunscreen formulations are designed in the most effective way and offer maximum protection against UV radiation.
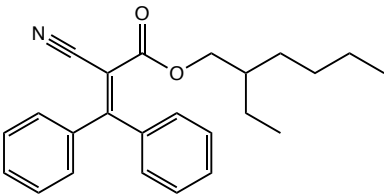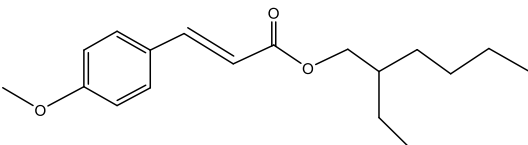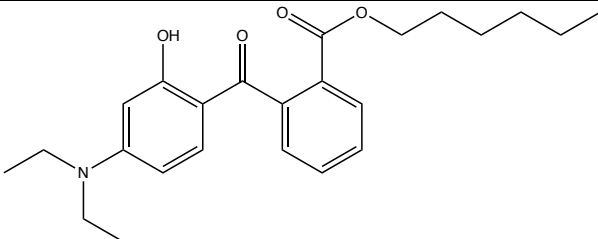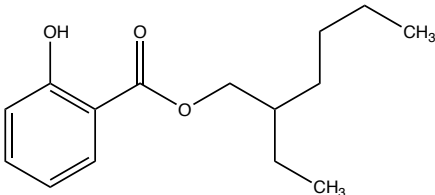
### 1.3 Using mass spectrometry to study sunscreens

### 1.3.1 Liquid chromatography-mass spectrometry

Mass spectrometry has been recognised as a powerful analytical technique.[28] Electrospray ionisation (ESI) is a soft ionisation technique used in mass spectrometry experiments.[28] In this technique, the sample in the solution phase is injected at a rate in the $\mu L\ min^{-1}$ scale. During the first stage of solvent evaporation small positively charged droplets are formed (if positive ion mode is used). This process is aided by the presence of ions such as $H^+$, $Na^+$ and $NH_4^+$. During the second stage of solvent evaporation the droplets decrease in size further (on a nm scale), while maintaining their positive charge. As a result, gaseous ions are generated that then reach the detector.[28,29] More details about ESI can be found in Chapter 2 of the thesis. Mass spectrometry combined with liquid chromatography (LC-MS)[30] have been used for the analysis of peptides,[31]

sunscreens[32–35] and other polymers.[36] In terms of sunscreen UV filter analysis in particular, LC-MS allows for the detection of various organic filters whose acid-base character may vary, as well as their potential photoproducts if combined with a UV light source.[37] In a recent study,[32] HPLC-MS/MS was used to measure the extent to which four UV filters (Table 1.1), namely octocrylene (OC), ethylhexyl methoxycinnamate (OMC), diethylamino hydroxybenzoyl hexyl benzoate (DHHB) and ethylhexyl salicylate (EHS) would permeate human skin.

**Table 1.1** Structures of UV filters used in a recent study[32] for the development and validation of an LC-MS/MS method for the determination of UV filters across human skin.

| UV filter | Structure | UV absorbance range[19] |
|---|---|---|
| OC |  | UVB |
| OMC |  | UVB |
| DHHB |  | UVA |
| EHS |  | UVB |

 Firstly, they aimed to optimise the chromatographic method they would employ, one which would result in the optimum separation, peak shape and ionisation for each UV filter. This method was used to measure the extent of permeability of these UV filters in the skin, through diffusion studies, using two commercial sunscreen lotions. A vertical Franz cell was used, with the donor compartment consisting of 2 mg cm$^{-2}$ of the sunscreen

lotion, the skin sample (more specifically the stratum corneum side) underneath, facing it, and the acceptor compartment consisting of the chosen medium. An aliquot of this medium was extracted at different time intervals (1, 2, 3, 4, 6 and 24 hours) and made into a sample for subsequent LC-MS/MS analysis. The results indicated that even after 24 hours had passed, there was a low concentration of the filters present in the acceptor sample meaning that the filters were not reaching the deeper layers of the skin, which is a positive attribute for a sunscreen product.[32]

The extent to which addition of a stabilising agent to sunscreen compounds leads to an improved photostability upon exposure to UV irradiation has also been explored. This could include another sunscreen compound or an antioxidant.[38] Herzog et al.[33] studied OMC (abbreviated EHMC in their study) mixed with octocrylene (abbreviated OCR in their study) and bis ethylhexyloxyphenol methoxyphenyl triazine (BEMT), two stabilisers, to investigate the underlying excited state processes taking place. Oil-in-water emulsions were prepared which consisted of EHMC mixed with either stabiliser and the samples were placed on quartz plates. A solar simulator was used as the irradiation source in the 290 to 400 nm range and the two plates used in each experimental run were placed on top of each other. Two kinds of experiments were carried out (labelled A and B for clarity purposes). In experiment A, using OCR as the example, EHMC and OCR were separated in the two different plates. The bottom plate consisted of EHMC (2 %) and the formulation base and the top plate consisted of the formulation base and OCR (0 %, 3 %, 6 % and 9 % respectively). Since EHMC and OCR were separated, if stabilisation occurred it would be due to energy absorption by the stabiliser. In experiment B, EHMC and OCR were combined in the bottom plate (2 % EHMC + 0 %, 3 %, 6 % and 9 % OCR respectively) and the top plate consisted of the formulation base only ("placebo" plate). In this case, if stabilisation occurred it would be due to absorption of the stabiliser or quenching or both. The type of quenching explored in this study was energy transfer. If stabilisation was improved in this experiment, then it was assumed that quenching had taken place. HPLC was used to monitor the rate of photodegradation of EHMC upon irradiation, which followed second order kinetics. Plots of EHMC photodegradation over time (h) under the two different conditions were constructed as seen in Figure 1.1. According to Figure 1.1, EHMC degrades rapidly upon irradiation without the presence of OCR. There is improved photostability upon 3% OCR addition under both experiments. A similar pattern is observed when BEMT is used as a stabiliser.[33]
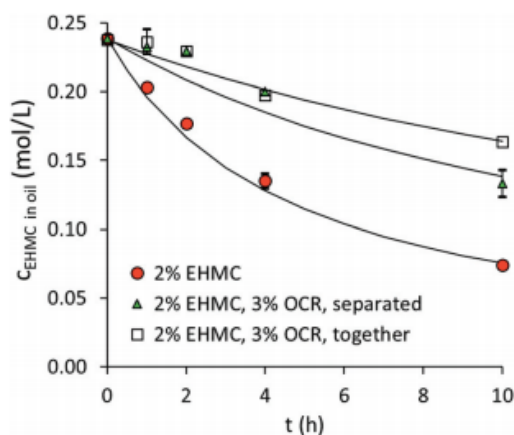
**Figure 1**.1 Degradation of EHMC with and without OCR under the two experimental conditions [Taken from Ref. 33]

Furthermore, the Jablonski diagram below (Figure 1.2) illustrates that singlet- singlet energy transfer is more efficient between EHMC and OCR compared to triplet-triplet energy transfer. Energy transfer occurs only if the amount of energy available by the photolabile species is equal to or greater than the energy required for the resulting transition to take place in the quencher molecule. Figure 1.2 shows that the energy difference between the relaxed $S_1$ state of EHMC and the $S_0$ state with $S_1$ geometry (transition indicated by the green arrow) is 342 kJ/mol. This value nearly matches the energy calculated for the transition between the $S_0$ state and the $S_1$ state with $S_0$ geometry upon excitation, for OCR (351 kJ/mol). This is not the case for the triplet-triplet energy transfer process, as the energy available at the relaxed $T_1$ state of EHMC (192 kJ/mol) is much less than the one required to excite OCR to the $T_1$ state with $S_0$ geometry (260 kJ/mol). Therefore, singlet-singlet energy transfer is more efficient between EHMC and OCR. A similar pattern is observed when BEMT is used as a stabiliser.[33]
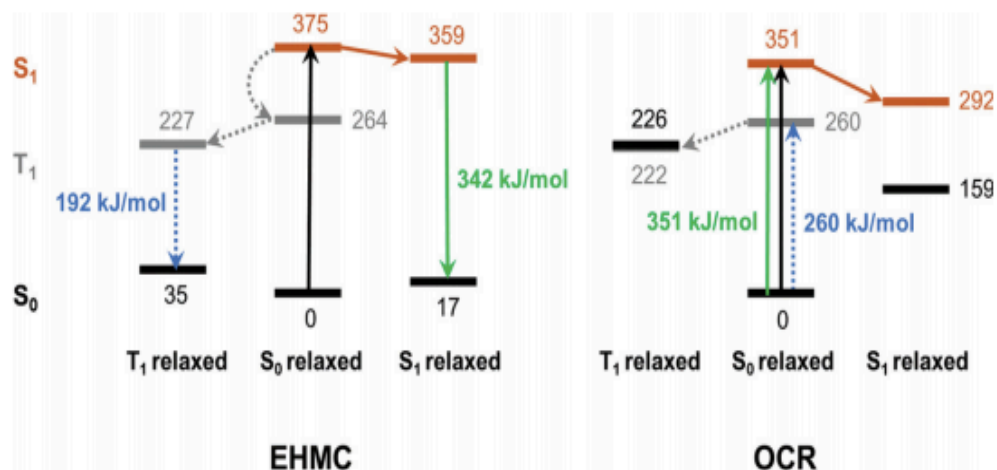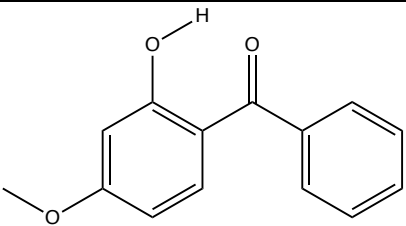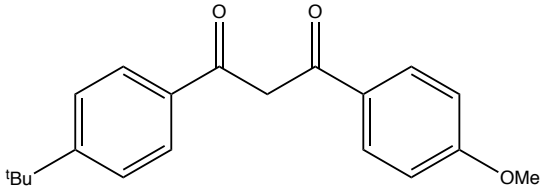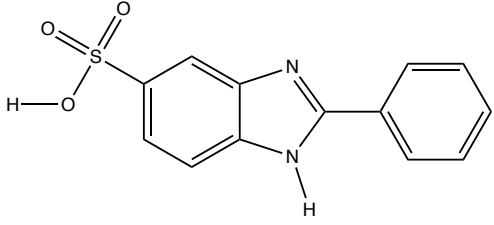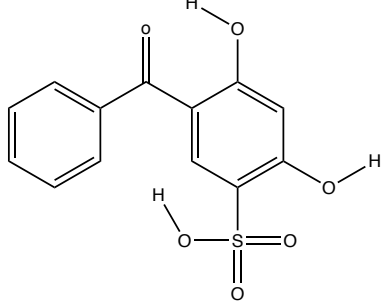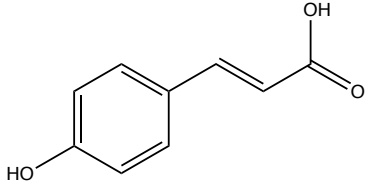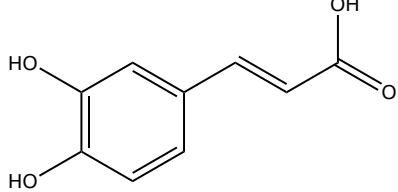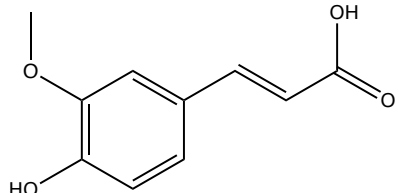
**Figure 1.2**. Jablonski diagram for the possible energy transfer taking place between EHMC and OCR. The grey colour corresponds to the excited triplet states and the brown colour corresponds to the excited singlet states. Possible singlet-singlet energy transfer is indicated by solid green arrows and triplet-triplet energy transfer is indicated by dotted blue arrows [Taken from Ref. 33].

### 1.3.2 Laser-Interfaced Mass Spectrometry

Extensive work has been carried out by our research group on the photochemistry and photophysics of various sunscreen UV filters in the gas phase, using laser-interfaced mass spectrometry (LIMS).[39–44] More details about the technique can be found in Chapter 2 and structures of the filters studied are included in Table 1.2. The experimental set up allows for selected ions, produced by electrospray, to be isolated in the ion trap of a mass spectrometer, where they can be studied without the influence of the solvent or other components of the sunscreen product.[39] The effect of pH on the absorption profile of oxybenzone (OB) was studied.[39] Protonated OB $[OB + H]^+$ showed a slight shift in the UVA absorption region in the gas phase towards higher wavelengths, compared to the equivalent absorption spectrum of the compound in acidic conditions in solution. However, deprotonated OB $[OB - H]^-$ showed decreased absorption in the gas phase in the region of 330-370 nm compared to the neutral species. The fragmentation pathways for both $[OB + H]^+$ and $[OB - H]^-$ were also explored and were significantly different. More specifically, the researchers drew attention to the production of free radicals as photoproducts of $[OB - H]^-$, which leads to questions around the use of OB as a sunscreen agent under alkaline conditions, as such species can lead to cell damage.[23]

Given that non-radiative relaxation to the ground state of OB following UV excitation takes place through a H-atom transfer in the excited state,[45] the effect of coordination of metal ions, namely $Na^+$, $K^+$ and $Rb^+$, on the relaxation mechanism was studied[42] since these ions could be expected to affect the electronic excited state in a similar way to a proton. Indeed, the presence of $Na^+$ affected OB's relaxation mechanism, as it replaced the H atom in the intramolecular bond. Infrared multiple photon dissociation (IRMPD) spectroscopy was also used in this experiment to characterise the geometric structures. Similar experiments have been carried out for AB[41] and 2-phenylbenzimidazole-5-sulfonic acid (PBSA).[40] Recently, the group have worked on the electronic relaxation dynamics of the UV filter benzophenone-4 (BP4) in its deprotonated form,[43] showing that it behaves as an efficient UV filter, even in the deprotonated form. Lastly, the deprotonated forms of the antioxidants trans-para coumaric acid (CMA), trans-caffeic acid (CA) and trans-ferulic acid (FA) have also been studied via this method and it was concluded that they can be effective as UV filters since rapid nonradiative excited state decay is maintained in their deprotonated forms.[44]

**Table 1.2** Structures of UV filters already studied by Dessent and co-workers.[39–44]

| UV filter | Structure | UV absorbance range |
|---|---|---|
| OB |  | UVA, UVB[39] |
| AB |  | UVA[41] |
| PBSA |  | UVB[40] |
| BP4 |  | UVA, UVB[43] |
| CMA |  | UVA. UVB[44] |
| CA |  | UVA, UVB[44] |
| FA |  | UVA, UVB[44] |

## 1.4 Natural sunscreens

Much effort has been made, over recent years, to investigate the potential of natural alternatives as sunscreens.[23,46] Lignin is a biopolymer that is readily available on Earth.[14,47] It plays an important role in plants, as a structural component, as well as in water transport and protection from microorganisms.[14] It has recently gained attention as a potential natural alternative to chemical UV filters used in sunscreen formulations, as it is easily accessible as a waste product from biomass processing, pulp and the paper industry.[48] In addition, its structural characteristics, namely its high phenolic and ketone content and its ability to form intramolecular hydrogen bonds make lignin appropriate for use as a UV filter.[49] Research has shown that a synergistic effect might exist between lignin and chemical UV filters which enhances UV absorption of the mixture. Qian et al.[49] made this observation while studying mixtures of organosolv lignin (OL) with either AB or OMC. This appears to arise from $\pi$-$\pi$* stacking of the aromatic rings in the lignin and the UV filter. Two types of interaction can take place known as J and H aggregates.[49,50] For a J aggregate to form, the tilt angle between the molecular axis that connects the chromophores and the transition dipole moment needs to be lower than 54.7°. The H aggregate will form if the angle is greater than 54.7°. While OMC absorbs primarily in the UVB region of the electromagnetic spectrum, formation of the J aggregate leads to lowering of the energy for the $\pi$-$\pi$* transition in the OL-OMC mixture and the mixture showed absorption in the UVA area as well. Therefore, UV absorption is improved. The researchers also reported that following 2 hours of irradiation, UV absorption increased further suggesting that additional conjugated compounds were formed.[49,50] To further the application of lignin in cosmetics, the potential incorporation of lignin nanoparticles in formulations is also being investigated by researchers.[23,48]

Sinapoyl malate (SM) is another compound found in plants that acts as a natural UV absorber.[4,51] SM (Figure 1.3) is an ester derivative of synaptic acid[51] and protects leaves from UV radiation.[52] Research has shown that the mechanism followed by SM in solution, following UV excitation, is *cis-trans* isomerisation, as the molecules return from the $\pi\pi$* excited state to the ground state *via* ultrafast IC.[4,52]
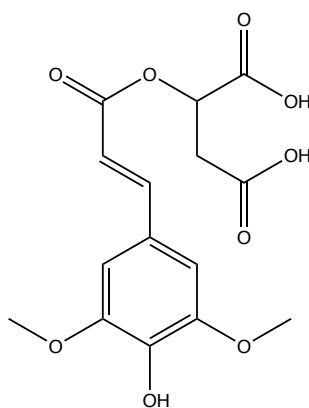
**Figure 1.3** Structure of sinapoyl malate (SM)[51]

Transient electronic absorption spectroscopy (TEAS)[4] has been used to detect changes in the electronic states exhibited by molecules in the solution phase. A variation of this method also exists, namely transient vibrational absorption spectroscopy (TVAS), which uses probe pulses with wavelengths in the IR region of the electromagnetic spectrum and allows the monitoring of bond formation and breakage. TEAS involves the use of a pulse-probe setup where ultrashort pulses are generated which last less than 100 fs. The pump pulse is used to excite a molecule at a specific wavelength. For sunscreen filters, in particular, this wavelength is in the UV region. A probe pulse of wavelengths between 300 and 800 nm is also used to measure the UV-Vis excited state absorption spectrum of the selected species. A dynamic absorption spectrum can be recorded by altering the time the probe pulse reaches the sample after the pump pulse. The time delays ($\Delta t$) vary and include nanoseconds in very small steps of even 10 fs. The transient absorption spectrum is generated by calculating the change in optical density ($\Delta OD$), as a result of transmission values taken at different pump-probe time delays. A few processes are involved in changing the optical density, namely ground-state bleach, stimulated emission, excited-state absorption and photoproduct absorption. The first two processes result in a negative $\Delta OD$ signal, whereas the remaining two in a positive $\Delta OD$ signal. A 1mM solution of SM[4] was prepared in dioxane, acetonitrile (ACN) and methanol. Based on its absorption spectrum, a wavelength of 330 nm ($\lambda_{max}$) was selected as the wavelength of photoexcitation. The probe wavelengths ranged from 335 to 675 nm over various pump-probe time delays with a maximum $\Delta t$ of 2 ns. The TEAS spectrum presented various features linked to the parameters that affect $\Delta OD$ listed above. For quantitative interpretation of the spectrum, global non-linear regression analysis modelling was used in order to extract the lifetimes ($\tau$) of the processes that are occurring and determine which physical process corresponds to each lifetime. Three lifetimes were extracted for all solvents and the suggested mechanism for the relaxation of SM was as follows:

photoexcitation of SM led to the formation of a $1^1\pi\pi^*$ excited state then $\tau_1$ (fs) described the geometry relaxation that followed outside of the Franck-Condon window. $\tau_2$ (ps) described the move to a $2^1\pi\pi^*$ after a conical intersection (CI). Finally, $\tau_3$ (ps) described the return of excited molecules to the ground-state trans isomer through CI, releasing heat to the surroundings. A few of the excited SM molecules could be "trapped" in a long-lived cis isomer, which had also been identified as the photoproduct in the mechanism. Therefore, this mechanism highlights that SM fulfils the conditions of a UV filter and has the potential to be used in a sunscreen formulation.[4] In a recent study[52] by the same research group, the effect of the size of added substituents on SM's relaxation pathway was also investigated. Sinapoyl L-dimethyl malate (SdiMM), sinapoyl L-diethyl malate (SdiEM) and sinapoyl L-di-t-butyl malate (SdiTBM) were used in addition to SM, seen in Figure 1.4. The results showed that the size of the substituent did not affect the relaxation pathway which showed a high degree of conservation for these types of molecules.
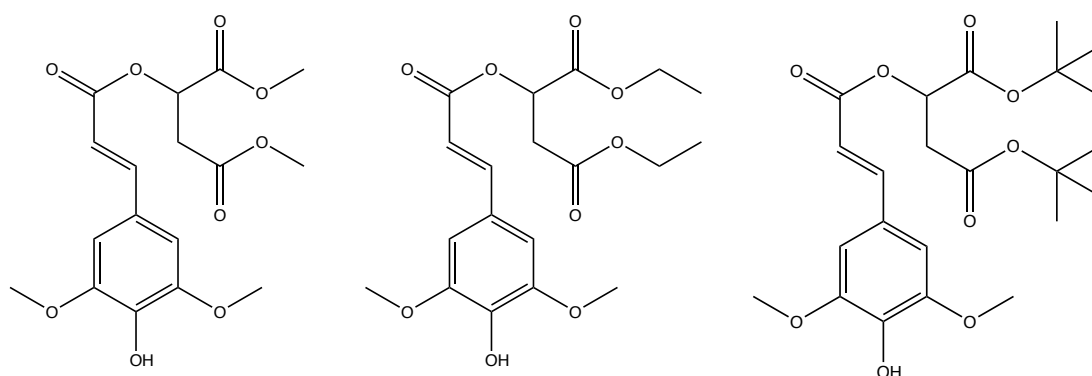


**Figure 1.4** Structures of Sinapoyl L-dimethyl malate (SdiMM, left), sinapoyl L-diethyl malate (SdiEM, middle) and sinapoyl L-di-t-butyl malate (SdiTBM, right) used in the study.[52]

**1.5 Thesis overview**

This thesis aims to build upon the high-quality research reviewed in this introduction by investigating the photodissociation of two sunscreen UV filters and looking into natural alternatives.

Chapter 3 will focus on OMC in further exploring the *cis-trans* isomerisation pathway followed upon exposure to UV radiation. Gas phase data on the protonated form of OMC are presented, obtained through LIMS, in addition to lower (CID) and higher (HCD) energy collisional induced dissociation data that give an insight into the thermal fragmentation pathway of the filter. A comparison between the two sets of fragments allows to determine whether potential harmful species are created upon photoexcitation for the protonated form of OMC.

Chapter 4 will focus on photolysis data collected under UVB irradiation for OMC and octyl dimethyl PABA (OD-PABA) in the solution phase. This chapter aims to discuss the extent to which the method followed is appropriate for detection of photoproducts in solution derived from the two filters, using ESI mass spectrometry. CID and HCD data for the identified cyclodimer of OMC in solution are also presented. Thermal fragmentation data for OD-PABA are also presented for comparison.

Lastly, Chapter 5 will focus on vanillin, one of the building blocks of lignin. CID and HCD data will be presented to determine the thermal fragments of the molecule. Photolysis data under UVB irradiation are also presented. In addition, the extent to which vanillin can act as a stabilising agent when combined with known photounstable filters, AB and OMC, will be explored. Solution-phase UV-Vis absorption spectra of vanillin and of mixtures of OMC/Vanillin and AB/Vanillin are presented and their absorbance monitored under UV irradiation.

# Chapter 2

## Experimental techniques

### 2.1 Introduction

The study of the sunscreen filters included in this thesis was possible through the combination of the experimental techniques described below. Solution-phase absorption spectra were recorded for all compounds and mixtures using UV-Vis spectrophotometry. Their absorbance was also monitored over time under exposure to UVA or UVB irradiation. Electrospray ionisation (ESI) mass spectrometry was used to produce the gas phase ions studied. Then, CID and HCD data were collected to determine the thermal fragmentation pattern of the molecules. Solution-phase photolysis data were also analysed using mass spectrometry, by irradiating a sample in a home-built photolysis cell and then using the mass spectrometer as a detector for possible photoproducts. Lastly, LIMS was used to obtain the gas-phase absorption and photoproduct production spectra of OMC.

### 2.2 Electrospray Ionisation Mass Spectrometry

Electrospray ionisation (ESI) is an atmospheric pressure soft ionisation technique used to convert species in the solution phase into ions in the gas phase.[29] It is described as soft, as it generally causes very little fragmentation.[28] ESI-MS was first developed by Dole and co-workers, who aimed to study polymers like polyethylene.[53] During the process (Figure 2.1), the solution is injected into a metal capillary at a rate of several μL min$^{-1}$. There is an electric potential of several kV in the capillary.
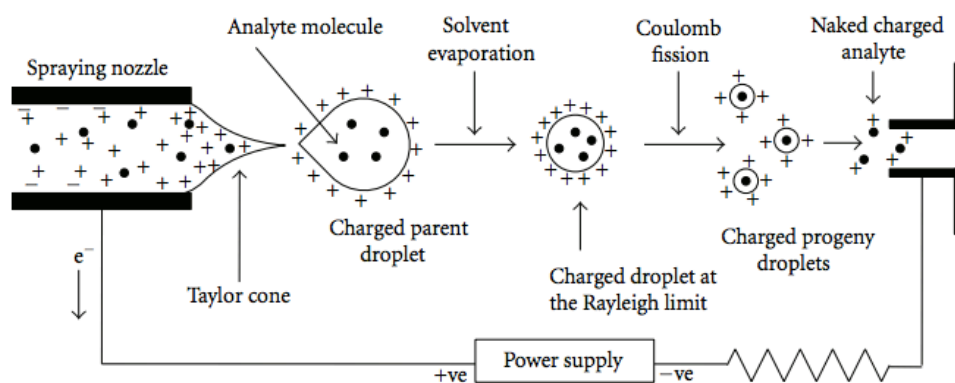


**Figure 2.1** Scheme showing the ESI mechanism for the production of gaseous ions detected by the mass spectrometer [Taken from Ref. 54].

During the first stage of solvent evaporation, the solution takes the form of a Taylor cone from which small positively charged droplets are formed (if positive ion mode is used), as a result of the very high electric field. The size of these droplets is a few micrometres. The droplets have a positive charge as a result of the presence of ions such as $H^+$, $Na^+$ and $NH_4^+$. Protons are usually accountable for the positive charge, not only because some solutions are acidic, but also as a result of redox reactions that take place inside the capillary, such as $2\ H_2O \rightarrow 4\ H^+ + 4\ e^- + O_2$.[28] The flow of a coaxial drying gas ($N_2$) also helps droplet formation, as well as guiding the electrospray into the instrument.[54] During the second stage of solvent evaporation, the droplets decrease in size further, as their increased charge density causes them to reach the Raleigh limit which is described by Equation 2a,[28] where $z_R$ is the number of elementary charges e, R is the radius of the droplet, $\varepsilon_0$ is the vacuum permittivity and $\gamma$ is the surface tension:

$$z_R = \frac{8\pi}{e}\sqrt{\varepsilon_0 \gamma R^3} \quad (2a)$$

Repetition of this process leads to the production of droplets with sizes in the nanometer range, from which gaseous ions that are in turn detected by the mass spectrometer are produced.[28,54,55]

Different mechanisms have been proposed for the formation of the gaseous ions that are formed from the nanosized droplets, namely the ion evaporation model (IEM)[56] and the charged residue model (CRM).[28,54] IEM is believed to take place when studying small samples;[57] therefore, it is assumed that this process is followed for the sunscreen filters studied. CRM, on the other hand, has been linked to the study of larger species, such as proteins.[54] More specifically, in the IEM model, gaseous ions are ejected by the droplets due to the very high electric field, formed as a result of the high charge density of the droplets.[28,54–56]

## 2.3 Quadrupole Ion Trap Mass Spectrometry

An amaZon SL dual funnel electrospray ionisation quadrupole ion trap (ESI-QIT) mass spectrometer (Bruker Daltonics, GmbH, Germany) was used. The trap consists of four parallel cylindrical metal rods. Two of the opposite rods have the same polarity (eg. positive) and the remaining two have negative polarity. They also have a constant potential 'U' and an alternating RF potential Vcos($\omega$t), where 'V' is the amplitude and '$\omega$' the frequency of the applied potential RF, which changes periodically. Once injected from the source, the ions travel through the rods via oscillations which are determined by

the values of V and U. Varying these values, allows for ions with a specific m/z to achieve the central trajectory that will lead them to the detector, while other ions hit the quadrupoles and do not get detected. By changing the applied RF, ions with different m/z values get detected and the mass spectrum is produced.[58–60]
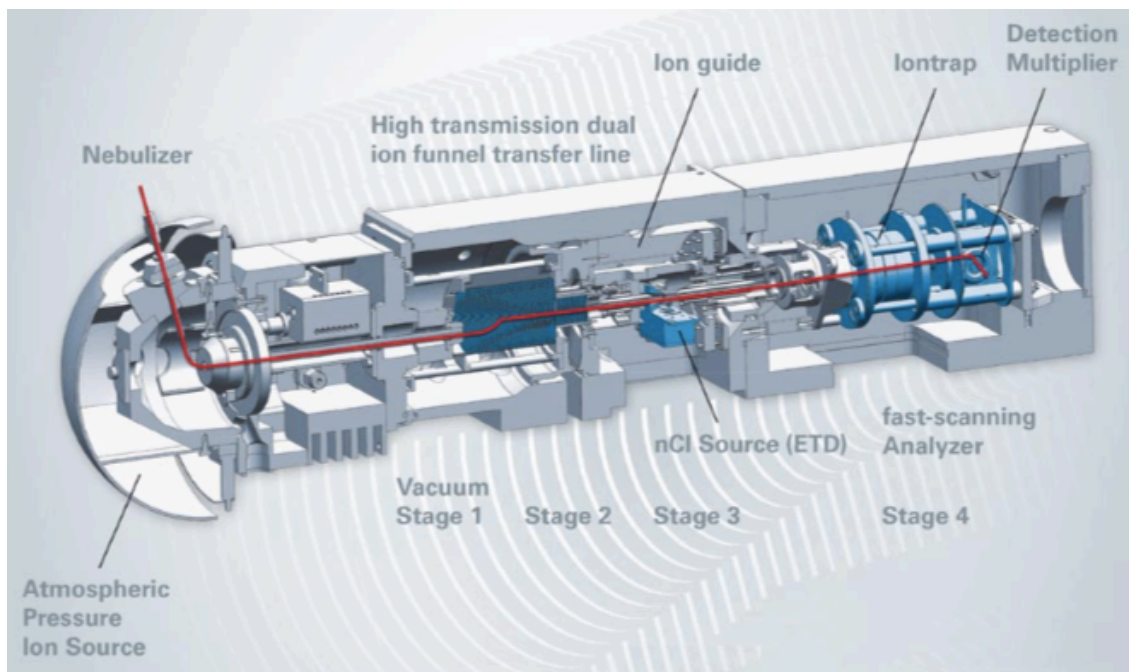


**Figure 2.2** Detailed diagram of the Bruker amaZon quadrupole ion trap (QIT) mass spectrometer used [Taken from Ref. 61].

## 2.4 Laser Interfaced Mass Spectrometry (LIMS)

The Bruker amaZon mass spectrometer outlined above was used to record the action spectra presented in Chapter 3 and it was modified so that a laser beam could pass through the ion trap. The details of the modifications made have been previously outlined.[62] Figure 2.3 summarises the experimental set up.
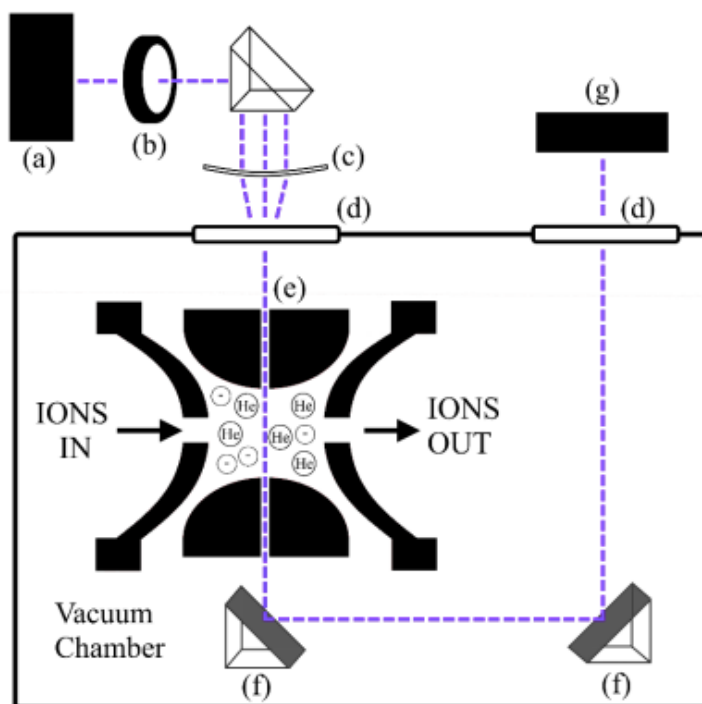
**Figure 2.3** Diagram of the experimental set up that allows for LIMS to take place [Taken from Ref 62). The modifications made to the amaZon mass spectrometer are also visible.

More specifically, Figure 2.2 shows a 10 Hz Nd:YAG (Surelite™, Amplitude Laser Group, San Jose, CA, USA) pumped OPO (Horizon™, Amplitude Laser Group) tuneable laser (a) as the photon source, giving ~ 0.1-0.4 mJ of energy between 215-400 nm (3.10-5.75 eV) for the sunscreen filters studied.[39] An optical shutter (b) (Model SH05, Thorlabs Inc), a 200 mm focal length UVFS lens (c) (LE4467-UV, Thorlabs Inc), a pair of flange mounted uncoated UVFS windows (d) (WG41050, Thorlabs Inc) and a pair of mirrors (f) are also part of the set up. The 2 mm hole drilled through the ring electrode of the ion trap allowing the laser pulse to pass through is shown (e) and finally a UV-Vis spectrometer (g) (USB2000+ UV-VIS, Ocean Optics Inc)is also used.[62]

The amount of ions available in the gas phase is much smaller compared to the amount of ions available in solution so direct measure of the gas phase absorption spectrum of a selected species is not possible. Therefore, gas-phase spectra are acquired by action spectroscopy, i.e. fragmentation of the parent ion which is detected as a function of photon energy. The following procedure is used to obtain the spectral data. The intensity of the parent ion isolated in the trap is measured with the laser turned off. Then, the laser is turned on and the intensity of the parent ion is measured again. In the second measurement, the ion intensity is expected to be lower, as the parent ion might

photofragment following photon absorption. The photofragments are also detected by the mass spectrometer. Repetition of this process over the chosen wavelength range leads to the gas-phase absorption (photodepletion) spectrum of the parent ion and associated absorption spectra of any photofragments produced. Measurements are taken usually every 2 nm.

Equations 2b,[62] 2c[62] and 2d[62] below are used to determine the photodepletion (PD) and photofragment (PF) intensities, where $I_{OFF}$ and $I_{ON}$ are the intensities of the parent ion recorded when the laser is off and on respectively, $I_{FRAG}$ is the intensity of the photofragment with the laser on, $I_{PFT}$ is the sum of the photofragment ion intensities with the laser on, $\lambda$ is the wavelength (nm) and P is the laser pulse energy (mJ):

$$Photodepletion\ Intensity\ (PD) = \frac{\ln\left(\frac{I_{OFF}}{I_{ON}}\right)}{\lambda \times P} \qquad (2b)$$

$$Photofragmentation\ Intensity = \frac{\left(\frac{I_{FRAG}}{I_{OFF}}\right)}{\lambda \times P} \qquad (2c)$$

$$Relative\ Ion\ Yield = I_{FRAG}/I_{PFT} \qquad (2d)$$

Data collection takes place using LabView while Bruker Daltonic's Data Analysis and Automation Engine software are used for data extraction. A python script is also used that controls the automated data analysis process. The intensity of the photofragments is normalised with respect to the parent ion during data processing.

## 2.5 Collision-Induced Dissociation

Tandem mass spectrometry (MS/MS) allows for selected ions to undergo different stages of mass analysis.[54] Low-energy collision induced dissociation (CID) is used to monitor the fragmentation pattern of a chosen species (precursor ion).[63] It is a unimolecular fragmentation process, where the precursor ion collides with an inert gas (eg. helium) in the trap; thus, increasing its internal energy. This results in fragments being produced by the precursor ion by either homolytic or heterolytic cleavage.[54] The user can set how strong the collision will be by varying the amplification over time, while setting up the experiment. In quadrupole (QIT) ion traps, the kinetic energy can be increased to a level that allows the ion's trajectory in the trap to remain stable, as discussed above.[54] An HCT

ultra ETD II mass spectrometer (Bruker Daltonics, Germany) was used to collect the CID data presented in this thesis.

Higher energy collision induced dissociation (HCD) was also used to determine the secondary fragments produced by the precursor ion, as well as distinguishing further between the thermal fragments and photofragments obtained by the action spectra.[40] A mass spectrometer with an Orbitrap mass analyser was used (in the experiments outlined in Chapters 3 and 4 a Thermo Fisher Orbitrap Fusion™ mass spectrometer is used). A C-trap exists as part of the instrument which lies closest to the mass analyser and collects the ions for optimisation before injecting them into the mass analyser in the form of ion packets. HCD takes places in a separate compartment, where the fragments are produced , which allows for higher kinetic energies to be attained compared to lower-energy CID.[64,65]

## 2.6 Photolysis apparatus

Solution-phase photolysis experiments were carried out using an HCT ultra ETD II mass spectrometer (Bruker Daltonics, Germnay). The method is described in more detail in Chapter 4. Solutions of the filters were irradiated using two photolysis cells consisting of light-emitting diodes (LEDs) of wavelengths in the UVA (365 nm) or the UVB (310 nm) region. The UV-Vis absorption spectrum was recorded first using a Thermo Genesis 180 UV-Vis spectrophotometer (Thermo Scientific) to determine the wavelength where maximum absorption occurs ($\lambda_{max}$) and subsequently choose the appropriate photolysis cell for irradiation. The UVA cell consisted of four LEDs (two mounted on each side of the cuvette holder) and the UVB cell consisted of eight LEDs (four mounted on each side of the cuvette holder). A power source accompanied each cell that allowed the user to set a required voltage for irradiation, thus allowing a controllable photon source.

# Chapter 3

## Gas phase and thermal fragmentation of OMC

### 3.1 Introduction

OMC is a common UV filter used in in a variety of sunscreen products.[15] It is used as a UVB (280-320 nm) filter, although it's low energy absorption extends into the UVA, so that absorption also occurs between 320-400 nm. An increasing interest in its photodegradation pattern has been developed due to the hypothesis that organic filters could trigger bleaching of coral reefs,[66,67] in addition to the link to skin cancer in humans, as previously outlined. It is therefore important to understand the behaviour of OMC under exposure to UV radiation including its fragmentation pattern.

Two isomers of OMC, *trans* and *cis*, are important in its photochemical behaviour and are shown in Figure 3.1. For the *trans* isomer, the main photochemical reaction pathway in solution is isomerization to the *cis* form.[68] The *cis* form has a lower extinction coefficient than the *trans* form, so that the overall absorptivity of OMC decreases under UV irradiation.[68] A range of experimental techniques have been used to study OMC's excited state photodynamics,[15,69] and reactive oxygen sensitization.[18] Interestingly, the loss of absorbance exhibited by OMC after exposure to UV irradiation has been well-documented in literature.[68] The irreversible degradation of OMC has been reported, with absorbance loss reaching 90 %.[70] Other studies have found that a photostationary state is formed between the *trans* and *cis* isomers with only 30-50% loss of absorption.[68,71,72] The formation of dimer photoproducts after exposure to UV irradiation has also been reported.[68,73] Loss of absorbance has been observed to vary greatly under different experimental conditions.[68]
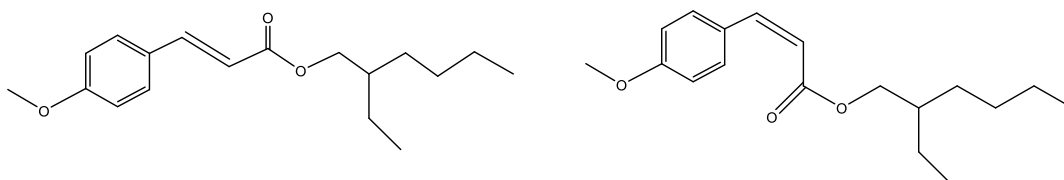


**Figure 3.1** Trans (left) and cis (right) isomers of OMC

Although real sunscreens are made up from a variety of different components,[11] it is important to study the individual component molecules to gain a better fundamental understanding of the intrinsic photochemistry and photodynamics. A recent extensive

study by Bardeen and co-workers on OMC found that aggregation of was important in determining the behaviour of OMC upon UV excitation.[68] They found the aggregation of OMC lead to a complex mixture of photoproducts, including production of UVA photoproducts, which generated singlet oxygen.[68] Given that aggregation effects have complicated Bardeen's study of OMC, it is useful to consider using gas-phase measurements to investigate the intrinsic photochemistry of individual sunscreen molecules. This approach has been applied successfully previously.[39] Studying molecules in the gas phase has the advantage of monitoring the photophysics of the isolated species, without taking into account any interactions with the surroundings (e.g. solvent).[39] In this Chapter, we present results to probe the intrinsic photochemistry and photodegradation pathways of OMC using the LIMS approach. OMC is studied as its protonated form, $[OMC+H]^+$, which is generated by electrospray ionization, to allow its study in the LIMS instrument. To complement the gas phase laser dissociation data, thermal fragmentation data are also presented to aid the interpretation of the excited state dynamics of $[OMC+H]^+$.

## 3.2 Experimental methods

OMC was purchased from Sigma Aldrich and was used without further purification. Solutions at a concentration of $10^{-3}$ M in ethanol (with traces of TFA to aid ionization efficiency) were used and were electrosprayed in positive ion mode using an amaZon SL dual funnel electrospray ionisation quadrupole ion trap (ESI-QIT) mass spectrometer (Bruker Daltonics, GmbH, Germany), modified to carry out LIMS, as described previously.[62] $[OMC+H]^+$ (*m/z* 291) was isolated in the ion trap before laser irradiation. A 10 Hz Nd:YAG (Surelite™, Amplitude Laser Group, San Jose, CA, USA) pumped OPO (Horizon™, Amplitude Laser Group) tuneable laser was used giving 0.15 mJ across the 400-214 (3.1-5.79 eV) nm range with a laser step size of 2 nm. The injection flow rate was 0.33 mL h$^{-1}$. The ion accumulation time was 10 ms for the photofragmentation experiments. A fragmentation time of 100 ms was selected to ensure that each ion packet would come into contact with only one laser pulse, to reduce the possibility of multiphoton events taking place.[39] This set of data was collected under the guidance and supervision of a senior group member, since a class 4 laser system was involved. The data was analysed using the equations outlined in Section 2.4.

Lower energy collisional induced dissociation (CID) data for $[OMC+H]^+$ were collected using the same amaZon mass spectrometer and the settings were as follows: capillary

voltage, 3800 V; dry temperature, 160°C; injection rate, 0.33 µL/h; nebulising gas pressure, 9.0 psi; dry gas, 5.0 l/min; accumulation time, 1 ms. CID energy was increased by an amplification of 0.02 in each segment and ion optics was used for optimisation in both cases.

HCD data for [OMC+H]$^+$ was collected using the Thermo Fisher Orbitrap Fusion$^{TM}$ mass spectrometer with the following settings: the syringe was operated at a flow rate of 3 µL/ min and with the following settings: MS$^2$ scan isolation mode, ion trap; detector type, ion trap; positive ion spray voltage (V), 3500; negative ion spray voltage (V), 2800; RF lens (%), 60; normalized AGC target (%), 100; maximum injection time (ms), 100; ion transfer tube temperature ( °C), 275; vaporizer temperature ( °C), 20. For the MS scan in this instrument the settings were as follows: detector type, Orbitrap; positive ion spray voltage (V), 3200; negative ion spray voltage (V), 2500; RF lens (%), 45; normalized AGC target (%), 100; maximum injection time (ms), 100.

## 3.3 Results and Discussion

### 3.3.1 Gas-phase UV absorption spectrum

Figure 3.2 shows the expected structure of protonated OMC, [OMC+H]$^+$, which should be produced following ESI in the positive ion mode. The alternative structure with protonation occurring at the anisole oxygen is not expected as the lone pair of that oxygen is considered to be delocalized around the aromatic ring.  ESI produced [OMC+H]$^+$ as an intense ion at *m/z* 291.
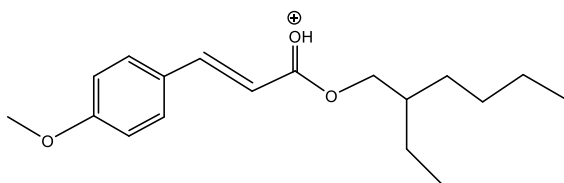


**Figure 3.2** Proposed structure of [OMC+H]$^+$
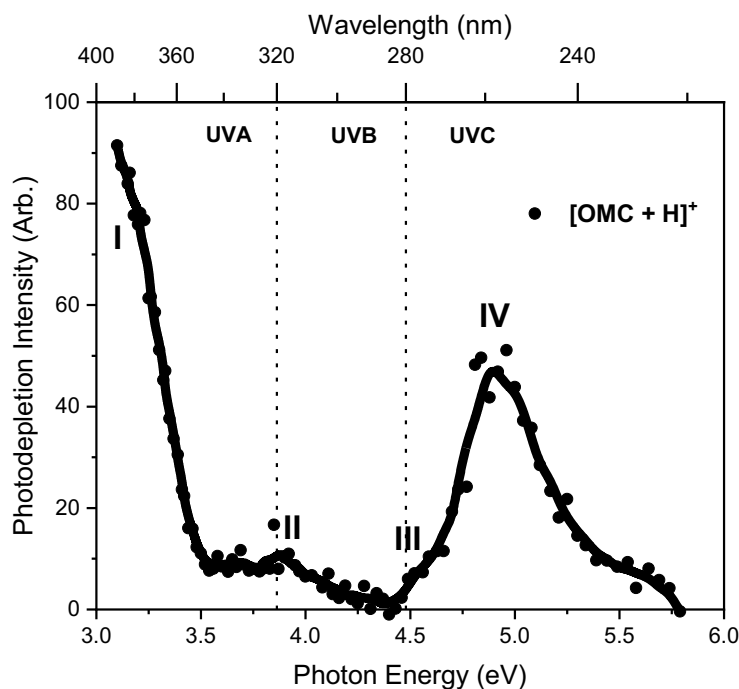
**Figure 3.3** Gas phase UV absorption (photodepletion) spectrum of [OMC+H]$^+$. The solid line is a five-point adjacent average of the data points.

Figure 3.3 shows the gas-phase absorption (photodepletion) spectrum of [OMC+H]$^+$ (*m/z* 291) obtained between 400-214 nm. The spectrum shown in Figure 3.3 shows that [OMC+H]$^+$ displays a strong absorption in the UVA spectral region (3.0-3.5 eV) and the UVC region (4.5-5.5 eV), which have been labelled I and IV, respectively, on Figure 3.3. Much lower absorption is observed in the UVB region with only a low intensity peak visible at around 3.9 eV. An additional small peak is visible at around 4.5 eV, around the onset of the strong absorption in the UVC region. OMC is primarily used as a UVB absorber in formulations,[15] and is known to have $\lambda_{max}$ = 310 nm in solution,[68] so it is interesting to observe that absorption in this region for the protonated species is reduced in the gas phase.

### 3.3.2 Photofragmentation pattern of [OMC+H]$^+$

Investigating the photofragmentation pattern of [OMC+H]$^+$ is important, as potential toxic photodegradant species produced upon exposure to UV radiation can be identified.[39] Figure 3.4 summarises the photofragment (PF) production intensity for the main photofragments of [OMC+H]$^+$ displayed along with the [OMC+H]$^+$ photodepletion spectrum for comparison. The intensity of the photofragments varies with photon energy; however, their absorption profiles show similar features and resemble that of the parent

ion. More specifically, all of the observed fragments show strong absorption in the UVA and UVC regions and relatively low absorption in the UVB region.
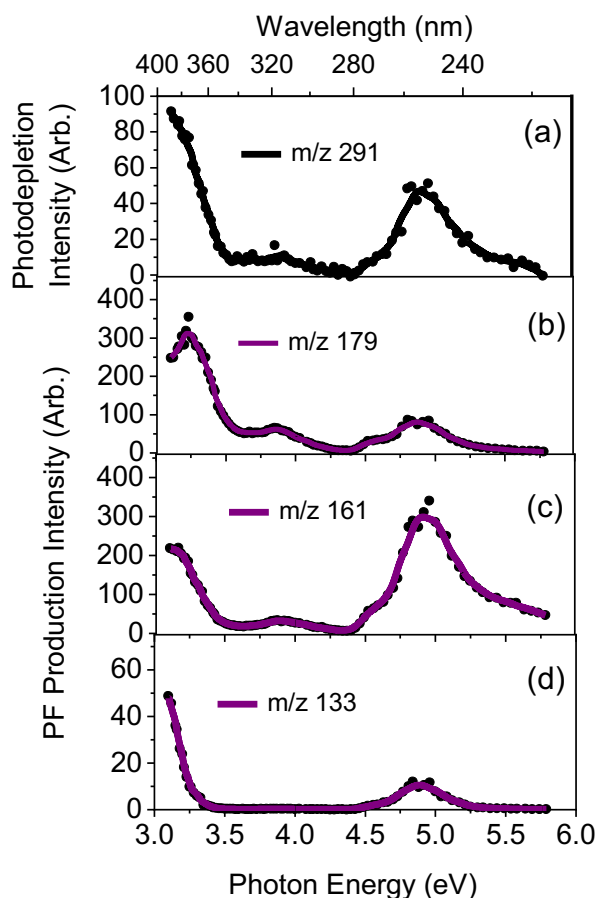


**Figure 3.4** (a) Gas phase UV absorption (photodepletion) spectrum of [OMC+H]$^+$. (b-d) Photofragment (PF) production intensity spectra of the three major photofragments with *m/z* 179, 161 and 133 respectively. The solid line is a five-point adjacent average of the data points.

The *m/z* 161 photofragment displays an absorption profile that matches the spectral profile of the [OMC+H]$^+$ parent ion most closely. The species at *m/z* 179 corresponds to protonated 4-methoxy cinnamic acid and the species at *m/z* 161 corresponds to cationic 4-methoxycinnamaldehyde, with the positive charge located on the aldehyde oxygen atom, following loss of $C_8H_{17}O$ from [OMC+H]$^+$. These fragments and proposed structures are in agreement with results from MacManus Spencer et al.[73] and Pattanaargson et al.[74] Proposed structures for the photofragments and the thermal fragments discussed below are presented in Table 3.1. Additional minor photofragments are listed in Appendix A1.1 (Figures A1.1-A1.3).

Figure 3.5 shows the relative ion yield of the major photofragments as a function of photon energy, to provide a more concise overview of photofragment production as a function of excitation energy.
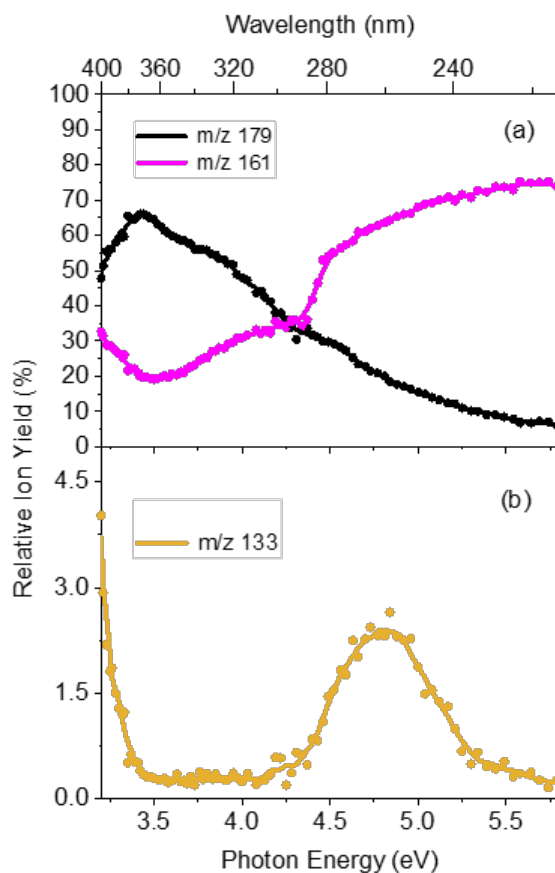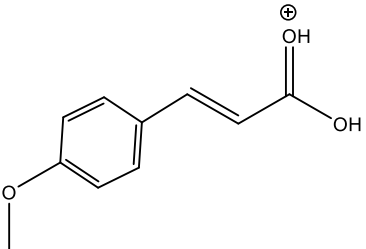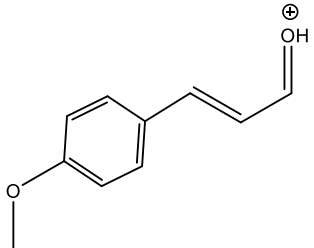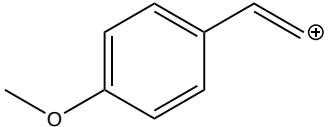


**Figure 3.5** Relative ion yield plot for the *m/z* 179, 161 and 133 photofragments of [OMC+H]⁺ between 3.2 and 5.8 eV. The solid line is a five-point adjacent average of the data points.

Overall, the relative ion yield of the photofragments at *m/z* 179 and 161 is greater compared to that of the photofragment with *m/z* 133, as can be seen for the reported ion intensities in Figure 3.4. The ion yield for the *m/z* 179 photofragment peaks in the UVA region (3.2-3.6 eV) and then decreasing smoothly across the UVB and UVC regions, whereas the yield for *m/z* 169 shows the opposite pattern, even though its initial yield is around 33 % at 3.2 eV. The initial yield for the *m/z* 179 photofragment is around 49 %. This could suggest that the *m/z* 161 photofragment could be formed from the one at *m/z* 179, possibly through the loss of $H_2O$. This can be further analysed though the thermal fragmentation data shown below. It is also evident that the photofragment with *m/z* 133 is mostly present in the UVA and UVC regions, but at much lower percentage. However, it is notable that its production profile is distinctive, suggesting that this photofragment is produced through a separate photochemical path.

**Table 3.1** Proposed structures for the fragments obtained via HCD and laser photoexcitation of [OMC+H]$^+$.

| Fragment Mass (m/z) | Proposed Structure of Fragment | m/z lost from [OMC+H]$^+$ (m/z 291) | Observed in HCD[a] (Y/N) | Observed in laser photoexcitation[a] (Y/N) |
|---|---|---|---|---|
| 179 |  | 112 | Y (s) | Y (vs) |
| 161 |  | 130 | Y (s) | Y (vs) |
| 133 |  | 158 | N | Y (vw) |
| 121 | - | 170 | Y (w) | Y (vw) |
| 113 | - | 178 | Y (vw) | N |
| 71 | - | 220 | Y (vw) | Y (vw) |

[a] very strong (vs), strong (s), medium (m), weak (w) and very weak (vw)

### 3.3.3 Thermal fragmentation versus photofragmentation of [OMC+H]$^+$

As outlined in Chapter 1, an efficient sunscreen filter needs to be able to return to the ground state from the excited state by releasing the excess energy gained through UV photon absorption as heat to the surroundings.[16]  In the solution phase, this can happen through vibrational relaxation.  In the gas phase; however, where there are no interactions with the solvent, this excess energy is held within the molecule, so it fragments when it relaxes back to the ground state. These fragments would be the same as those produced by the isolated molecule if it was heated, in the limit where the excited state decays on an ultrafast timescale without significant geometric (or electronic) evolution of the excited state. This is called statistical (or ergodic) fragmentation, as it corresponds to the "hot ground state" fragmentation pattern the molecule would follow.[39–41,43]  Therefore, fragments that are detected following UV excitation only are described as non-statistical (non-ergodic) and are produced from the excited state during photodissociation.[40] Lower (CID) and higher (HCD) energy collisional induced dissociation can be used to mimic the fragmentation profile of the "heated" molecule.[40,75]  More specifically, HCD can also be used to identify secondary fragments produced from primary fragments of the parent ion,[76] which is helpful when identifying thermal fragments from purely photochemical fragments.

Figures 3.6 and 3.7 display the thermal fragments of [OMC+H]$^+$ obtained through CID from 15 % CID energy onwards, as no fragmentation took place at lower CID energy. A relatively high CID energy percentage was required for [OMC+H]$^+$ to fragment. The CID thermal fragments observed are *m/z* 179 and *m/z* 161, with the *m/z* 179 fragment being the dominant fragment.  It is likely that *m/z* 179 is fragmenting into *m/z* 161 through loss of H$_2$O at higher (collisional) internal energies.
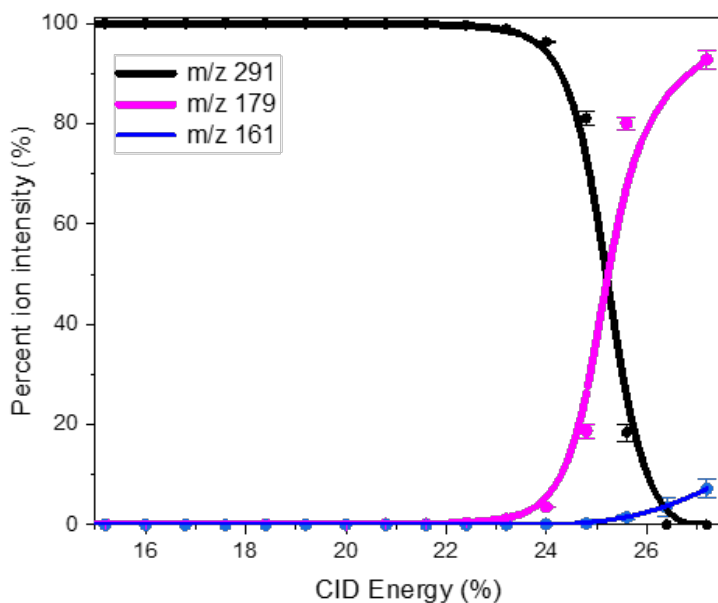
**Figure 3.6** Percent ion intensity of the major thermal fragments of [OMC+H]$^+$ at *m/z* 179 and 161 as a function of CID energy. The solid line is a three-point adjacent average of the data points and the error bars are the standard error of the mean.
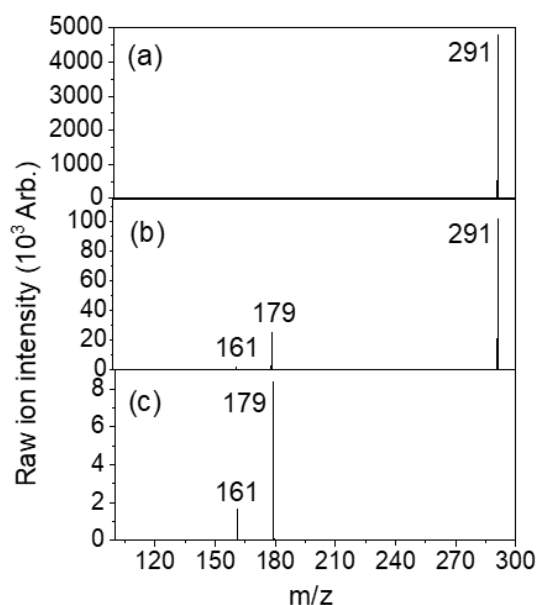


**Figure 3.7** Raw ion intensity mass spectra of the major thermal fragments of [OMC+H]$^+$ at (a) 0 %, (b) 25 % and (c) 27 % CID energy.

Figures 3.8 and 3.9 display the thermal fragments of [OMC+H]$^+$ obtained through HCD. In addition to the two main fragments observed in lower-energy CID (*m/z* 179 and *m/z* 161), minor fragments are also present at *m/z* 121, 113 and 71. [OMC+H]$^+$ fragments from very low collisional energies to form the species at *m/z* 179, as seen by the high

percent ion intensity of the species at 0 % HCD energy. Interestingly, the ion intensity of the *m/z* 179 fragment increases as the intensity of the parent ion decreases but then it decreases suggesting that it fragments as well, as seen by the shape of the curve. This coincides with an increase in the ion intensity of the *m/z* 161 fragment, indicating that it might be a secondary fragment produced from the *m/z* 179 fragment rather than directly from the parent ion. As noted above, *m/z* 179 is likely fragmenting into *m/z* 161 through loss of $H_2O$.
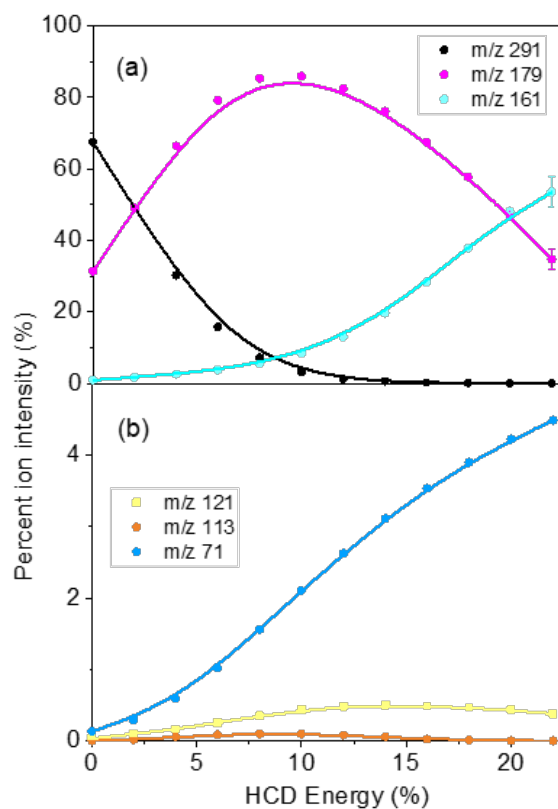


**Figure 3.8** Percent ion intensity of the (a) major and (b) minor thermal fragments of $[OMC+H]^+$ as a function of HCD energy. The solid line is a three-point adjacent average of the data points and the error bars are the standard error of the mean.
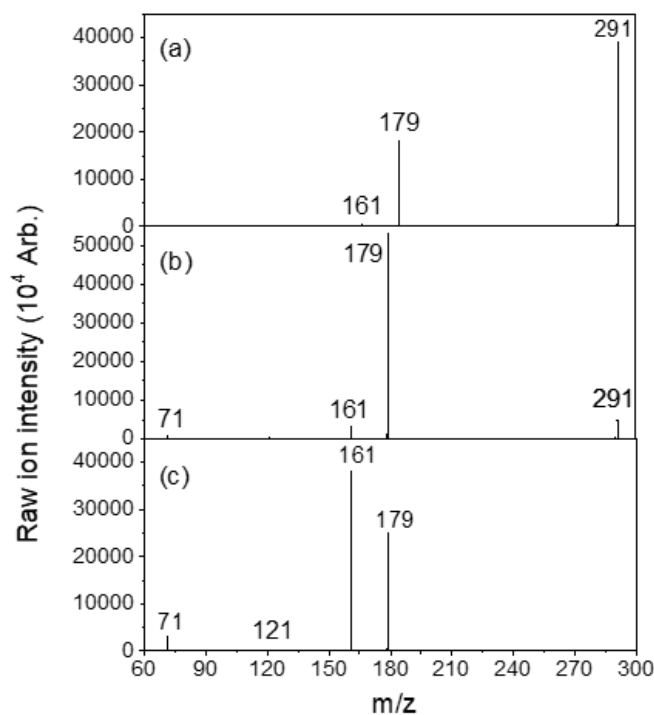
**Figure 3.9** Raw ion intensity mass spectra of the thermal fragments of [OMC+H]$^+$ at (a) 0 %, (b) 8 % and (c) 22 % HCD energy.

It is notable that the minor photofragment, *m/z* 133 (Figure 3.5b), is not observed as a thermal fragment, either via CID or HCD. This supports the assignment of this fragment as a photochemical fragment that is likely to appear through a longer-lived excited state, e.g. a triplet excited state.

However, the main photofragments are the same as the thermal fragments, so it can be inferred that photodissociation of [OMC+H]$^+$ is primarily statistical across the extended UVA-UVC region studied. This is in agreement with previous research on the molecule, as the main identified mechanism for OMC's relaxation to the ground state after UV excitation is ultrafast *cis-trans* isomerisation, while losing some of its UVB absorbing capacity.[15,77,78] More specifically, Tan and co-workers showed that once OMC is promoted to an excited state ($^1\pi\pi^*$), relaxation to the ground state occurs via an "optically dark" $^1n\pi^*$ state before moving on to the triplet state and then the ground state (S$_0$), so the process of releasing energy becomes slower, which influences the filter's efficiency. These experiments were performed on gas-phase neutral OMC by combining two-colour resonance-enhanced two-photon ionisation (RE2PI) and UV-UV depletion spectroscopy.[15] Ebata et al.[78] subsequently used laser-induced fluorescence (LIF) spectroscopy, UV−UV hole-burning (HB) spectroscopy as well as density functional theory (DFT) calculations to further investigate the non-radiative decay followed by

OMC. They also defined the photoisomerisation process followed by OMC as follows "$S_1$ (trans, $^1\pi\pi^*$) $\rightarrow$ $^1n\pi^*$ $\rightarrow$ $T_1$ ($^3\pi\pi^*$) $\rightarrow$ $S_0$ (cis)".[78]

## 3.4 Concluding Remarks

Laser interfaced mass spectrometry of $[OMC+H]^+$ has been used to obtain its gas-phase absorption spectrum via photodepletion spectroscopy, along with the accompanying photofragment production. The absorption spectrum is most intense in the UVA and UVC regions, which differs from the known absorption spectrum of neutral OMC in solution, which peaks in the UVB. Upon photoexcitation, $[OMC+H]^+$ fragments primarily into the *m/z* 179 and *m/z* 161 fragments, which are in line with the main known photofragments of OMC (4-methoxy cinnamic acid and cationic 4-methoxycinnamaldehyde). This illustrates the utility of LIMS photodissociation measurements as a straightforward route for identifying photoproducts.[79] CID and HCD measurements were performed to identify the thermal fragments of the ground electronic state of $[OMC+H]^+$. The *m/z* 179 and *m/z* 161 ions were found to be the major thermal fragments in line with the major photofragments.

The minor photofragment with *m/z* 133 was not observed as a thermal fragment, indicating that it is a purely photochemical fragment. The distinctive nature of this photofragment is evident in its unique production profile, shown in the ion-yield spectrum displayed in Figure 3.5b. Production of fragments with this type of profile have previously been associated with excitation of long-lived triplet excited states, *e.g.* as in deprotonated 2-phenylbenzimidazole-5-sulfonic acid where such photochemical photoproducts were associated with excitation of the $T_1$ state responsible for photosensitization.[40] Our observations indicate that such a state may be accessed between 410-240 nm, and also into the strong UVA region. This is in line with the known property of OMC to generate singlet oxygen under UVA irradiation, and again illustrates how LIMS can provide information on photochemical properties that are important in solution-phase behaviour.

# Chapter 4

# Photodegradation of OMC and OD-PABA in the solution phase

## 4.1 Introduction

Electrospray ionisation mass spectrometry (ESI-MS) has routinely been used to monitor photochemical reactions.[80,81] On-line photolysis studies[79,82,83] have also been carried out aiming to provide a direct method via which photoproducts generated in solution can be detected in the gas phase by the mass spectrometer. For sunscreens, in particular, experiments in the solution phase are critical, as it represents the sunscreen formulation more closely, compared to the laser gas-phase studies.[79]

The second UVB filter studied in this thesis is 2-ethylhexyl 4-(dimethylamino) benzoate (OD-PABA).
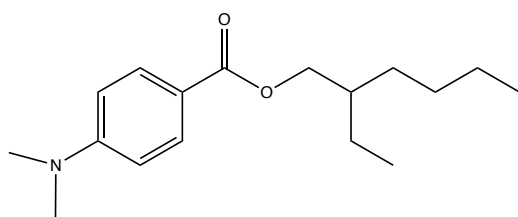


**Figure 4.1** Structure of OD-PABA

OD-PABA is a derivative of 4-aminobenzoic acid (PABA) and unlike PABA it is not soluble in water.[84] The extent to which OD-PABA and its photoproducts persist in the environment has been studied by various groups.[85–89] Sakkas et al.[85] investigated the effect of residual OD-PABA found in chlorinated water (e.g., swimming pools) on the production of toxic chlorinated compounds. Chlorine residue was measured in water samples collected from swimming pools and seawater and distilled water samples were also collected for comparison. The effect of dissolved organic matter (DOM) was also studied by varying the concentration of humic acids. HPLC/UV-DAD was used to monitor the photodegradation of OD-PABA, as a factor of a decrease in OD-PABA's concentration. The irradiation source was natural sunlight. GC-MS was also used to identify potential photoproducts. According to the results, the photodegradation of OD-PABA followed first order kinetics and the reaction rate was greater in distilled water and lowest in seawater samples. More specifically, in distilled water, 86% of OD-PABA was degraded following exposure to sunlight for 60 hours, followed by 83% in swimming

pool water and 80% in seawater. When a solar simulator was used 99% of OD-PABA degraded within 10 hours of irradiation in distilled water, followed by 96 and 92% in swimming pool and seawater respectively. The researchers also reported a negative relationship between the concentration of humic acids in the different solvents and the degradation of OD-PABA suggesting that DOM potentially acts as an inhibitor in the degradation process. The authors suggested that this could be explained by the competition for photons between the different species. In terms of the photoproducts observed, the most relevant for this piece of research were octyl-*p*-aminobenzoic acid with peaks at *m/z* 249, *m/z* 137 and *m/z* 120 and octyl-methyl-*p*-aminobenzoic acid with peaks at *m/z* 263, 151 and 134, as seen in the mass spectra for each photoproduct. OD-PABA also degraded into a photoproduct at *m/z* 166.[85]

This Chapter presents results to investigates the photodegradation of OMC and OD-PABA in solution. CID and HCD data for both compounds and the dimer of OMC, which was identified in solution, are also presented to provide a comparison between the thermal fragments (which can be seen produced during the electrospray process) and any photoproducts that are produced upon photolysis of the solutions.

## 4.2 Experimental methods

OMC and OD-PABA were purchased from Sigma Aldrich and were used without further purification. Stock solutions in ethanol were prepared at $4 \times 10^{-3}$ M and $1 \times 10^{-3}$ M for OMC and OD-PABA respectively. All data presented are an average of three runs.

The absorption spectra were recorded using a Genesis 180 UV-Vis spectrophotometer (Thermo Scientific) to determine the wavelength where maximum absorption occurs ($\lambda_{max}$) and subsequently choose the appropriate photolysis cell for irradiation. Cuvettes with a 1 cm pathlength and approximately 3 mL of solution were used. The absorption of OMC and OD-PABA, under UVB irradiation (310 nm), was monitored at a wavelength range of 200 to 400 nm, by irradiating a sample using a home-built photolysis cell containing eight LEDs (four on each side) operating at a maximum voltage of 20.5 V. The voltage used for the irradiation was approximately 19.2 V. A fitted lid was used to cover the cuvette and hence minimise loss of solvent from the cuvette over the photolysis time. The cuvette containing the sample to be irradiated was placed in the cuvette holder in between the LEDs. In these experiments, solutions of $4 \times 10^{-5}$ M and $1 \times 10^{-5}$ M were used for OMC and OD-PABA respectively.

Mass spectrometry analysis of the solution phase photolysis experiments was carried out using an HCT ultra ETD II mass spectrometer (Bruker Daltonics, Germany). For OMC, a $4 \times 10^{-3}$ M solution was electrosprayed, as it was found that a better ion signal was achieved with this concentration. Traces of TFA (*ca.*10 μL) was added to aid ionization efficiency. The same UVB photolysis cell described above was used. A background spectrum obtained with just the rinsing solution (ethanol or 1:1 ethanol:isopropanol) on, injected via a syringe-pump set, was recorded first on the mass spectrometer. A 500 μL syringe (Hamilton) was used to obtain approximately 200 μL of the unirradiated sample and a full MS scan in a 70-700 m/z range was recorded, with the solution. The syringe solution was replaced with the rinsing solution. The LEDs were then turned on and the solution was irradiated for 5 s. The LEDs were switched off again. An additional 200 μL aliquot was collected from the cuvette, injected into the mass spectrometer and the mass spectrum was recorded again. The syringe was covered with foil to prevent light exposure. This process was repeated at 20, 40, 60 and 120 s. The rinsing time between each experimental run would vary but one hour was mostly used to ensure that the baseline would be as clear as possible for the next run to be able to measure the potential difference in ion intensity of the parent ion and any photoproducts produced. The same procedure was followed for OD-PABA ($1 \times 10^{-5}$ M) but every 1 hour for 7 hours.

CID data on the dimer of OMC ($4 \times 10^{-3}$ M , *m/z* 581) identified following electrospray of solution were collected using the amaZon SL Dual Funnel Ion Trap Mass Spectrometer with the following settings: capillary voltage, 3750 V; dry temperature, 110°C; injection rate, 0.33 μL/h; nebulising gas pressure, 10.0 psi; dry gas, 8.0 l/min; accumulation time, 3 ms. CID energy was increasing by an amplification of 0.02 in each segment and ion optics was used for optimisation.

CID data on OD-PABA ($1 \times 10^{-5}$ M) were collected using an HCT ultra ETD II mass spectrometer (Bruker Daltonics, Germany) with the following settings: capillary voltage, 3880 V; dry temperature, 200°C; injection rate, 80 μL/h; nebulising gas pressure, 10.0 psi; dry gas, 5.0 l/min; accumulation time, 12 ms.

HCD data was collected on a Thermo Fisher Orbitrap Fusion™ mass spectrometer with the following settings: MS2 scan isolation mode, ion trap; detector type, ion trap; positive ion spray voltage (V), 3500; negative ion spray voltage (V), 2800; RF lens (%), 60; normalized AGC target (%), 100; maximum injection time (ms), 100; ion transfer tube

temperature ( °C), 275; vaporizer temperature ( °C), 20. For the MS scan in this instrument the settings were as follows: detector type, Orbitrap; positive ion spray voltage (V), 3200; negative ion spray voltage (V), 2500; RF lens (%), 45; normalized AGC target (%), 100; maximum injection time (ms), 100. The injection flow rate was 3μL/ min.

## 4.3 Results and Discussion

### 4.3.1 Octyl methoxycinnamate

#### 4.3.1.1 Solution phase absorption spectroscopy

A solution of OMC was irradiated at 310 nm using the LED photolysis cell. Figure 4.2 displays the solution phase absorption spectrum of OMC obtained following irradiation for up to 120 s. OMC's absorption decreases significantly within a very short time framework. The first noticeable decrease in absorption occurs after 5 seconds, where the known *trans* to *cis* isomerisation likely takes place.[68] The absorbance continues to decrease until approximately 80 seconds of irradiation has been reached, where no further decrease is observed. However, based on this spectrum alone, it is not possible to deduce whether isomerisation, photoproduct formation or both are taking place during photoexcitation of OMC.
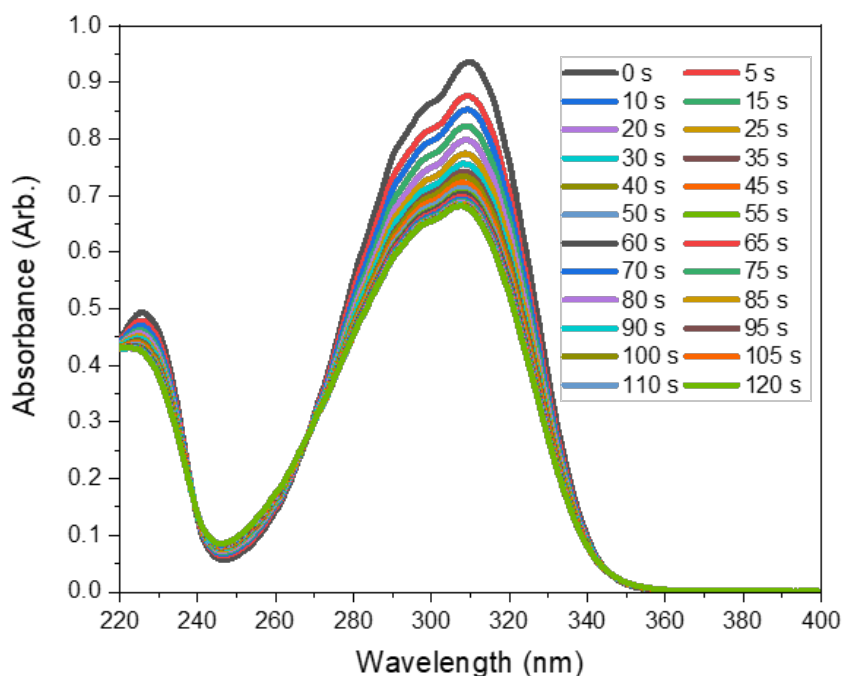


**Figure 4.2** Absorption spectrum of OMC in ethanol under irradiation at 310 nm for 120 s.

To rule out hydrolysis in ethanol during the irradiation time, a test experiment was carried out (Appendix A1.2, Figure A1.4) which showed that OMC does not hydrolyse during this time framework (i.e. there was no change to the UV-VIS spectrum over this timescale with no photolysis). If hydrolysis had taken place, the $\lambda_{max}$ would have been expected to shift towards lower wavelengths (~ 274 nm) to correspond to the $\lambda_{max}$ for 4-methoxycinnamic acid, one of the two building blocks of OMC.[90] In addition, OMC has been found to be thermally stable up until 200 °C[91] after which it degrades, so thermal degradation as a result of exposure to the LEDs in the photolysis cell will not take place, as the temperature of both the cell and the solution was measured and it was around 23 °C, measured at a constant room temperature of 22 °C.

The absorption spectrum shown in Figure 4.2 is in agreement with findings from Hanson et al.[68] who have also studied the isomerisation behaviour of OMC in solution, in both methanol and cyclohexane, under UV radiation. The absorption spectra recorded before exposure to UV radiation indicated that the maximum absorption for trans-OMC in ethanol occurred at 310 nm ($\lambda_{max}$ = 310 nm) and at $\lambda_{max}$ = 291 nm in cyclohexane. This also verifies that the data presented in Figure 4.1 correspond primarily to a solution of the trans-isomer of OMC. In contrast, for cis-OMC maximum absorption occurred at $\lambda_{max}$=305 nm in both solvents. The decrease in absorbance was faster in methanol compared to cyclohexane suggesting that the non-polar solvent favoured the stability of *trans*-OMC in solution. Quantum yields were calculated in methanol and cyclohexane, in an attempt to carry out a quantitative analysis of the *cis-trans* conversion in the excited state of OMC, as $\varphi_{CT}$ and $\varphi_{TC}$ respectively. $\varphi_{TC}$ in methanol (0.37) was found to be greater compared to cyclohexane (0.28), whereas the results for $\varphi_{CT}$ indicated the opposite behaviour, following a similar pattern as in the solution experiment.[68]

### 4.3.1.2 Solution-phase photolysis

A solution of OMC was irradiated at 310 nm using a photolysis cell to investigate whether photoproducts could be detected in from solution photolysis, and if so, to compare them with the gas phase data (Chapter 3). An HCT ultra ETD II mass spectrometer (Bruker Daltonics, Germany) was used to perform electrospray analysis of the photolyzed solutions, following the method described in detail in Section 4.2. OMC was electrospayed in positive ion mode to detect [OMC+H]$^+$ (*m/z* 291). Measurements were taken at 0, 5, 20, 40, 60 and 120 seconds and the results are presented in Figure 4.3.
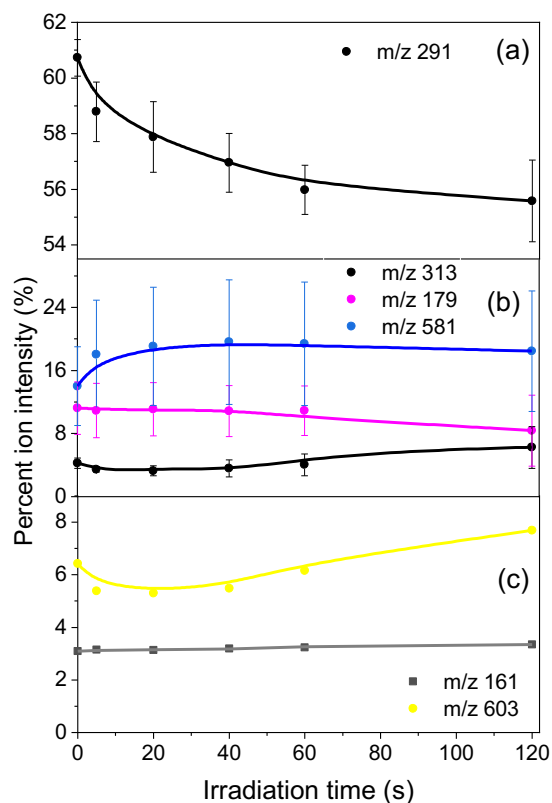
**Figure 4.3** Plot of the solution-phase photodegradation of [OMC+H]$^+$ (in ethanol) obtained through monitoring changes in (a) the parent ion intensity and (b,c) changes in the ion intensity of the photoproducts formed under UVB irradiation for 120 s. The solid line is a three-point adjacent average of the data and the error bars are the standard error of the mean.

Figure 4.2 shows the absorbance of OMC decreasing over irradiation time which is in agreement with the data shown in Figure 4.3a, as the ion intensity of [OMC+H]$^+$ decreases over irradiation time. The rate of decrease seems to be higher between 0 and 5 seconds, which could be further evidence of the isomerisation taking place, with a resulting decrease in the absorbance of the *trans* isomer. This decrease is followed by a slight increase in the ion intensity of some photoproducts, namely the species at *m/z* 179, 161, 303, 581 and 603. Interestingly, all photoproducts seem to be present in solution at 0 seconds which might suggest that they are produced by in source dissociation, as a result of the source conditions, during ESI.[54,92,93] To investigate the extent to which this occurs, further studies need to be conducted by varying the voltage and temperature at the source[94] and seeing which fragments are detected. Another possible explanation could be that they are formed while the solution is being prepared, during sonication. After sonication, the flask becomes slightly heated which might lead to the production of thermal fragments that remain in solution and are then detected by the mass spectrometer. The LC-MS method commonly used to detect sunscreen photoproducts in solution,

combined with mass spectrometry, is able to distinctly separate the starting analyte from the photoproducts that are eluted after irradiation so it likely is a more appropriate method to follow to investigate photoproduct production.[19,32,34,95] The species at *m/z* 179 and 161 have been identified in Chapter 1, are the known main thermal fragments and photoproducts of [OMC+H]$^+$.[68,74]

The species at *m/z* 581 was identified as the cyclodimer of OMC, formed by the dimerization of the *E*- and *Z*- isomers of OMC. Multiple reports[34,73,96] have discussed the formation of the dimer following OMC's exposure to light. Two kinds of the dimer seem to form, primarily through the alkene bond, truxinates (head-to-head isomers) and truxillates (head-to-tail isomers). It has been shown[34] that truxinate dimers are formed preferentially due to better highest-occupied molecular orbital (HOMO) lowest-unoccupied molecular orbital (LUMO) overlap as well as steric interactions. The structures of the cyclodimers are presented in Figure 4.4. Finally, the fragments at *m/z* 313 and 603 can be attributed to the sodiated[34] forms of OMC (i.e. OMC.Na$^+$) and the dimer respectively. These results could suggest that dimerisation, in addition to *cis-trans* isomerisation, is a pathway followed during OMC exposure to UVB irradiation.
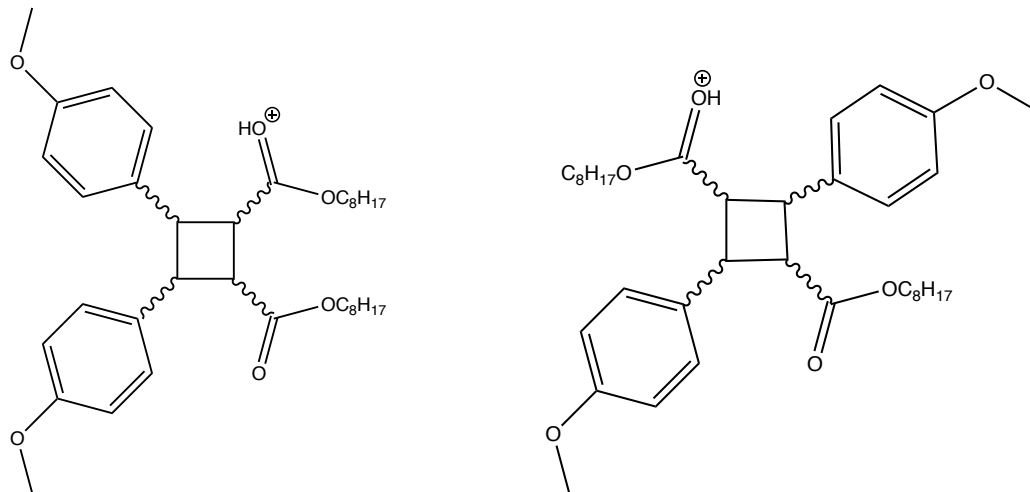


**Figure 4.4** Proposed structures[96] of the protonated truxinate (left) and truxillate (right) OMC dimers (m/z 581) formed after OMC's exposure to UV irradiation, assuming protonation during electrospray takes place at the carbonyl.

**4.3.1.3 Thermal fragmentation of the OMC cyclodimer produced upon UVB irradiation**

Since the OMC cyclodimer was present in solution upon irradiation, its thermal fragmentation pattern was also investigated, using an HCT ultra ETD II mass spectrometer (Bruker Daltonics, Germany). Figures 4.5 and 4.6 show the thermal fragments produced from the dimer, detected in its protonated form (m/z 581) over an increasing CID energy percentage. Figure 4.5 shows the ion intensity changes as a function of CID, while Figure 4.6 shows the associated mass spectra recorded at selected collisional energies.
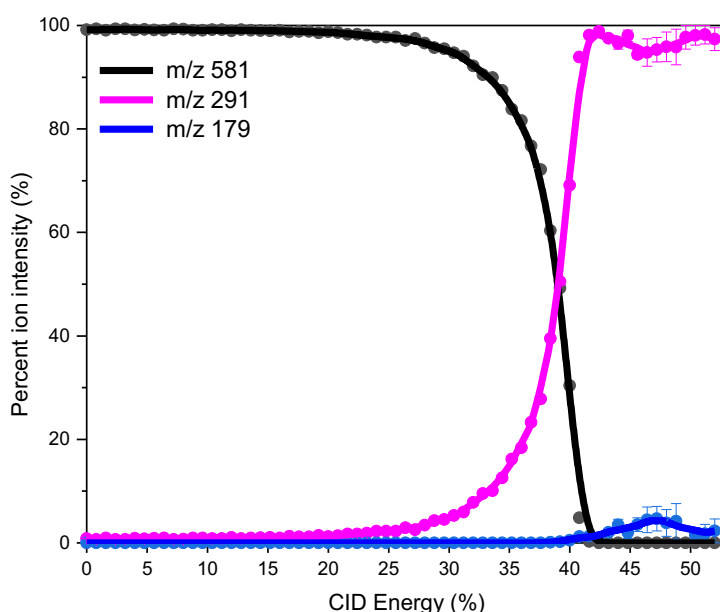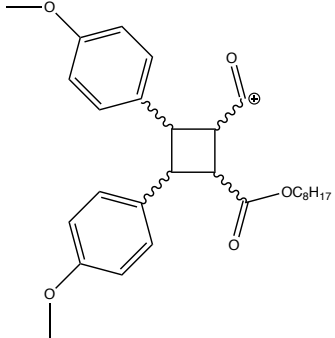


**Figure 4.5** Percent ion intensity of the main thermal fragment of the protonated cyclodimer of OMC [2OMC+H]$^+$ (*m/z* 581) at *m/z* 291 and *m/z* 179. The solid line is a three-point adjacent average of the data and the error bars are the standard error of the mean.
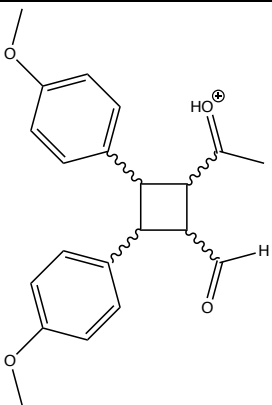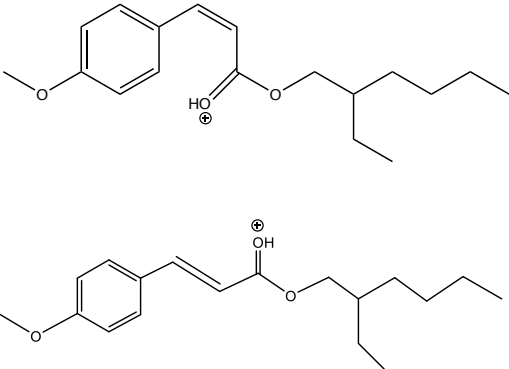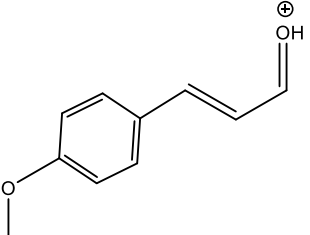
Based on the CID data, the main thermal fragments are protonated OMC (*m/z* 291) and the fragment at *m/z* 179, which has been observed as a fragment in the studies of the OMC monomer. As seen in Figure 4.6d, the species at *m/z* 161 discussed previously is also produced as a minor fragment at a higher CID energy percentage. Figures 4.7 and 4.8 show the thermal fragments produced over an increasing HCD energy percentage. The percent ion intensity of the dimer, around 55 %, is much less than 100 % at 0 % HCD energy, as seen in Figure 4.7a. The high percent ion intensity of [OMC+H]$^+$ (38%) at 0% HCD energy highlights the dimerisation process that is taking place, as the two species are possibly dimerising and falling apart at very low internal energy. The dimer's

instability could also explain the relatively higher error bar values, compared to other data sets presented, as it was more challenging to isolate the dimer in the ion trap compared to $[OMC+H]^+$.

Nevertheless, the ion intensity of $[OMC+H]^+$ increases as the intensity of the dimer decreases and then decreases again as it is fragmenting. Therefore, the major (*m/z* 179, 161) and minor (*m/z* 451, 339, 321, 241, 148) fragments observed could have been produced by fragmentation of both $[OMC+H]^+$ and the dimer. These fragments are in agreement with ones reported elsewhere[34,73,96] and proposed structures are shown in Table 4.1. However, this is the first time the production profile of these fragments has been measured using HCD, and this measurement would be important to interpret future gas-phase photodissociation measurements of the protonated dimer.

**Table 4.1** Proposed structures for the thermal fragments obtained via HCD and the photoproducts produced by the cyclodimer of OMC, which was formed in the solution phase following UVB photolysis.

| Fragment Mass (*m/z*) | Proposed Structure of Fragment | m/z lost from dimer (*m/z* 581) | Observed in HCD[a] (Y/N) | Observed in solution phase photolysis[a] under UVB light |
|---|---|---|---|---|
| 451 |  | 130 | Y (m) | N |

| | | | | |
|---|---|---|---|---|
| 339 |  | 242 | Y (vw) | N |
| 321 | loss of H₂O from *m/z* 339 | 260 | Y (w) | N |
| 291 |  | 290 | Y (vs) | Y (s) |
| 241 |  | 340 | Y (vw) | N |
| 179 |  | 402 | Y (s) | Y (w) |
| 161 |  | 420 | Y (w) | Y (vw) |

[a] very strong (vs), strong (s), medium (m), weak (w) and very weak (vw)
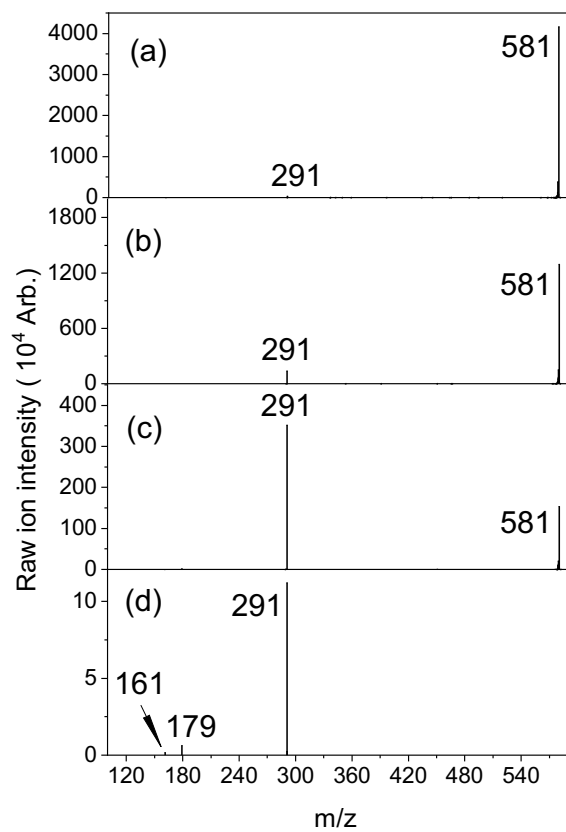
**Figure 4.6** Ion intensity mass spectra (positive ion mode) of the major thermal fragments of the cyclodimer of OMC [2OMC+H]$^+$ at (a) 0 %, (b) 33 %, (c) 40 % and (d) 52 % CID energy.
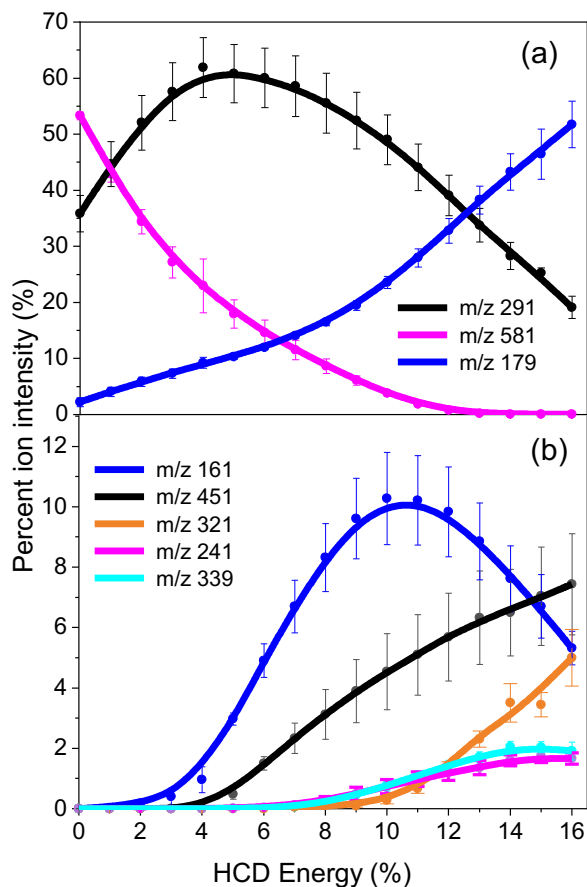
**Figure 4.7** Percent ion intensity of the (a) major and (b) minor thermal fragments of the cyclodimer of OMC [2OMC+H]$^+$ (*m/z* 581) at *m/z* 291 and *m/z* 179. The solid line is a three-point adjacent average of the data and the error bars are the standard error of the mean.

**Figure 4.8** Raw ion intensity mass spectra of the thermal fragments produced by the cyclodimer of OMC [2OMC+H]$^+$ at (a) 0 %, (b) 5 %, (c) 10 % and (d) 16 % HCD energy.

### 4.3.2 2-ethylhexyl 4-(dimethylamino) benzoate (OD-PABA)

### 4.3.2.1 Solution phase absorption

A solution of neutral OD-PABA was irradiated at 310 nm for 7 hours using the UVB photolysis cell. Figure 4.9 shows the absorption spectra obtained over this time. The absorbance of OD-PABA decreases slightly every hour as the irradiation period increases. A similar experiment was carried out in a recent published study[19] and the researchers saw a significant decrease in the absorbance of OD-PABA after 10 hours of irradiation. More specifically, OD-PABA was not detected in the TD-ESI/MS spectrum obtained in that work after 48 hours of irradiation.[19] Based on the data presented in Figure 4.9, OD-PABA seems to be more photostable than OMC. A stability experiment in ethanol was also carried out over 7 hours to investigate whether hydrolysis might be taking place alongside photodegradation and is shown in Appendix A1.3, Figure A1.5. shows a slight increase in OD-PABA's absorbance over the irradiation time but whether

this is due to instrument calibration or hydrolysis is not clear. It can be concluded however, that photodegradation and hydrolysis are not in competition for OD-PABA.
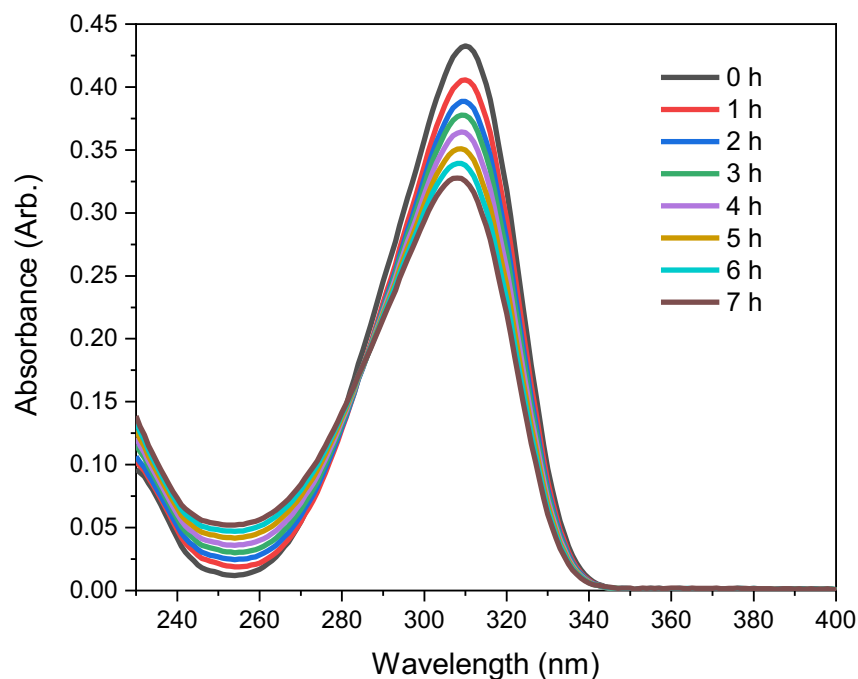


**Figure 4.9** Absorption spectrum of OD-PABA in ethanol under irradiation at 310 nm for 7 hours.

### 4.3.2.2 Solution phase photolysis

The effect of UVB irradiation on the degradation of [OD-PABA+H]$^+$ (m/z 278, Figure 4.10) in solution was investigated using the same UVB photolysis cell and the HCT mass spectrometer. Nguyen at al.[35] carried out a calculation to identify whether the carbonyl oxygen or the nitrogen of the amino group was the most likely protonation site in the molecule, with the nitrogen being favourable. The same procedure was followed as with [OMC+H]$^+$.
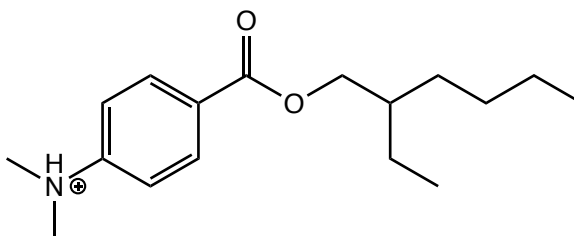


**Figure 4.10** Proposed structure of [OD-PABA+H]$^+$

As seen in the data presented in Figure 4.11, OD-PABA's percent ion intensity decreases slightly as the irradiation time increases, in accordance with the changes seen in the absorption spectrum (Figure 4.9). This decrease is accompanied by an increase in the ion intensity of a major photoproduct at m/z 264, which has also been identified in the literature as a transformation product upon irradiation,[88] as a result of loss of a methyl group. Minor photoproducts are also present at m/z 152, 166 and 151. The last two have also been identified as potential photoproducts in LC-MS[35,86] and TD-ESI/MS[19] experiments.
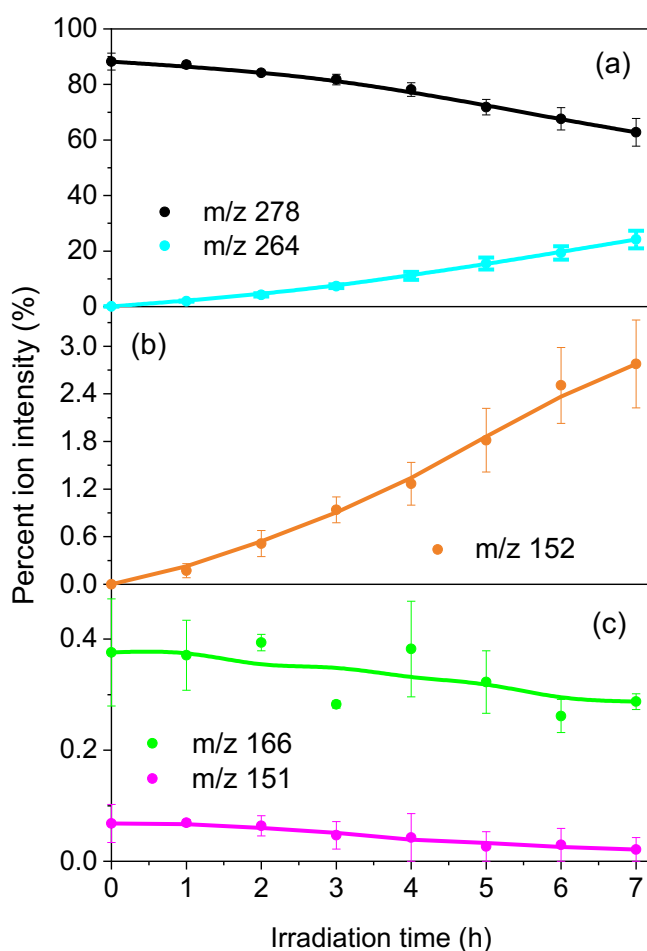


**Figure 4.11** Plot of the solution-phase photodegradation of [OD-PABA+H]$^+$ obtained by monitoring changes in (a) the parent ion intensity and major photoproduct at m/z 264 and (b,c) the minor photoproducts formed under UVB irradiation for 7 hours. The solid line is a three-point adjacent average of the data and the error bars are the standard error of the mean.

### 4.3.2.3 Thermal fragmentation of OD-PABA
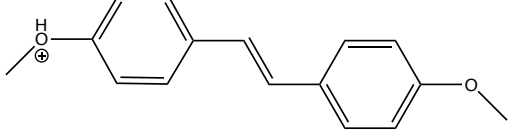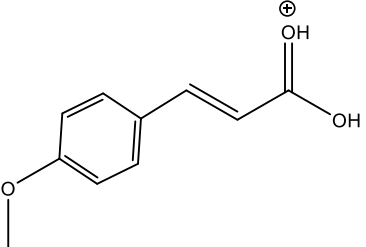
As with OMC, the thermal fragments for OD-PABA were also explored (studied as its protonated form). The results are summarised in Figures 4.12-4.15.
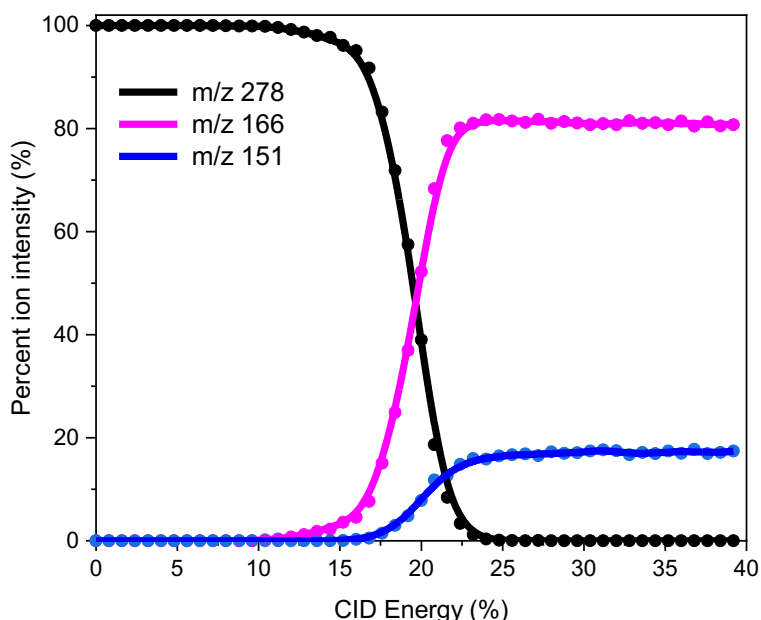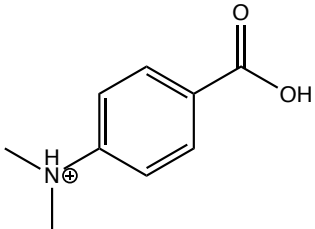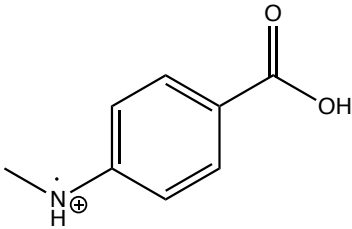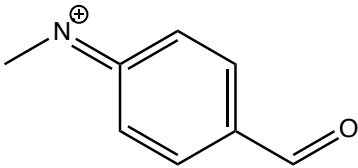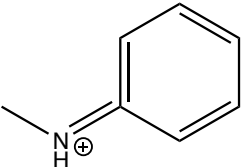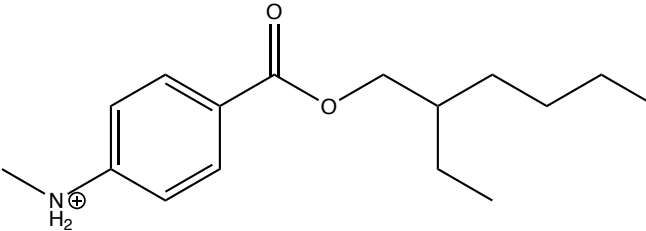


**Figure 4.12** Percent ion intensity of the main thermal fragments of [OD-PABA+H]$^+$ (*m/z* 278) at *m/z* 166 and *m/z* 151 produced over an increasing CID energy percentage. The solid line is a three-point adjacent average of the data and the error bars are the standard error of the mean.

Figures 4.12 and 4.13 show the thermal fragments produced over an increasing CID energy percentage. The main thermal fragments were the ones at *m/z* 166 and 151, which were also identified as photoproducts. Proposed structures of all fragments can be seen in Table 4.2. Two additional minor fragments are shown Figure 4.13, namely the ones at *m/z* 122 and 107, visible at 30 % CID energy. The thermal fragments produced during an increasing HCD energy percentage are displayed in Figures 4.14 and 4.15. Figure 4.12 shows the *m/z* 166 fragment fragmenting as well at around 35 % HCD energy. Even though the *m/z* 151 fragment is mainly produced by the parent ion, it can also be a secondary fragment, produced by the *m/z* 166 fragment. The *m/z* 122 fragment is likely produced from the *m/z* 166 fragment as well. The *m/z* 134 could be a secondary fragment of the *m/z* 151 fragment. An additional minor fragment is the one at *m/z* 107. These have been reported previously as well.[88]

**Table 4.2** Proposed structures for the thermal fragments obtained via HCD and the photoproducts produced by [OD-PABA+H]$^+$ following solution-phase photolysis under exposure to UVB irradiation.

| Fragment Mass (m/z) | Proposed Structure of Fragment | m/z lost from [OD-PABA+H]$^+$ (*m/z* 278) | Observed in HCD[a] (Y/N) | Observed in solution phase photolysis[a] under UVB light |
|---|---|---|---|---|
| 166 |  | 112 | Y (vs) | Y (vw) |
| 151 |  | 227 | Y (vs) | Y (vw) |
| 134 |  | 144 | Y (w) | N |
| 107 |  | 171 | Y (vw) | N |
| 264 |  | 14 | N | Y (s) |

[a] very strong (vs), strong (s), medium (m), weak (w) and very weak (vw)
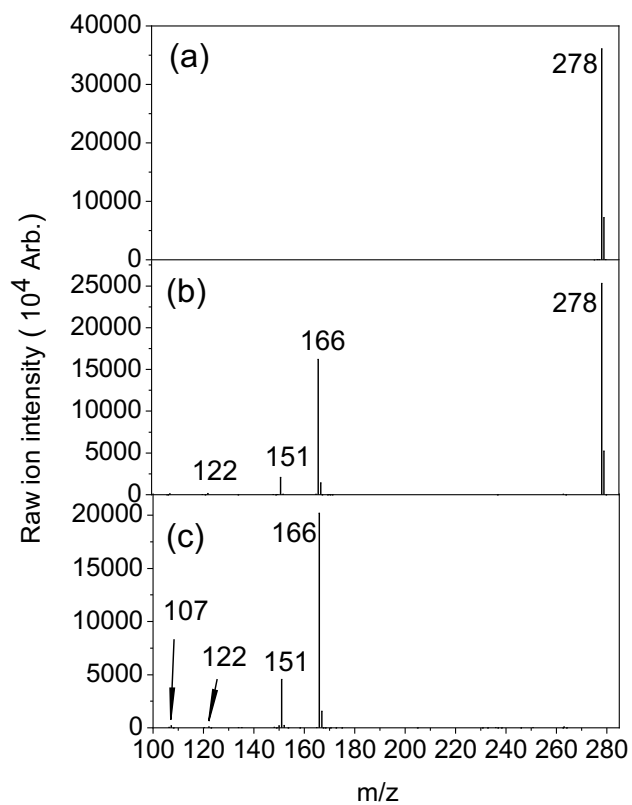
**Figure 4.13** Ion intensity mass spectra of the thermal fragments produced by [OD-PABA+H]$^+$ at (a) 0 %, (b) 19 % and (c) 30 % CID energy.
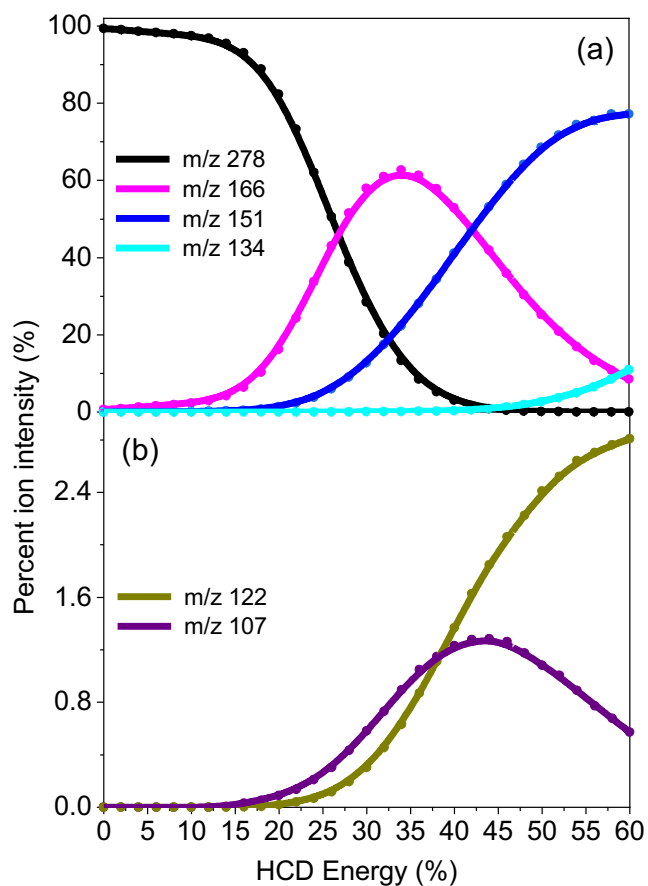
**Figure 4.14** Percent ion intensity of the (a) major and (b) minor thermal fragments of [OD-PABA+H]$^+$ at *m/z* 166, 151, 134 and *m/z* 122, 107 respectively, produced over an increasing HCD energy percentage. The solid line is a three-point adjacent average of the data and the error bars are the standard error of the mean.
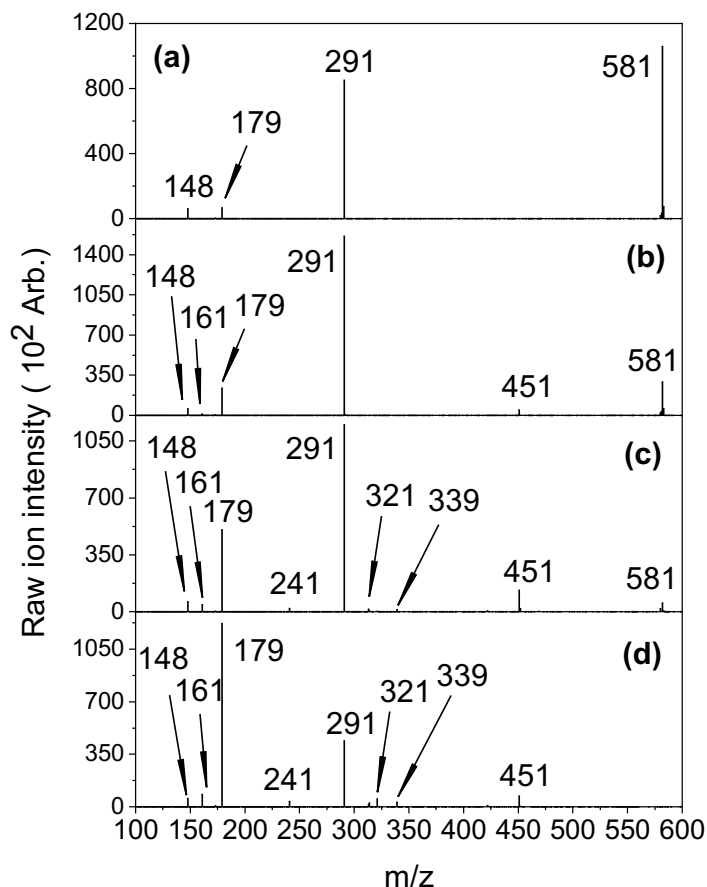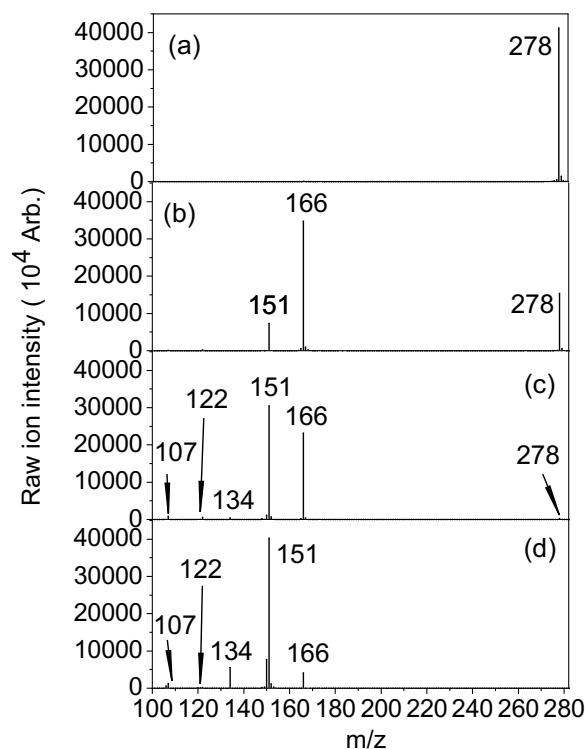
**Figure 4.15** Ion intensity mass spectra of the thermal fragments produced by OD-PABA+H]$^+$ at 0 % (a), 30 % (b), 44 % (c) and 60 % (d) HCD energy.

Since the *m/z* 264 fragment is not observed as a thermal fragment, it can be inferred that it is a photoproduct produced exclusively after exposure to UVB irradiation. This likely occurs through a long-lived excited state, similar to that outlined for OMC in Chapter 3. More specifically, as the *m/z* 264 fragment is produced via loss of a methyl radical, OD-PABA's efficiency as a sunscreen filter is compromised.[39,97] In addition, a recent environmental study[89] explored the toxicity of some of OD-PABA's photoproducts. Various parameters such as water solubility, bioconcentration factor (BCF), overall persistence in the environment (POV), long-range transport potential (LRTP) and the octanol-water partition coefficient (log $K_{OW}$) were measured to study the degradation of OD-PABA in the environment. OD-PABA had a solubility value of 0.6963 mg/L and most photoproducts had low values of a similar magnitude. Despite its low value, the researchers pointed out that OD-PABA had still been detected in rivers and lakes. Mainly mono and di-chloro derivatives of OD-PABA, as well as some oxidation products were associated with higher values for all the parameters outlined above and were deemed toxic. The researchers concluded that mixtures of photoproducts identified in the environment could be more toxic than OD-PABA itself.

## 4.4 Concluding remarks

This chapter presents new measurements on the photodegradation of OMC and OD-PABA in solution, which have been conducted here for the first time using photolysis of small volumes of sunscreen solutions, which are exposed to irradiation in home-built UV diode photolysis cells. The experiments performed in this chapter provide a benchmark against previous results obtained on much larger volume solutions which were photolyzed by much higher power mercury lamp photon sources.[34] They are therefore a much more sustainable method for performing such experiments, since they have lower solvent and energy requirements. Another aim of this chapter was to evaluate whether direct injection of the irradiated solution via a syringe into the mass spectrometer is an appropriate method to probe photodegradation (i.e. production of photoproducts).

Both the OMC and OD-PABA molecules studied were electrosprayed in positive ion mode and the intensity of both parent ions decreased following exposure to UVB irradiation. The decrease in the ion intensity of the parent ion was accompanied by an increase in the ion intensity of some photoproducts. For OMC, the main photoproducts at *m/z* 179 and 161 matched the thermal fragments obtained via CID and HCD and the photoproducts obtained via LIMS. The fact that the products were identical is not surprising as they reflect low energy molecular dissociation pathways for the system. However, an additional photoproduct was identified from the solution photolysis, namely the cyclodimer of OMC (*m/z* 581) (detected in its protonated form), which is a purely photochemical product. Thermal fragmentation data were also presented for this species.

For OD-PABA, the main photoproduct identified in solution was the fragment at *m/z* 264, which was formed through ejection of a methyl radical, which is not desirable for a sunscreen filter. The remaining photoproducts were also thermal fragments, observed in CID and HCD experiments.

The results obtained in our home built, low volume photolysis cells, gave results that identified the same photoproducts as had been observed previously in bulk solution photolysis measurements. This demonstrated that the new methodology we employed could be confidently used for the analysis of previously untested sunscreen molecules. Furthermore, the results obtained for OMC were important in the context of the gas-phase photolysis results presented in Chapter 3. Our studies of OMC both in the gas-phase via LIMS, and in solution using our UV diode set ups, identified the same main photoproducts. This illustrates that gas-phase LIMS is a useful tool for identifying

photodegradation products. In future work, photofragmentation of OD-PABA in the gas phase via LIMS would be useful to determine whether additional photoproducts that were not produced during solution photolysis with a lower power photon source, as well as investigating whether statistical or non-statistical fragmentation is taking place in the UVA-UVC region, and hence providing enhanced fundamental information on the photophysics and hence photostability of OD-PABA.

Lastly, an important point which has not been acknowledged in any of the previous solution-phase photolysis studies of sunscreen molecules is noted.[19] The work performed in this chapter has included careful CID and HCD studies which have characterised the pathways by which the parent ions can potentially break down during the electrospray/mass spectrometry process. We have found that protonated OMC and OD-PABA predominantly break apart upon CID and HCD to form the same molecular fragments that have been previously identified as photoproducts from solution-phase photolysis measurements. It is therefore not clear whether the photoproducts previously detected by the mass spectrometer were actually produced during UVB irradiation or from processes such as in-source dissociation. More experiments investigating the effect of changing the source conditions on the photodissociation of sunscreen UV filters need to take place, and there should be acknowledgement of this potential problem in future solution-photolysis studies.

# Chapter 5

## Natural UV filters: a study on vanillin and its synergistic effect with chemical UV filters

### 5.1 Introduction

As outlined in Section 1.4, natural alternatives for UV filters, lignin in particular, have received increased attention in recent years as substitutes of chemical UV filters.[46,47] Vanillin is one of the possible building blocks of the lignin polymer, alongside syringol and guaiacol (Figure 5.1).[98] Research on these subunits has already been carried out, aiming to provide an insight into their spectroscopic characteristics[99] and behaviour under UV irradiation.[100] A recent study investigated the photochemistry of vanillin using laser flash photolysis.[101] In this study, the wavelength of the excitation laser was 355 nm and the results showed that a triplet state was formed, which followed an exponential decay with a lifetime of 134 ns. In addition, the solution was exposed to UVA irradiation and HPLC data was collected which showed that vanillin dimers were formed following UVA irradiation. UVA irradiation was conducted for this work under both $O_2$ and $N_2$, with the results showing that there was less degradation under $O_2$. The authors suggested that this was due to two processes competing, namely self-quenching and oxygen quenching leading to singlet oxygen formation. Understanding vanillin's ionisation pattern using mass spectrometry, as well as its behaviour under UVB irradiation will be useful to understand not only the possible fragmentation pathways of lignin but also its potential application in sunscreen formulations.
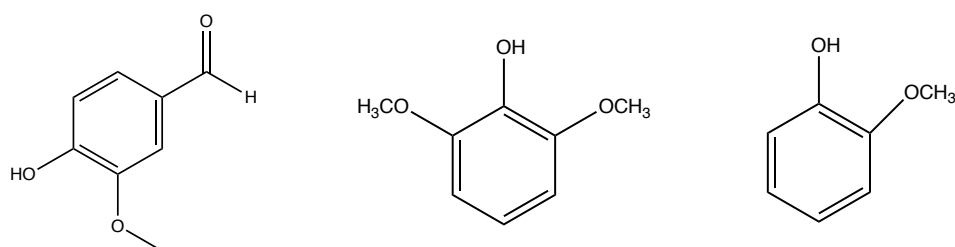


**Figure 5.1** Structures of vanillin (left), syringol (middle) and guaiacol (right)

Avobenzone is a well-studied UVA filter which is commonly found in sunscreens.[41] However, research has shown that it is photounstable following exposure to UVA irradiation. More specifically, the dominant form of avobenzone in the ground state is the

chelated enol which is a UVA absorber with a $\lambda_{max} \sim 358$ nm.[41] Dubois et al.[102] have shown that two isomers of the enol form are in equilibrium (Figure 5.2), which are stabilised by an intramolecular hydrogen bond (forming the chelated enol structure).[102,103]
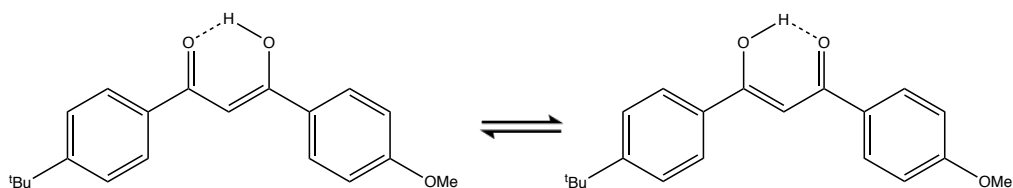


**Figure 5.2** The equilibrium in place between the two enol forms in the ground state of avobenzone.[103]

When exposed to UVA irradiation the enol converts to the keto form which is the dominant structure in the excited state and is a UVB absorber with a $\lambda_{max} \sim 266$ nm.[41] This process is shown in Figure 5.3. The effect of solvent polarity on the stabilisation of avobenzone has also been studied[103] with the data suggesting that avobenzone is more stable in polar protic solvents but tends to isomerise in polar aprotic solvents. Photodegradation can also take place and is favoured in non-polar solvents.[103] It is common to combine different chemical UV filters in a sunscreen formulation in an attempt to improve photoprotection.[33,38] It is therefore interesting to investigate whether vanillin, as a monomer of lignin would influence absorption efficiency of chemical UV filters, including ones that are acknowledged to be photounstable such as avobenzone.

Keto form

Chelated enol form
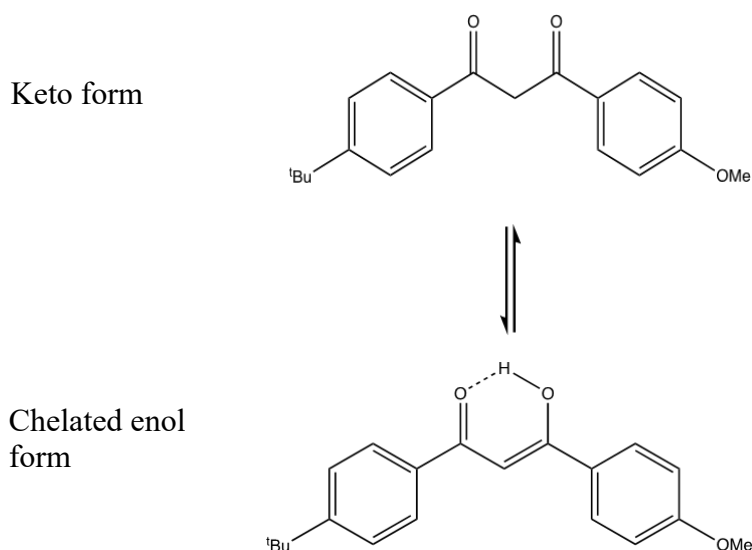


**Figure 5.3** The photoisomerisation process followed by avobenzone upon exposure to UVA irradiation.[41]

This chapter presents thermal fragmentation (collision induced dissociation) and solution phase data of vanillin to determine the extent to which it can be used as a UV filter in sunscreens. In addition, to explore the synergistic effect between vanillin and currently used chemical UV filters, absorption spectra of mixtures of OMC with vanillin and avobenzone with vanillin are presented and the effect of vanillin as a co-component on the absorbance of each UV filter is measured. Better understanding of the interaction between vanillin and the chemical UV filters on a molecular level will aid further work on the development of sunscreens that incorporate natural UV filters. Since commercial sunscreen formulations are more complex, as outlined in the introduction, additional studies on the interaction between vanillin and the bulk sunscreen mixture are required.

## 5.2 Experimental methods

Vanillin (VA), avobenzone (AB) and OMC were purchased from Sigma Aldrich and were used without further purification.

The absorption spectra of the two compounds were recorded using a Genesis 180 UV-Vis spectrophotometer (Thermo Scientific) to determine the wavelength where maximum absorption occurs ($\lambda_{max}$) and subsequently choose the appropriate photolysis cell for irradiation. Cuvettes with a 1 cm pathlength and approximately 3 mL volume were used. The absorption of VA, under UVB irradiation, was monitored at a wavelength range of 200 to 400 nm using the same UVB photolysis cell and settings outlined in Chapter 4, for two hours. The absorption of AB, under UVA irradiation, was monitored by irradiating a sample at 365 nm for 40 minutes using a custom-made UVA photolysis cell consisting of four LEDs. The voltage used for the irradiation was approximately 3.97 V. Working solutions of $1 \times 10^{-4}$ M and $1 \times 10^{-5}$ M were used for VA and AB respectively.

The absorption spectra of the sunscreen-vanillin mixtures were also recorded using a Genesis 180 UV-Vis spectrophotometer (Thermo Scientific). Stock solutions of AB and VA ($1 \times 10^{-3}$ M) were prepared in ethanol and were diluted to $1 \times 10^{-5}$ M working solutions. The mixture ratios were as follows: 1:1, 2:1, 10:1, 1:2, 1:3, 2:3, 1:5 and 1:10 avobenzone:vanillin (AB:VA). A sample from each mixture was added to a cuvette and the absorption spectrum was measured. Then, the sample was exposed to UVA irradiation at 365 nm, using the photolysis cell outlined above, for 5 minutes and the absorption spectrum was recorded again. This process was repeated every 5 minutes for a total of 30 minutes. The same mixing ratios were used for the OMC-VA mixtures. The UVB

photolysis cell was used instead and the samples were irradiated at 0, 5 and 10 s and then every 10 s until 120 s were reached.

CID data (lower energy collision induced fragmentation) on VA were collected in positive and negative ion mode using an HCT ultra ETD II mass spectrometer (Bruker Daltonics, Germany) with the following settings: positive ion mode; capillary voltage, 4200 V; dry temperature, 100°C; injection rate, 80 μL/h; nebulising gas pressure, 10.0 psi; dry gas, 5.0 l/min; accumulation time, 2 ms, negative ion mode; capillary voltage, 4500 V; dry temperature, 100°C; injection rate, 80 μL/h; nebulising gas pressure, 10.0 psi; dry gas, 5.0 l/min; accumulation time, 2 ms. Solution phase photolysis experiments were carried out in positive ion mode for VA using the same settings and with a trace amount of formic acid (ca. 10 μL) to aid ionisation efficiency. The UVB photolysis cell was used and the procedure outlined in section 4.2 was followed but data was collected at 0, 15, 30, 60 and 120 minutes.

HCD (higher-energy collision induced fragmentation) data on VA were collected on a Thermo Fisher Orbitrap Fusion$^{TM}$ mass spectrometer in the positive and negative ion mode with the following settings: positive ion mode; MS$^2$ scan isolation mode, ion trap; detector type, orbitrap; positive ion spray voltage (V), 4500; negative ion spray voltage (V), 2900; RF lens (%), 60; normalized AGC target (%), 100; maximum injection time (ms), 100; ion transfer tube temperature ( °C), 275; vaporizer temperature ( °C), 20. negative ion mode; MS$^2$ scan isolation mode, ion trap; detector type, ion trap; positive ion spray voltage (V), 4200; negative ion spray voltage (V), 2800; RF lens (%), 60; normalized AGC target (%), 100; maximum injection time (ms), 100; ion transfer tube temperature ( °C), 275; vaporizer temperature ( °C), 20. The injection flow rate was 3μL/ min.

## 5.3 Results and Discussion

### 5.3.1 Solution phase absorption of vanillin

A solution of vanillin (VA) was irradiated at 310 nm using the UVB photolysis cell described previously. Figure 5.4 displays the solution-phase absorption spectrum of VA obtained under irradiation for 120 minutes. VA's absorption decreases slightly over the irradiation period indicating that it is stable under exposure to UVB irradiation on this timescale. The absorption spectrum also reveals that VA shows significant absorption in the UVB region ($\lambda_{max}$ = 308.5 nm), appropriate for a UVB absorbing filter. This,

combined with its photostability, suggests that it has the potential to be used as a UVB filter in a sunscreen formulations. Additional $\lambda_{max}$ values are seen at $\lambda_{max}$ = 278 and 230 nm as has been reported elsewhere.[104] Figure A1.6 in Appendix A1.4 also shows a plot of the potential hydrolysis of vanillin during that time which does not seem to compete with photolysis. We can therefore conclude that VA does not degrade in aqueous solutions over the timescale studied.
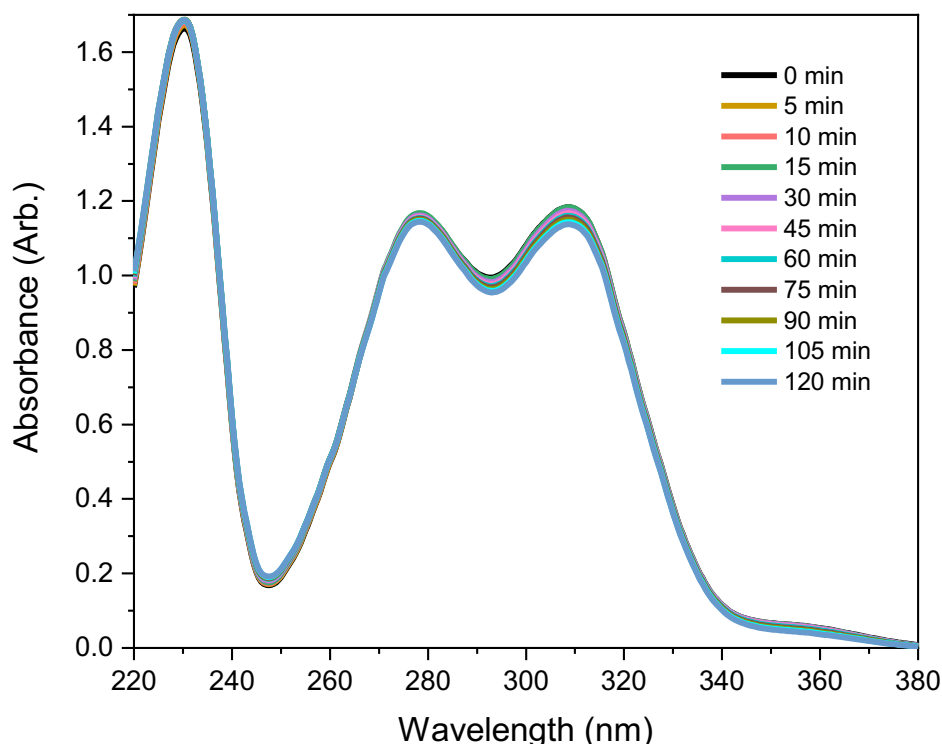


**Figure 5.4** Absorption spectrum of vanillin in ethanol following UVB irradiation at 310 nm for 120 minutes.

### 5.3.2 Solution phase photolysis of vanillin

A solution of VA was irradiated at 310 nm using a photolysis cell to investigate whether photoproducts could be detected from the photolysed solution and compare any fragments seen from the photolysed solution with the thermal fragmentation data presented in the following Section. An HCT ultra ETD II mass spectrometer (Bruker Daltonics, Germany) was used, following the method described in detail in Section 4.2. VA was electrosprayed in positive ion mode to detect [VA+H]$^+$ (m/z 153). Measurements were taken at 0, 15, 30, 60 and 120 minutes and the results are presented in Figure 5.5.
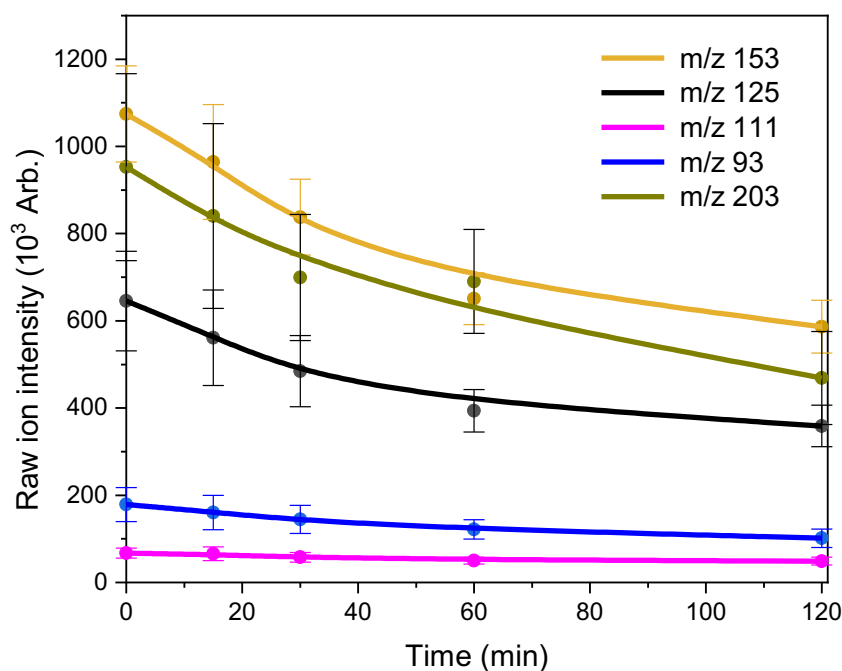
**Figure 5.5** Plot of the solution-phase photodegradation of [VA+H]$^+$ in ethanol and the photoproducts formed under UVB irradiation for 120 minutes. The solid line is a three-point adjacent average of the data and the error bars are the standard error of the mean.

Figure 5.5 shows a decrease in the amount of the electrosprayed [VA+H]$^+$ ion detected after photolysis. This is in agreement with the absorbance of VA decreasing over an increasing irradiation time, as shown in Figure 5.4, although the decrease in ion intensity looks more pronounced than the decrease in absorption. This decrease in the amount of [VA+H]$^+$seems to be faster between the start of the irradiation and 30 minutes. Other species which are potential photoproducts are also evident upon ESI-MS of the photolysed solutions, namely the species at m/z 203, 125, 111 and 93. However, the ion intensity of these potential photoproducts seems to decrease with time as well. This is not the behaviour we would expect of a photoproduct, indicating that they may be being produced through in source dissociation, rather than by photodegradation , as discussed in the previous chapter. The fact that they are also present in solution at various ion intensities at 0 minutes might also support the suggestion that they are formed through in source dissociation.

### 5.3.3 Thermal fragmentation of vanillin

The ground state thermal fragmentation of vanillin was investigated using an HCT ultra ETD II mass spectrometer (Bruker Daltonics, Germany). Figures 5.6-5.9 display the

positive ion mode data and Figures 5.10-5.13 display the negative ion mode data. As seen in Figures 5.6 and 5.7 the thermal fragments of vanillin in positive ion mode are the ones at m/z 125, 111 and 93. Only a small amount of CID energy is required for vanillin to fragment which suggests that $[VA+H]^+$ is relatively thermally unstable. It is possible that the m/z 111 and 93 fragments are secondary fragments produced from the main fragment at m/z 125 but this should become more clear when looking at the HCD data. Proposed structures for the fragments are shown in Table 5.1.



**Figure 5.6** Percent ion intensity of the thermal fragments of $[VA+H]^+$ (m/z 153) at m/z 125, 111 and 93 produced over an increasing CID energy percentage in positive ion mode. The solid line is a three-point adjacent average of the data and the error bars are the standard error of the mean.

**Figure 5.7** Raw ion intensity mass spectra (obtained in positive ion mode) of the thermal fragments of $[VA+H]^+$ at (a) 0 %, (b) 10 % and (c) 16 % CID energy.

Figures 5.8 and 5.9 display the HCD data collected in positive ion mode for $[VA+H]^+$. As with the data presented in Figure 5.6, it is evident that $[VA+H]^+$ is fragmenting when only a relatively small amount of HCD energy, around 2 %, is applied. The same thermal fragments identified upon low-energy CID (Figures 5.6 and 5.7) are present with the exception of the one at m/z 65. Based on Figure 5.8, it is evident that vanillin easily fragments into all four fragments (m/z 125, 111, 93 and 63) at different HCD energy percentages, and that the initial fragments can also break apart quite readily. This further supports the assumption that the protonated vanillin ion is thermally unstable and has low-barrier heights for molecular fragmentation.
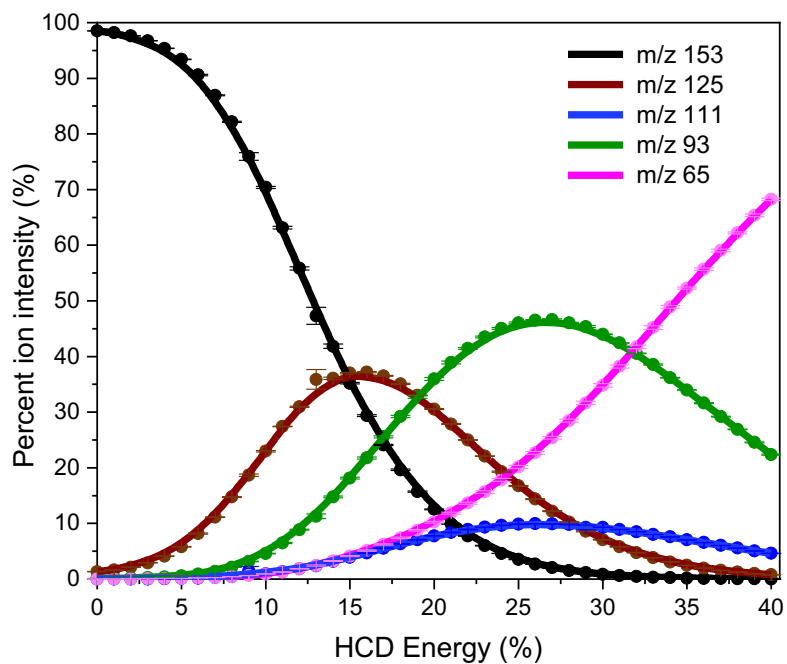
**Figure 5.8** Percent ion intensity of the thermal fragments of [VA+H]$^+$ at m/z 125, 111, 93 and 64 over an increasing HCD energy percentage in positive ion mode. The solid line is a three-point adjacent average of the data and the error bars are the standard error of the mean.

**Figure 5.9** Raw ion intensity mass spectra (obtained in positive ion mode) of the thermal fragments of $[VA+H]^+$ at (a) 0 %, (b) 15 %, (c) 30 % and (d) 40 % HCD energy.

**Table 5.1** Proposed structures for the thermal fragments [VA+H]$^+$ obtained via HCD and also of the potential photoproducts produced upon photolysis of [VA+H]$^+$ in the solution phase.

| Fragment Mass (m/z) | Proposed structure of Fragment | m/z lost from [VA+H]$^+$ | Observed in HCD[a] | Observed in solution phase photolysis[a] under UVB light |
|---|---|---|---|---|
| 125 |  | 28 | Y (s) | Y (s) |
| 111 |  | 42 | Y (w) | Y (s) |
| 93 |  | 60 | Y (s) | Y (s) |
| 65 | - | 88 | Y (s) | N |

[a] very strong (vs), strong (s), medium (m), weak (w) and very weak (vw)

Figures 5.10-5.13 display the negative ion mode thermal fragmentation data. VA, electrosprayed in negative ion mode, was detected as the deprotonated ion, [VA-H]$^-$ (m/z 151). Figures 5.10 and 5.11 summarise the lower-energy CID data collected. The only significant intensity fragment ion observed is the one the occurs at m/z 136, which is possibly formed by loss of a methyl radical.
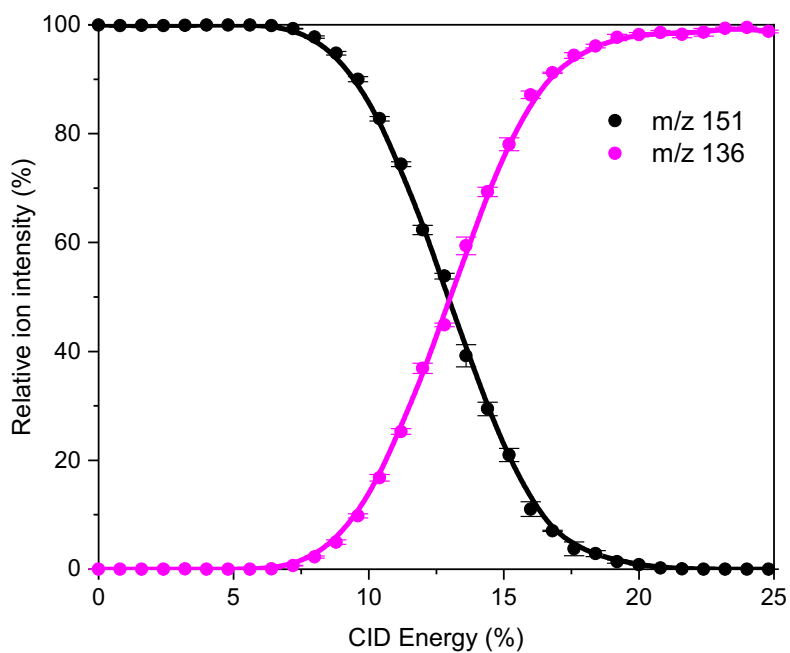
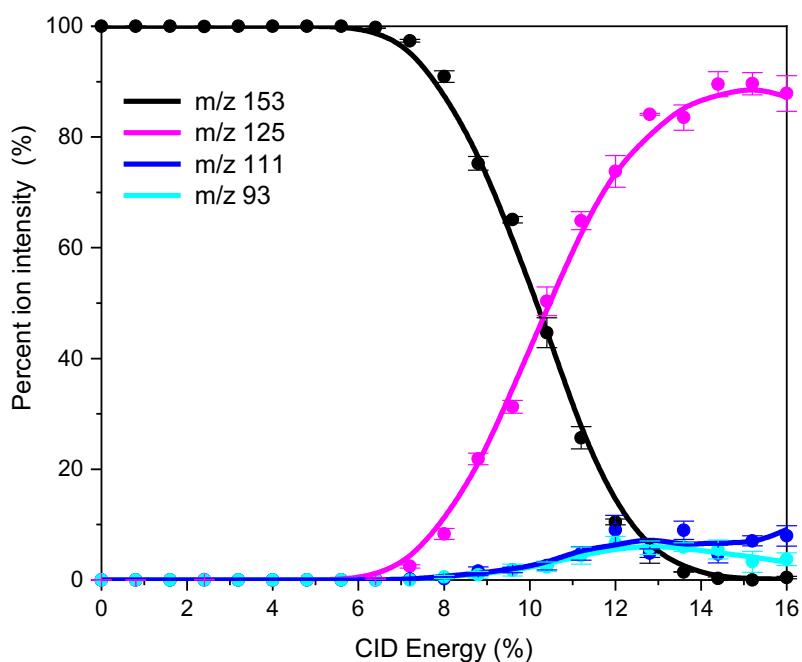**Figure 5.10** Percent ion intensity of the thermal fragment of [VA-H]⁻ (m/z 151) at m/z 136 produced over an increasing CID energy percentage in negative ion mode. The solid line is a three-point adjacent average of the data and the error bars are the standard error of the mean.
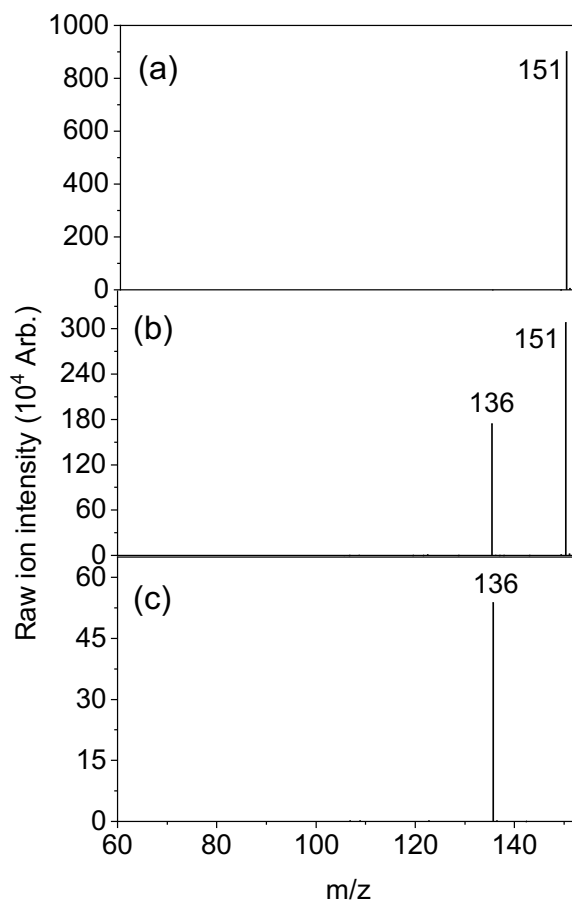
**Figure 5.11** Raw ion intensity mass spectra of the thermal fragments of [VA-H]⁻ at (a) 0 %, (b) 12 % and (c) 25 % CID energy.

Figures 5.12 and 5.13 display the HCD data collected for [VA-H]⁻. At the lower HCD energies (< 22% HCD energy), the only fragment ion observed is again the m/z 136 ion, which was also observed upon lower-energy CID. At higher HCD energies, two additional minor fragments are present, namely the ones at m/z 108 and 92, which are likely to be secondary thermal fragments produced from the m/z 136 fragment at higher internal energies. This is supported by the fact that their production onsets match the decrease in intensity of the primary m/z 136 fragment. Proposed structures for the fragments are shown in Table 5.2.
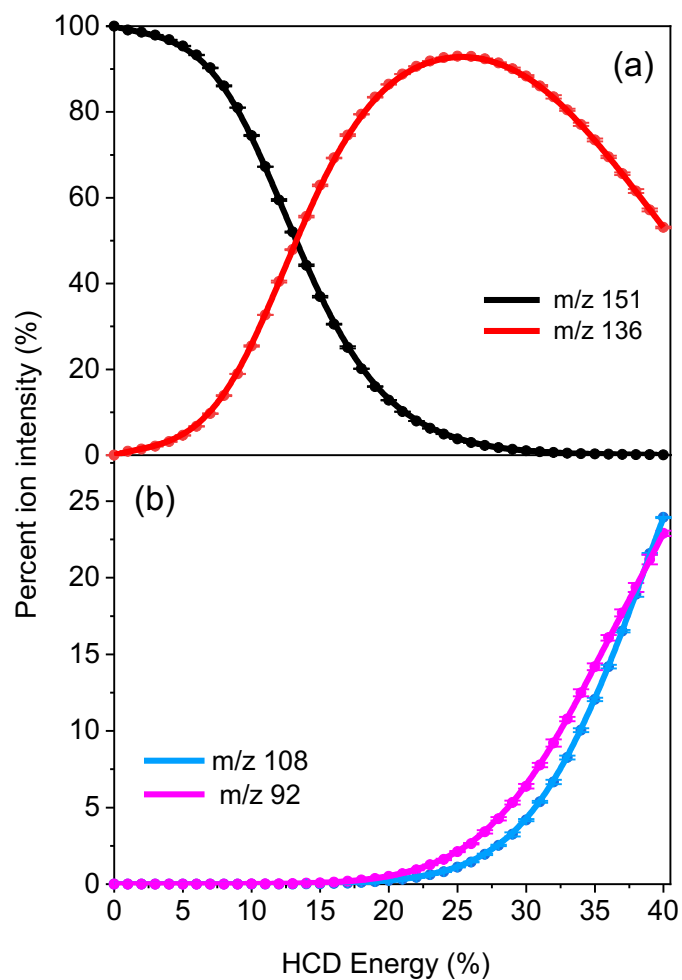
**Figure 5.12** Percent ion intensity of the (a) major and (b) minor thermal fragments of [VA-H]⁻ at m/z 136 and 108, 92, respectively, over an increasing HCD energy percentage in negative ion mode. The solid line is a three-point adjacent average of the data and the error bars are the standard error of the mean.
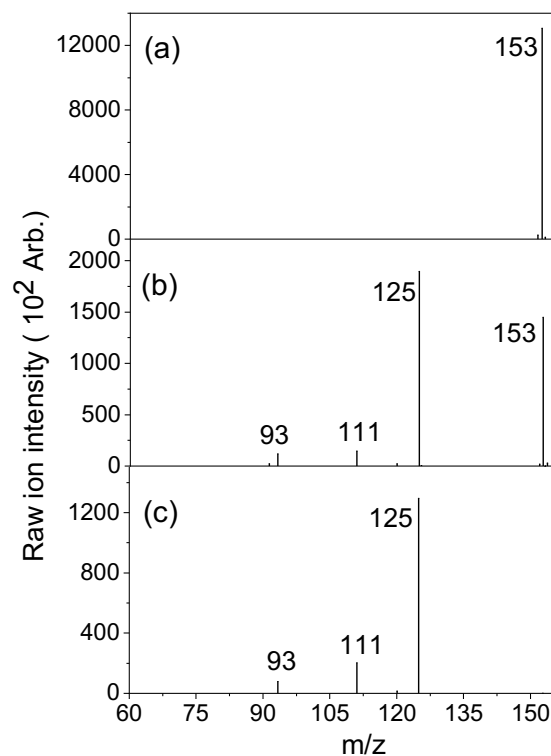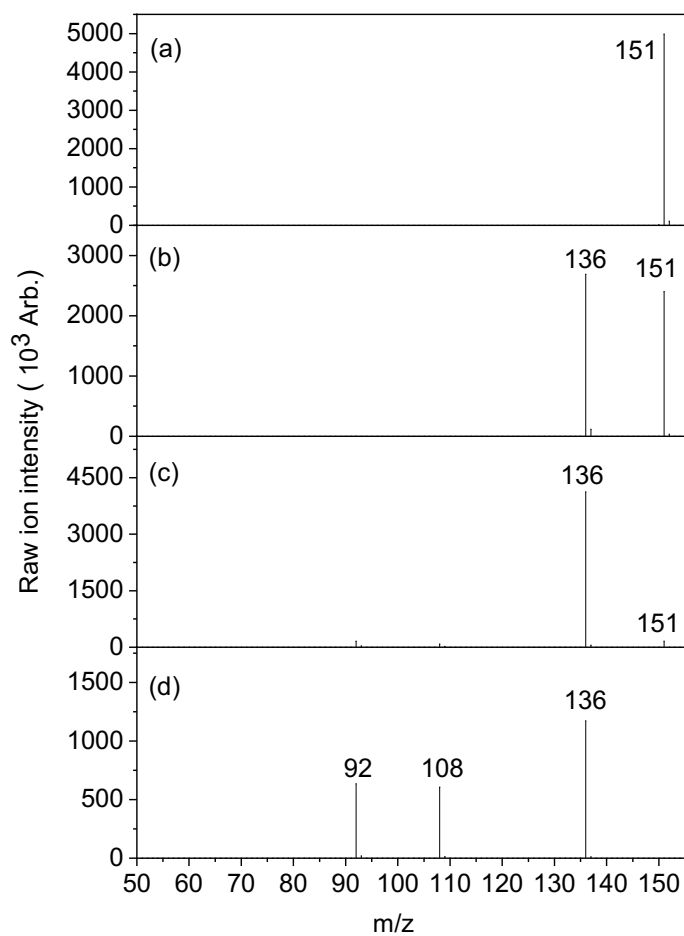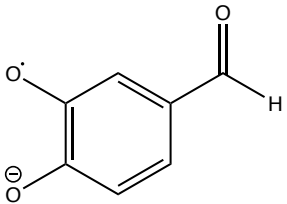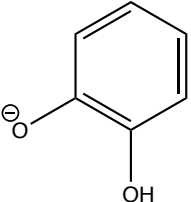
**Figure 5.13** Raw ion intensity mass spectra (obtained in negative ion mode) of the thermal fragments of [VA-H] at (a) 0 %, (b) 13 %, (c) 25 % and (d) 40 % HCD energy.

**Table 5.2** Proposed structures for the thermal fragments obtained via HCD by [VA-H]⁻.

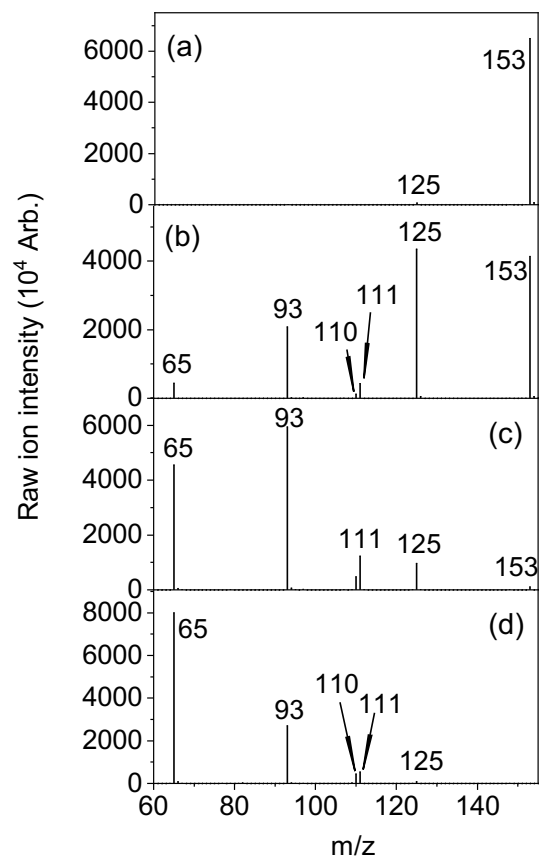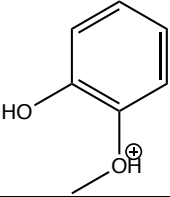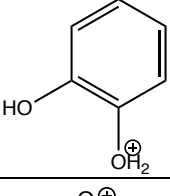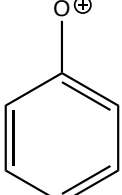| Fragment Mass (m/z) | Proposed structure of Fragment | m/z lost from [VA+H]⁺ | Observed in HCD[a] |
|---|---|---|---|
| 136 |  | 15 | Y (vs) |
| 108 |  | 43 | Y (w) |
| 92 | - | 59 | Y (w) |

[a] very strong (vs), strong (s), medium (m), weak (w) and very weak (vw)

### 5.3.4 OMC – Vanillin mixtures in ethanol

The potential synergistic effect between OMC and VA was explored by preparing mixtures of the two compounds in the following ratios: 1:1, 2:1, 10:1, 1:2, 1:3, 2:3, 1:5 and 1:10 OMC:VA. The mixtures were irradiated using the UVB photolysis cell at 310 nm for 2 minutes. The results are summarised in Figures 5.14-5.17. Figures 5.14-5.16 display overlay plots of the photodegradation of OMC, between 0 and 5 s, and VA, between 0 and 1 min, as well as of the different OMC:VA mixture ratios, between 0 and 5 s. The absorbance difference between these irradiation times was measured. This was because it is known from the work presented in the previous chapter, that when OMC is photolysed, the *cis-trans* isomerisation that takes place for OMC can lead to a decrease in absorption. Investigating the absorption difference; therefore, allows the effect of VA on the absorbance decrease to be directly investigated.

**Figure 5.14** (a) Plot of the photodegradation of OMC between 0 and 5 s. (b) Plot of the photodegradation of VA between 0 and 1 min. The lines are exactly superimposed so no photodegradation is taking place during that irradiation time. (c) Overlay plot of the photodegradation of OMC:VA mixtures with 1:1, 2:1 and 10:1 ratios between 0 and 5 s. All samples were irradiated at 310 nm using a UVB photolysis cell.

**Figure 5.15** (a) Plot of the photodegradation of OMC between 0 and 5 s. (b) Plot of the photodegradation of VA between 0 and 1 min. The lines are exactly superimposed so no photodegradation is taking place during that irradiation time (c) Overlay plot of the photodegradation of OMC:VA mixtures with 1:3, 1:2 and 2:3 ratios between 0 and 5 s. All samples were irradiated at 310 nm using a UVB photolysis cell.

**Figure 5.16** (a) Plot of the photodegradation of OMC between 0 and 5 s. (b) Plot of the photodegradation of VA between 0 and 1 min. The lines are exactly superimposed so no photodegradation is taking place during that irradiation time (c) Overlay plot of the photodegradation of OMC:VA mixtures with 1:5 and 1:10 ratios between 0 and 5 s. All samples were irradiated at 310 nm using a UVB photolysis cell.

Figure 5.17 also displays the change in absorbance at 310 nm (the $\lambda_{max}$ for OMC in ethanol) over time for the OMC:VA mixtures. For all mixtures, the absorbance decreases with an increasing irradiation time, as expected based on the fast OMC photoisomerisation. In particular for the 1:3, 1:5 and 1:10 mixtures, it is evident that the higher vanillin content in the mixture seems to stabilise OMC and slightly reduce the absorbance loss between 0 and 5 s. In addition, as seen in Figure 5.16c, the OMC:VA mixtures show small absorption in the UVA region as well, at wavelengths between 340-360 nm.
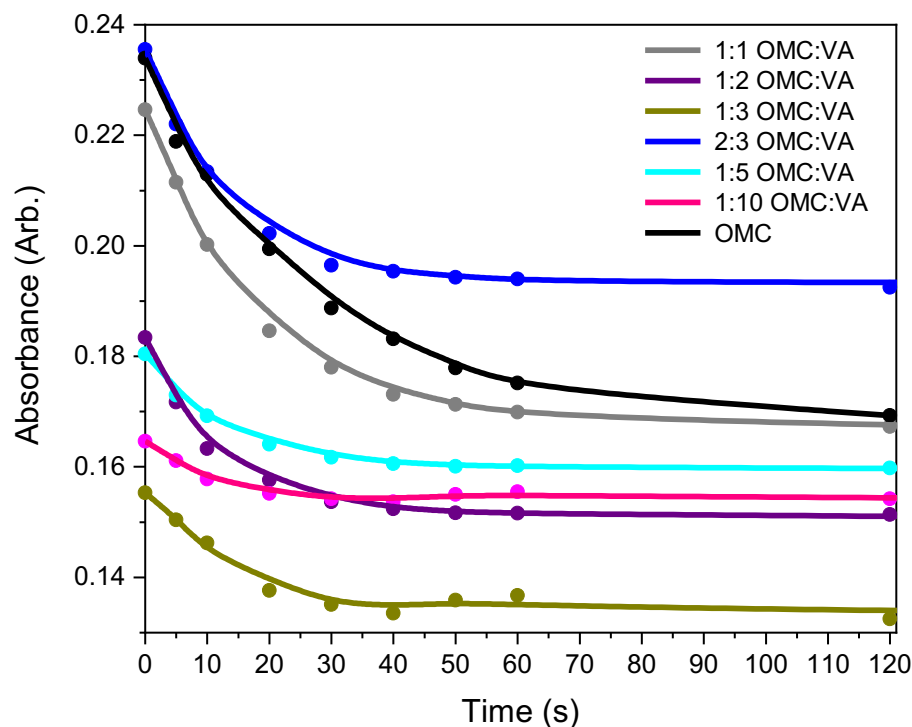
**Figure 5.17** Absorbance at 310 nm for the various OMC:VA mixtures versus OMC over irradiation at 310 nm for 120 seconds.

While a relatively small effect, this enhanced absorption in the UVA region is still evident when comparing with Figure 5.16a, which shows no absorbance in the region. Also, Figure 5.14c displays the overlay plot containing the OMC:VA mixtures where the OMC content is higher and no absorption in that region of UVA radiation is present either. This is not as clear in the intermediate mixtures displayed in Figure 5.15c. This observation is in agreement with findings from Qian et al.[49] who studied mixtures of OMC with OL lignin in dioxane and glycol solution. The authors concluded that the improved UV coverage is due to J-aggregate formation between OMC and OL which resulted in lowering of the energy in the π-π* transition required for UVA energy absorption. Based on the shape of the absorption spectra of the mixtures, in Figures 5.15c and 5.16c, it is likely that complexes might be formed, as the shape looks intermediate between the two separate species, but this cannot be inferred based on this experiment alone.

### 5.3.5 Avobenzone – Vanillin mixtures in ethanol

The synergistic effect between AB and VA was also explored by preparing mixtures of the two compounds in the following ratios: 1:1, 2:1, 10:1, 1:2, 1:3, 2:3, 1:5 and 1:10 AB:VA. The samples were exposed to UVA irradiation at 365 nm using the UVA photolysis cell and the absorption spectra were recorded every 5 minutes for a total of 30 minutes. The absorption spectrum of avobenzone in ethanol under this irradiation time is shown in Appendix A1.5, Figure A1.7. The results are summarised in Figures 5.18-5.21. Figures 5.18-5.20 display overlay plots of the photodegradation of AB, between 0 and 10 min, and VA, between 0 and 10 min, as well as of different AB:VA mixture ratios, between 0 and 10 min.
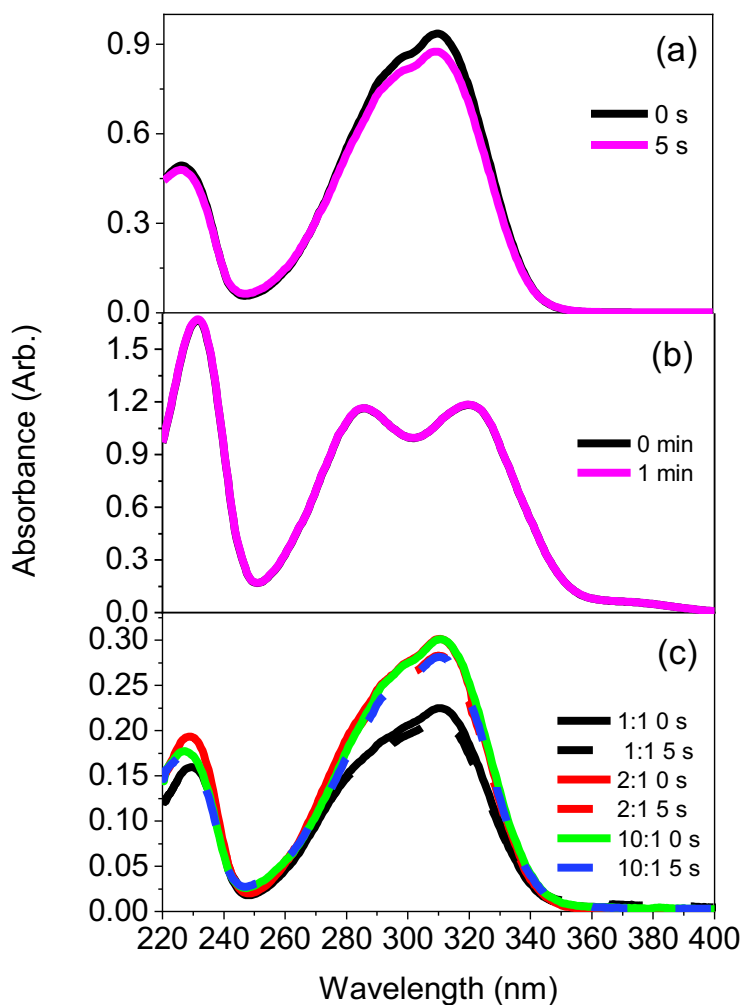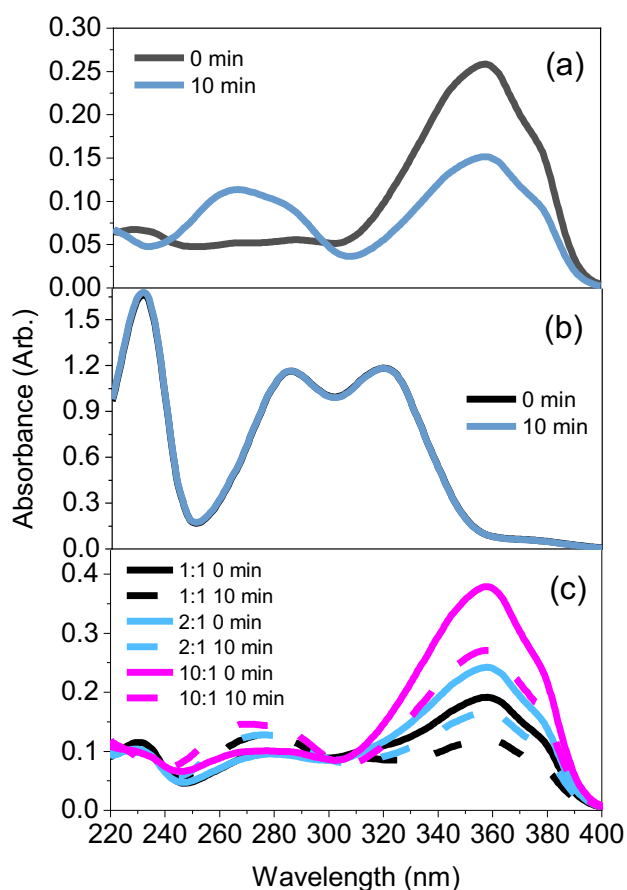


**Figure 5.18** (a) Plot of the photodegradation of AB between 0 and 10 min. (b) Plot of the photodegradation of VA between 0 and 10 min. The lines are exactly superimposed so no photodegradation is taking place during that irradiation time (c) Overlay plot of the photodegradation of AB:VA mixtures with 1:1, 2:1 and 10:1 ratios between 0 and 10 min. All samples were irradiated at 365 nm using a UVA photolysis cell.
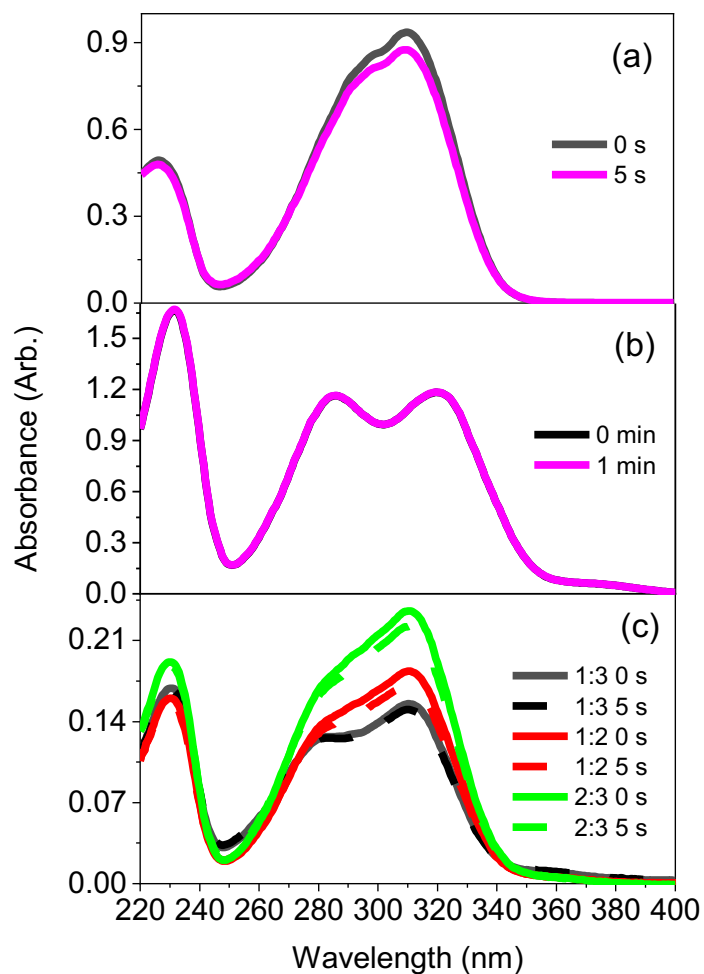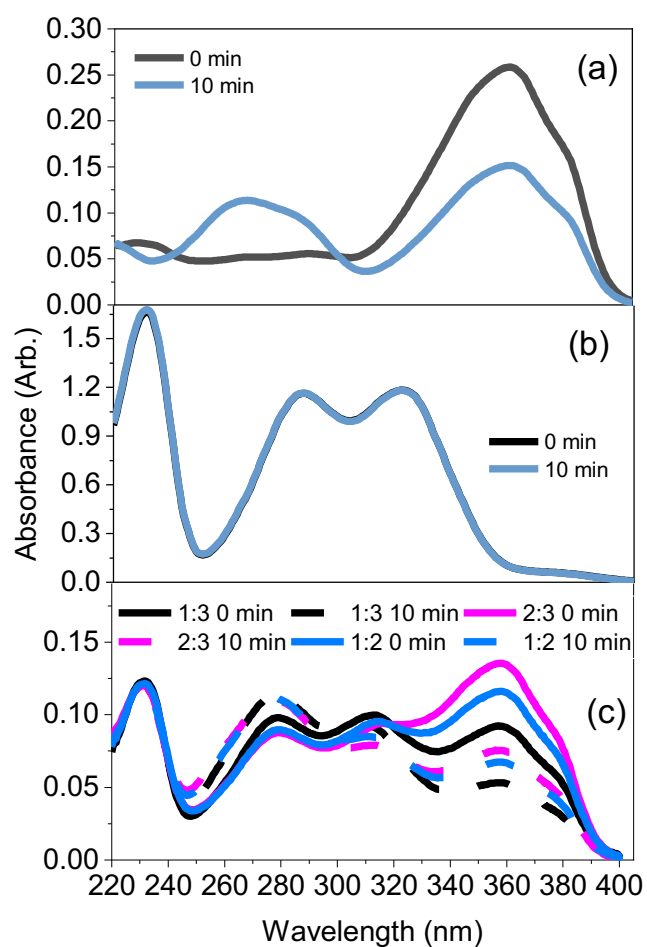
**Figure 5.19** (a) Plot of the photodegradation of AB between 0 and 10 min. (b) Plot of the photodegradation of VA between 0 and 10 min. The lines are exactly superimposed so no photodegradation is taking place during that irradiation time (c) Overlay plot of the photodegradation of AB:VA mixtures with 1:3, 2:3 and 1:2 ratios between 0 and 10 min. All samples were irradiated at 365 nm using a UVA photolysis cell.
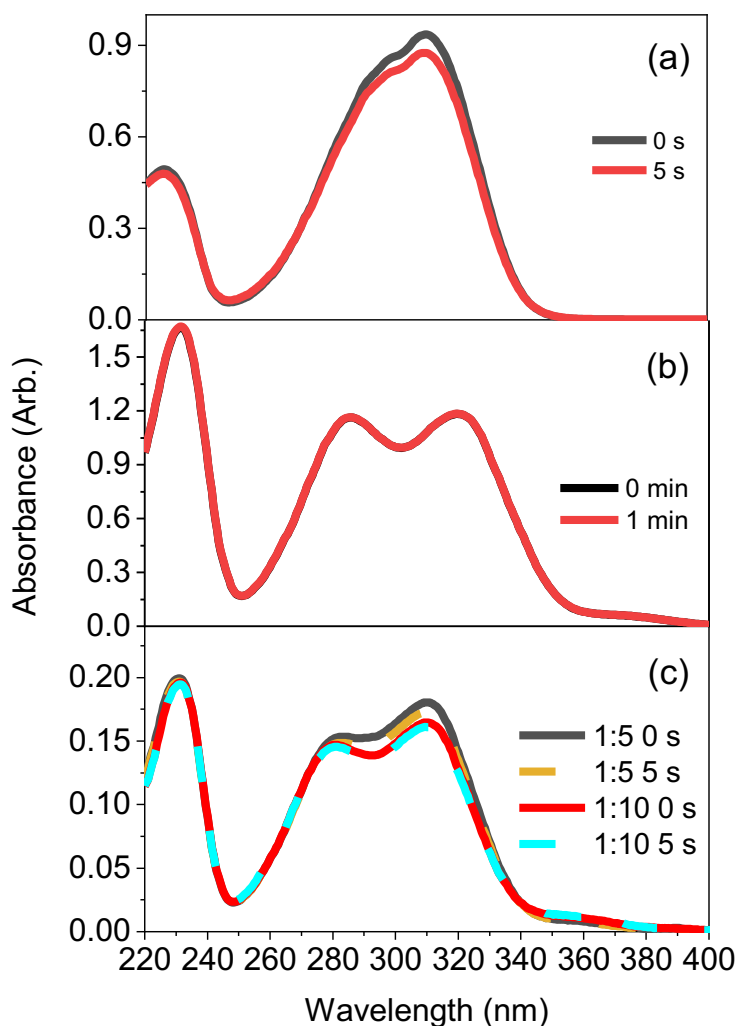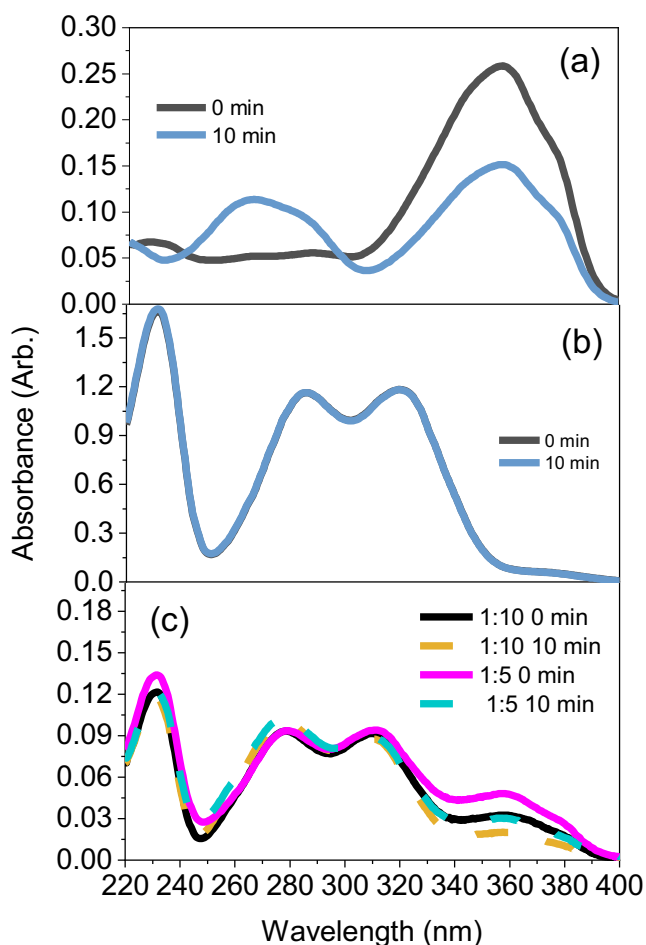
**Figure 5.20** (a) Plot of the photodegradation of AB between 0 and 10 min. (b) Plot of the photodegradation of VA between 0 and 10 min. The lines are exactly superimposed so no photodegradation is taking place during that irradiation time (c) Overlay plot of the photodegradation of AB:VA mixtures with 1:10 and 1:5 ratios between 0 and 10 min. All samples were irradiated at 365 nm using a UVA photolysis cell.

Figure 5.21 also displays the change in absorbance at 358 nm (the $\lambda_{max}$ for ground state chelated enol form of AB in ethanol). As with the OMC:VA mixtures, as the VA content increases in the mixtures studied, the absorbance difference between 0 and 10 minutes becomes smaller. This shows that VA acts as a stabiliser for AB. When looking at Figures 5.18c-5.20c, it is evident that mixing the two compounds results in a broader UV coverage, both in the UVA and UVB regions, which is also highly desirable for a sunscreen filter. Similar to the OMC:VA mixtures, the shape of the overall spectral profile resembles the compound that is present at higher concentration in the mixture. This effect is clearer in Figures 5.18c and 5.20c, where the mixtures have a higher component of AB and VA, respectively. Lastly, the peak at around 270 nm could correspond to a complex

formed between the keto form of AB and VA, as it is intermediate between the two species, which could also be responsible for the improved absorbance in the UVB region for the mixture.
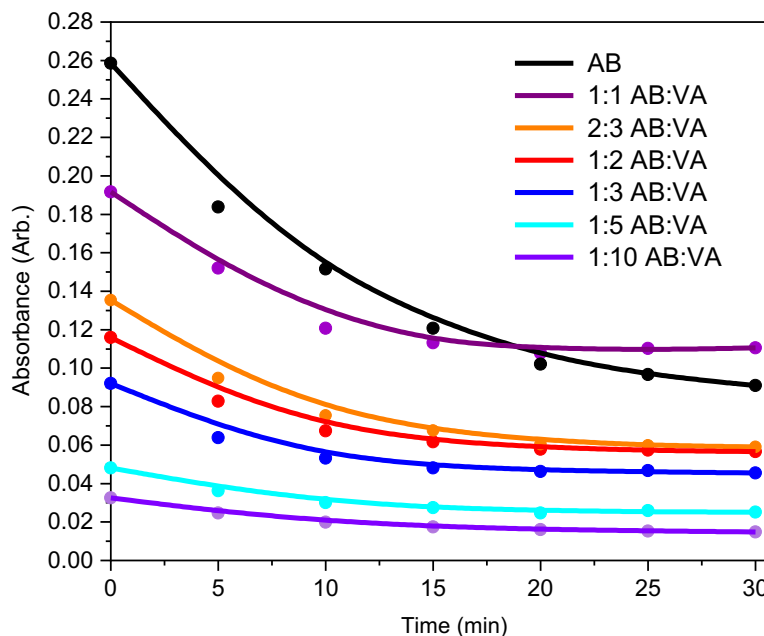


**Figure 5.21** Absorbance at 358 nm for the various AB:VA mixtures versus AB over irradiation at 365 nm for 30 minutes.

Nevertheless, it is not possible to deduce the nature of the complex formed based on this experiment alone. The absorption spectrum of VA under UVA irradiation at 365 nm was also recorded to determine whether the increase in absorbance at around 270 nm is due to VA possibly breaking down into UVA absorbing species or just a result of the mixture. The plot is displayed in Appendix A1.6, Figure A1.8. A slight increase in absorbance is observed after exposure to UVA irradiation, but it was considered negligible.

## 5.4 Concluding remarks

The work presented in this chapter aimed to investigate whether Vanillin (VA), a lignin monomer, would be a suitable UVB filter for sunscreens, due to its broad UVB coverage and stability under UVB irradiation. Its thermal gas-phase fragmentation pattern (obtained via CID) showed it can be quite thermally unstable. The solution phase photodegradation data, while showing that some photoproducts are present upon exposure to UVB irradiation, did not establish whether these species were actually photoproducts or thermal fragments, as discussed in Chapter 4.

The photodegradation of mixtures of VA with OMC and AB was also explored using UV-VIS spectroscopy, under UVB and UVA irradiation respectively. It was found that a higher VA content led to increased photostability under irradiation in the time frames studied for the mixtures. A mixture of VA with the other organic sunscreens also provided a broader UV coverage compared to the isolated chemical UV filters. This further supports the recent reports that a combination of lignin and chemical UV filters could be beneficial in sunscreen formulations.[48,49,105] The presence of complexes (aggregates) between the two species might potentially be responsible for this increased photostability. Unfortunately, it was not possible to obtain ESI-MS of the photolysed solutions of VA mixed with OMC and AB to explore how the identity of any photoproducts changed in the mixed solutions compared to single component solutions. This was due to the limited time available across this master's project, particularly given that much of it happened when lab occupancy was limited due to the pandemic. However, it would be interesting to investigate this in future work.

Further research on the nature of synergistic effects of VA and other lignin monomers is required given the results presented here. LIMS experiments, would be beneficial to provide clear information on the electronic properties of complexes of mixed VA clusters, e.g. VA·OMC and VA·AB. Computational studies would also be useful as they would provide detailed insight into how the electronic spectra of the individual chromophores are affected within a mixed complex. Such calculations should be conducted on different complex molecular geometries to probe whether this affects the absorption properties, as suggested by Qian et al.[49]

# Chapter 6

## Further work

This thesis aimed firstly to investigate the photodegradation of organic sunscreen UV filters in the gas phase and in solution, in an attempt to demonstrate new methods for identifying photoproducts, and hence providing new information to assess the photostability of organic sunscreens. We have focused here on the well characterised sunscreen molecules, OMC and OD-PABA, which have previously been studied both experimentally and computationally. This allowed us to benchmark the new methods trialled here against the previous results.

Laser-interfaced mass spectrometry (LIMS) was applied to OMC in the work presented in Chapter 3, and the results showed that it was a useful tool for identifying photoproducts, since the gas-phase photoproducts identified by LIMS, matched those observed in solution previously. This result agrees with recent results from our research group on the photodegradation of riboflavin, where the observed LIMS photoproducts matched those seen upon solution photolysis.[79] LIMS is a much more straightforward technique than solution-phase photolysis in identification of photoproducts, as the molecule to be studied is mass selected prior to photolysis. This means that any photoproducts observed must have arisen from this molecule. In solution, the presence of solvent, counterions, etc can complicate the photochemistry considerably. For the current thesis work, it was not possible to use LIMS to study OD-PABA due to time constraints, but it would be interesting to perform this study in future work, to provide further evidence of the utility of LIMS for identifying photoproducts.

In addition to gas-phase LIMS experiments, solution-phase photolysis experiments on OMC and OD-PABA were also conducted, with results presented in Chapter 4. Traditionally, such experiments have been conducted on relatively large volume solutions (>0.5 litre) using mercury UV lamps.[34] These lamps have a high energy requirement, and also require mercury in their production, which is a harmful waste product when the lamps expire. For our experiments, we used LED UVA and UVB diode setups to photolyse small volumes of sunscreen solutions. This is a much greener solution, which uses less chemicals, less solvent and less energy to achieve the photolysis experiments. Using our new approach, we were able to detect the same photoproducts using electrospray ionisation as have previously been seen using LC-MS.

In addition, in Chapter 4, a series of detailed mass spectrometry studies were also presented on OMC and OD-PABA, electrosprayed in positive ion mode. These were performed to better understand the breakdown of these molecules through the electrospray process. We found that fragments that were previously identified as "photoproducts" were also associated with thermal break up of these molecules. This leads us to question the previous results and illustrates the importance of fully characterising the analytical technique employed for detecting low concentration species such as photoproducts. While mass spectrometry is known as a highly sensitive technique for analysis of complex mixtures, our work shows that it is important to perform careful control measurements as a part of developing protocols for photoproduct identification.

The other topic this thesis aimed to explore was the potential use of the lignin monomer, vanillin, as a natural UVB filter in sunscreens. LIMS experiments on the protonated and deprotonated forms of VA in the gas phase would be useful to mirror the pH environment the filter could perform in. More specifically, the skin is slightly acidic[106] (pH = 5), whereas chlorinated swimming pool water (pH ~ 7.3) and seawater (pH = 8) are alkaline.[107] As discussed in Chapter 5, the results were promising in terms of VA's photostability, and highlight the potential for future use of such bio-available sunscreen molecules. Apart from the LIMS experiments and computational calculations on the complexes of OMC-VA and AB-VA, as discussed in Chapter 5, it would be interesting to study their photodegradation in solution, using a different light source to the photolysis cells employed for the experiments in this thesis, such as a full solar simulator. Overall, research on the synergistic effect between lignin and chemical UV filters is still limited, and more work is clearly warranted to better understand the fundamental physical chemistry at work in this system.

Certain challenges regarding the use of lignin in sunscreens have been identified, such as the dark colour of the polymer.[23,47] While this can be slightly altered via acetylation[105] or UV irradiation,[108] the UV absorbing properties of lignin could be affected. Nevertheless, this could also lead to the development of tinted products which would be beneficial for some areas of the commercial sunscreen market.[47] Lastly, an area that has attracted attention is the incorporation of lignin nanoparticles in sunscreens.[23,47] Li et al.[109] reported that nano-structured lignin shows a 30 % increase in UV protection compared to the regular sized polymer. Additionally, results by Wang et al.[105] indicated that there was an increase of 115 % on the SPF value of pure cream studied when 5 % of lignin nanoparticles were added. It is therefore evident that further research into lignin

nanoparticles is worthwhile, as it could lead to significant advances in sunscreen formulations.

# Appendix

## A1.1 Photofragment (PF) production intensity of the minor photofragments produced by [OMC+H]$^+$ in the gas phase.
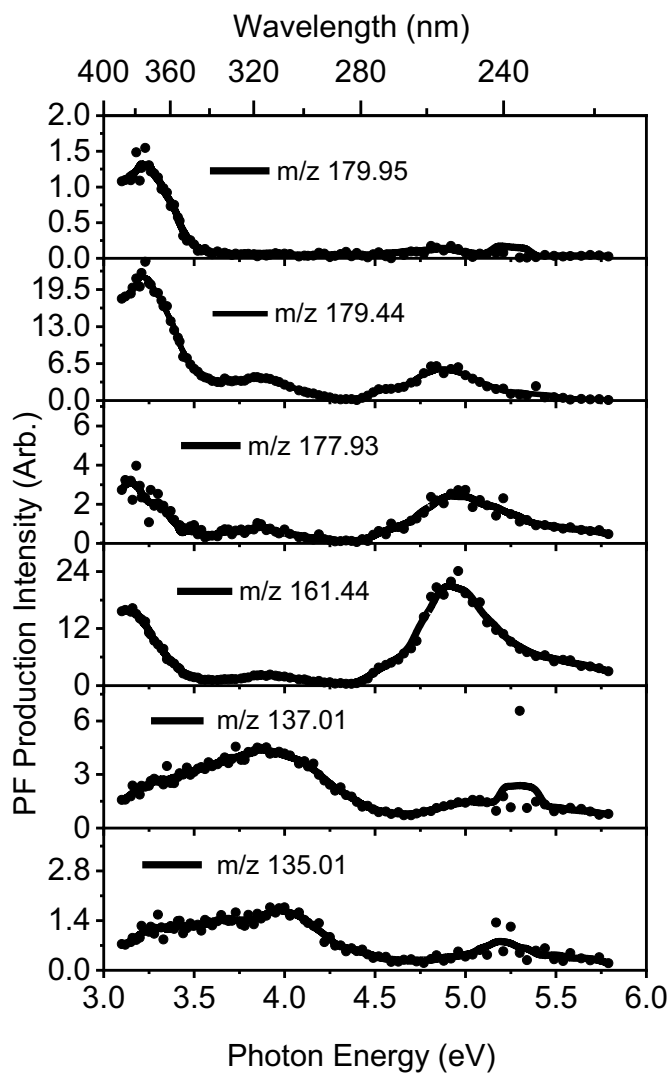


**Figure A1.1** Photofragment production intensity of the minor fragments of [OMC.H]$^+$ (m/z 179.95, 179.44, 177.93, 161.44, 137.01 and 135.01). The solid line is a five-point adjacent average of the data points.
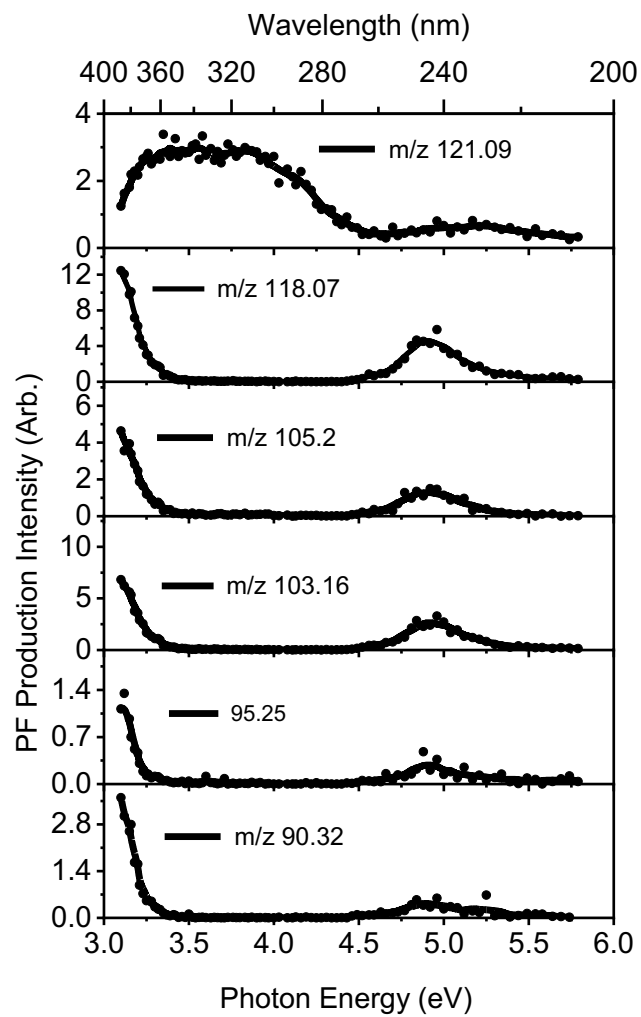
**Figure A1.2** Photofragment production intensity of the minor fragments of [OMC.H]$^+$ (m/z 121.09, 118.07, 105.2, 103.16, 95.25 and 90.32). The solid line is a five-point adjacent average of the data points.
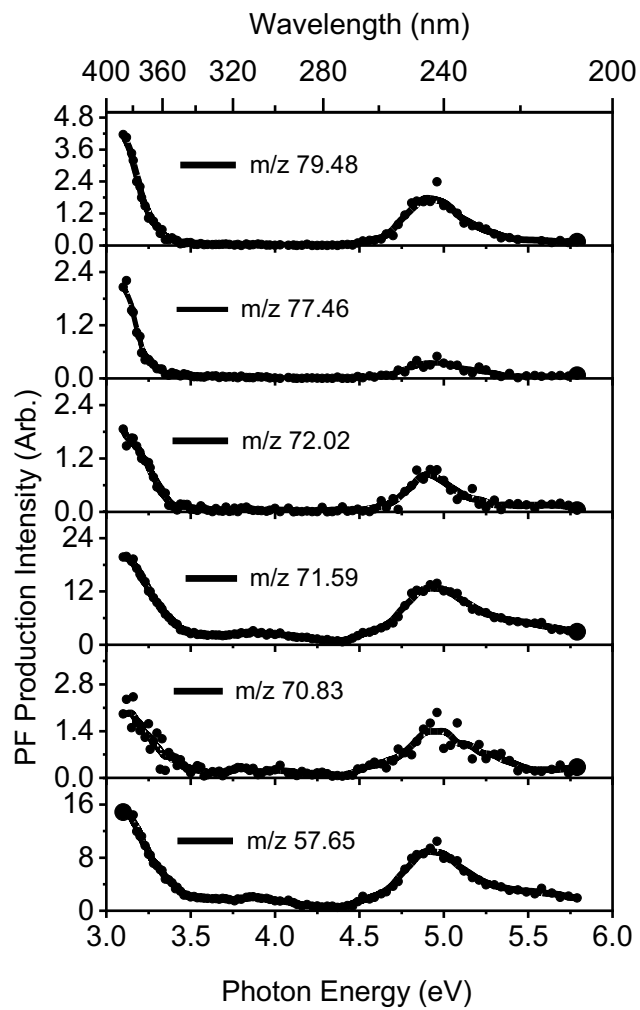
**Figure A1.3** Photofragment production intensity of the minor fragments of [OMC.H]$^+$ (m/z 79.48, 77.46, 72.02, 71.59, 70.83 and 57.65). The solid line is a five-point adjacent average of the data points.

## A1.2 Hydrolysis of OMC in ethanol

As seen in Figure A1.2 no hydrolysis takes place for OMC over 20 minutes, so it is not competing with the photolysis process studied.
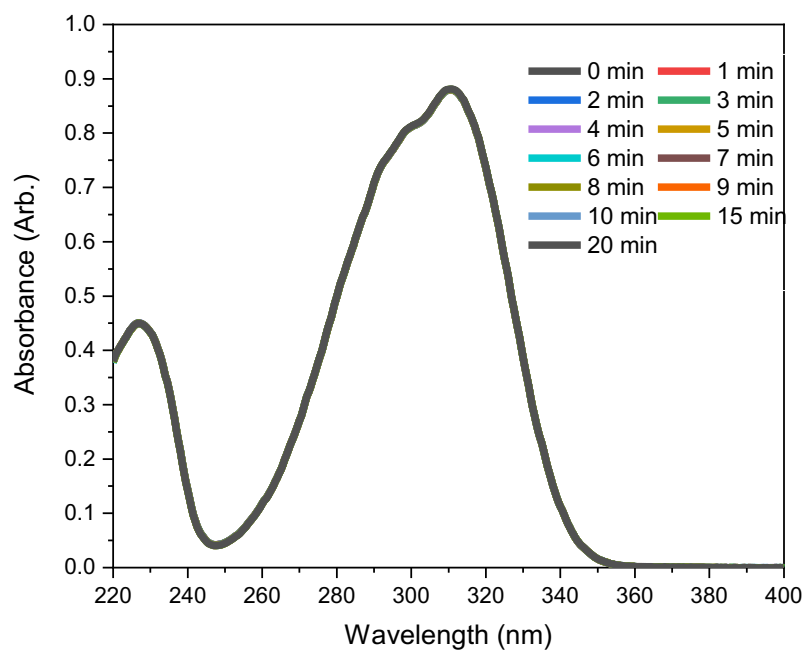


**Figure A1.4** Absorption spectrum showing hydrolysis of OMC in ethanol over a period of 20 minutes.

## A1.3 Hydrolysis of OD-PABA in ethanol

As seen in Figure A1.5, OD-PABA seems to hydrolyse over the 7-hour period studied, since its absorbance shows a slight increase. It is not clear whether this is due to the molecule breaking down into UV absorbing fragments or poor instrument calibration. Nevertheless, it does not seem to compete with the photolysis process studied.
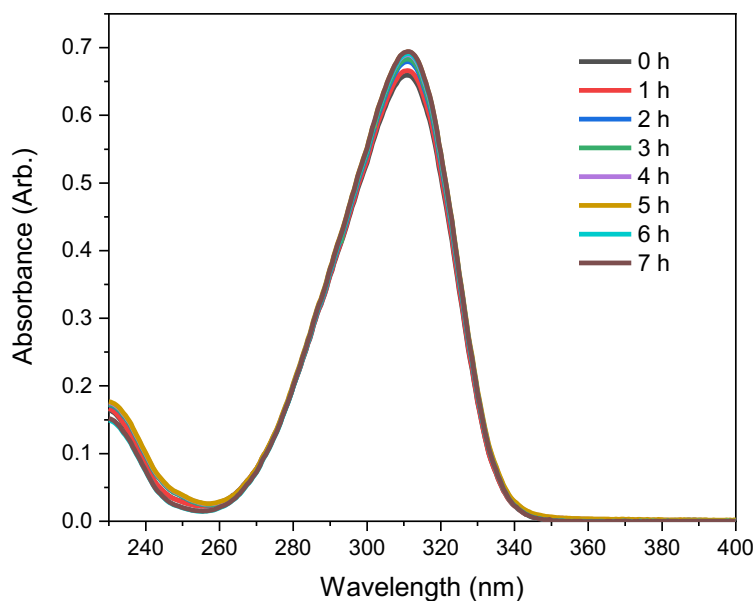


**Figure A1.5** Absorption spectrum showing hydrolysis of OD-PABA in ethanol over a period of 7 hours.

## A1.4 Hydrolysis of Vanillin in ethanol

As seen in Figure A1.6, VA seems to hydrolyse over the 120-minute period studied, as its absorbance increases slightly. As with OD-PABA (Figure A1.5), it is not clear whether this is due to the molecule breaking down into UV absorbing fragments or poor instrument calibration. Nevertheless, it does not seem to compete with the photolysis process under investigation.
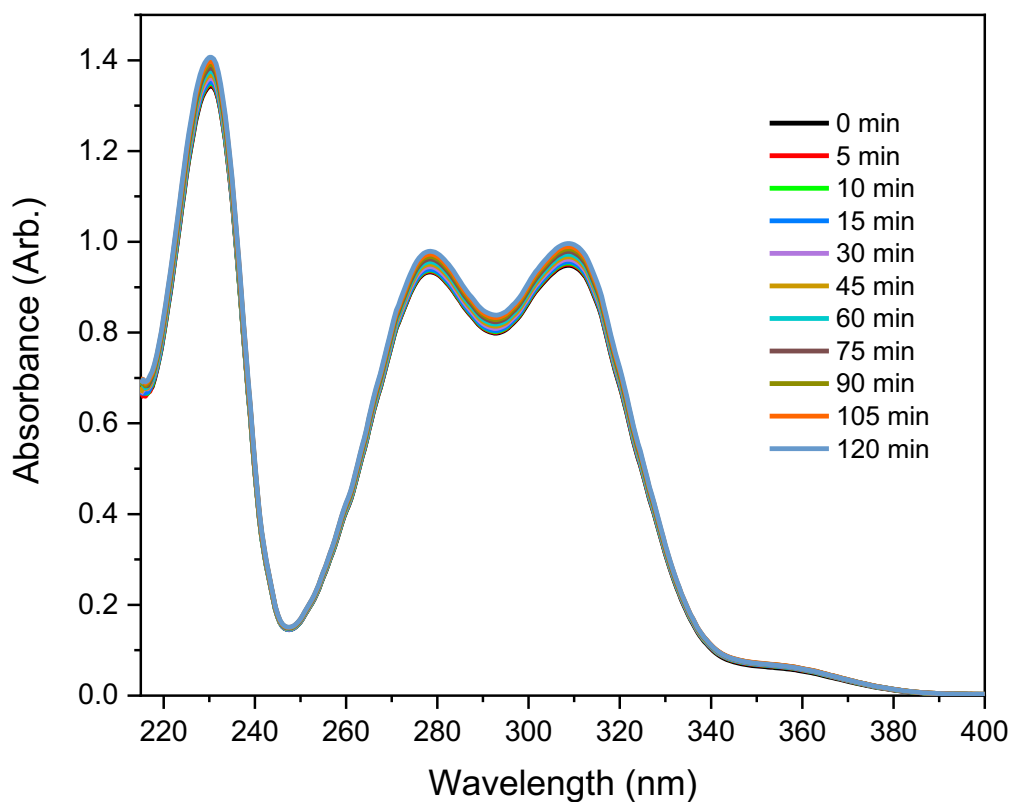


**Figure A1.6** Absorption spectrum showing hydrolysis of VA in ethanol over a period of 120 minutes.

## A1.5 Photodegradation of AB in ethanol under UVA irradiation

Figure A1.7 shows the photodegradation of AB in ethanol under UVA irradiation at 365 nm for 30 minutes. As seen in Figure A1.7, AB is photounstable following exposure to UVA irradiation. More specifically, the dominant form of avobenzone in the ground state is the chelated enol which is a UVA absorber with a $\lambda_{max} \sim 358$ nm. When exposed to UVA irradiation the enol converts to the keto form which is the dominant structure in the excited state and is a UVB absorber with a $\lambda_{max} \sim 266$ nm.[41]
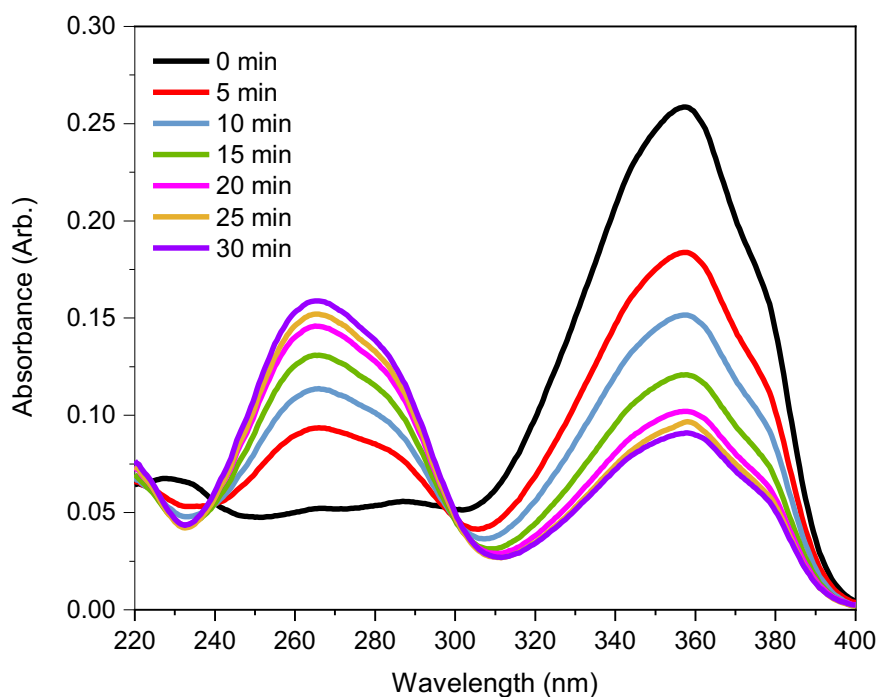


**Figure A1.7** Absorption spectrum showing the photodegradation of AB in ethanol under UVA irradiation at 365 nm for 30 minutes.

.

## A1.6 Photodegradation of VA in ethanol under UVA irradiation

Figure A1.8 shows the photodegradation of VA under UVA irradiation 365 nm for 60
minutes. The absorbance of VA increases slightly but this increase was considered
negligible.
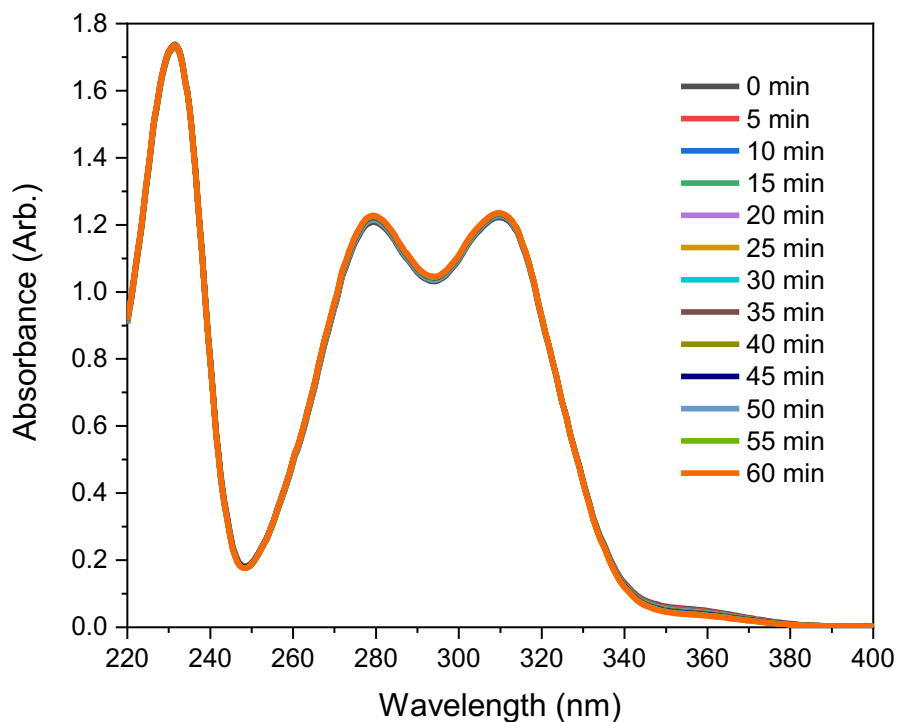


**Figure A1.8** Absorption spectrum showing the photodegradation of VA in ethanol under UVA
irradiation at 365 nm for 60 minutes.

# List of abbreviations

IR – Infrared

IC – Internal conversion

OMC – Octylmethoxycinnamate

AB – Avobenzone

OD-PABA – Ethylhexyl diethylamino benzoate

OC – Octocrylene

DHHB – Diethylamino hydroxybenzoyl hexyl benzoate

EHS – Ethylhexyl salicylate

BEMT – Bis ethylhexyloxyphenol methoxyphenyl triazine

OB – Oxybenzone

PBSA – 2-phenylbenzimidazole-5-sulfonic acid

BP4 – Benzophenone-4

CMA – *trans* para coumaric acid

CA – *trans* caffeic acid

FA – *trans* ferulic acid

VA – Vanillin

NPs – Nanoparticles

ESI – Electrospray Ionization

ESI-MS – Electrospray Ionization- Mass Spectrometry

LC-MS – Liquid chromatrography-Mass Spectrometry

HPLC – High performance liquid chromatrography

CID – Collision Induced Dissociation

CRM – Charge Residue Model

HCD – Higher Energy Collisional Dissociation

IEM – Ion Evaporation Model

LIMS – Laser Interfaced Mass Spectrometer

DFT – Density Functional Theory

IRMPD – Infrared multiple photon dissociation

OL – Organosolv lignin

SM – Sinapoyl malate

TEAS – Transient electronic absorption spectroscopy

TVAS – Transient vibrational absorption spectroscopy

ACN – Acetonitrile

CI – Conical intersection

ESI-QIT – Electrospray ionisation quadrupole ion trap

PD – Photodepletion

PF – Photofragment

MS/MS – Tandem mass spectrometry

QIT – Quadrupole

LEDs – Light emitting diodes

RE2PI – Resenonace enhanced two-photon ionisation

LIF – Laser induced fluorescence

HB – UV-UV hole burning

DOM – Dissolved organic matter

HOMO – Highest occupied molecular orbital

LUMO – Lowest unoccupied molecular orbital

POV – Persistence in the environment

LRTP – Long-range transport potential

# References

1    G. P. Pfeifer and A. Besaratinia, *Photochem. Photobiol. Sci.*, 2012, **11**, 90–97.

2    Skin cancer statistics: melanoma of the skin is the 19th most common cancer worldwide, https://www.wcrf.org/dietandcancer/cancer-trends/skin-cancer-statistics, (accessed 21 March 2021).

3    Global Coalition for Melanoma Patient Advocasy and Euro Melanoma, 2020 Melanoma Skin Cancer Report, Stemming the global epidemic, https://melanomapatients.org.au/wp-content/uploads/2020/04/2020-campaign-report-GC-version-MPA_1.pdf, (accessed 23 November 2021).

4    L. A. Baker and V. G. Stavros, *Sci. Prog.*, 2016, **99**, 282–311.

5    J. D'Orazio, S. Jarrett, A. Amaro-Ortiz and T. Scott, *Int. J. Mol. Sci.*, 2013, **14**, 12222–12248.

6    M. Cichorek, M. Wachulska, A. Stasiewicz and A. Tymińska, *Adv. Dermatology Allergol.*, 2013, **1**, 30–41.

7    R. E. Neale, S. R. Khan, R. M. Lucas, M. Waterhouse, D. C. Whiteman and C. M. Olsen, *Br. J. Dermatol.*, 2019, **181**, 907–915.

8    L. Y. Matsuoka, J. Wortsman and N. Hanifan, *Arch. Dermatol.*, 1988, **124**, 1802.

9    J. J. Neville, T. Palmieri and A. R. Young, *JBMR Plus*, , DOI:10.1002/jbm4.10460.

10    R. M. Lucas, S. Yazar, A. R. Young, M. Norval, F. R. de Gruijl, Y. Takizawa, L. E. Rhodes, C. A. Sinclair and R. E. Neale, *Photochem. Photobiol. Sci.*, 2019, **18**, 641–680.

11    R. Jansen, U. Osterwalder, S. Q. Wang, M. Burnett and H. W. Lim, *J. Am. Acad. Dermatol.*, 2013, **69**, 867.e1-867.e14.

12    U. Osterwalder, M. Sohn and B. Herzog, *Photodermatol. Photoimmunol. Photomed.*, 2014, **30**, 62–80.

13    A. Steinemann, *Air Qual. Atmos. Heal.*, 2019, **12**, 891–897.

14    L. A. Baker, B. Marchetti, T. N. V. Karsili, V. G. Stavros and M. N. R. Ashfold, *Chem. Soc. Rev.*, 2017, **46**, 3770–3791.

15    E. M. M. Tan, M. Hilbers and W. J. Buma, *J. Phys. Chem. Lett.*, 2014, **5**, 2464–2468.

16    S. Forestier, *J. Am. Acad. Dermatol.*, 2008, **58**, 133–138.

17    C. Mylonas and D. Kouretas, *In Vivo*, **13**, 295–309.

18    K. M. Hanson, E. Gratton and C. J. Bardeen, *Free Radic. Biol. Med.*, 2006, **41**, 1205–1212.

19    Y. T. Cho, H. Su, I. C. Huang, C. Y. Lai and Y. Da Tsai, *Anal. Methods*, 2019, **11**, 6013–6022.

20    Directorate-General for Internal Market; Industry;Entrepreneurship and SMEs, Cosmetic ingredient database (Cosing) - List of UV filters allowed in cosmetic products, https://data.europa.eu/data/datasets/cosmetic-ingredient-database-list-of-uv-filters-allowed-in-cosmetic-products?locale=en, (accessed 28 November 2021).

21    S. Narla and H. W. Lim, *Photochem. Photobiol. Sci.*, 2020, **19**, 66–70.

22    N. Sabzevari, S. Qiblawi, S. A. Norton and D. Fivenson, *Int. J. Women's Dermatology*, 2021, **7**, 28–44.

23    M. H. Tran, D.-P. Phan and E. Y. Lee, *Green Chem.*, 2021, **23**, 4633–4646.

24    T. G. Smijs and S. Pavel, *Nanotechnol. Sci. Appl.*, 2011, **4**, 95–112.

25    M. E. Burnett and S. Q. Wang, *Photodermatol. Photoimmunol. Photomed.*, 2011, **27**, 58–67.

26    K. Schilling, B. Bradford, D. Castelli, E. Dufour, J. F. Nash, W. Pape, S. Schulte, I. Tooley, J. Van Den Bosch and F. Schellauf, *Photochem. Photobiol. Sci.*, 2010, **9**, 495–509.

27    U. Osterwalder and B. Herzog, *Br. J. Dermatol.*, 2009, **161**, 13–24.

28    L. Konermann, E. Ahadi, A. D. Rodriguez and S. Vahidi, *Anal. Chem.*, 2013, **85**, 2–9.

29    J. B. Fenn, *Angew. Chemie Int. Ed.*, 2003, **42**, 3871–3894.

30    W. M. . Niessen and A. . Tinke, *J. Chromatogr. A*, 1995, **703**, 37–57.

31    A. Kulyyassov, M. Fresnais and R. Longuespée, *Proteomics*, 2021, 2100153.

32    A. Pafili, T. Meikopoulos, E. Kontogiannidou, S. Papageorgiou, E. Demiri, D. Meimari, D. G. Fatouros, H. Gika and G. Theodoridis, *J. Chromatogr. B*, 2021, **1167**, 122561.

33    B. Herzog, J. Giesinger and V. Settels, *Photochem. Photobiol. Sci.*, 2020, **19**, 1636–1649.

34    F. Jentzsch, O. Olsson, J. Westphal, M. Reich, C. Leder and K. Kümmerer, *Sci. Total Environ.*, 2016, **572**, 1092–1100.

35    K. T. N. Nguyen, C. Scapolla, M. Di Carro and E. Magi, *Talanta*, 2011, **85**, 2375–2384.

36    E. Uliyanchenko, S. van der Wal and P. J. Schoenmakers, *Polym. Chem.*, 2012, **3**, 2313.

37    P. Gago-Ferrero, M. S. Díaz-Cruz and D. Barceló, *Anal. Methods*, 2013, **5**, 355–366.

38   M. S. Scarpin, C. M. Kawakami, K. C. Rangel, K. de C. Pereira, C. G. Benevenuto and L. R. Gaspar, *Photochem. Photobiol.*, 2021, php.13407.

39   N. G. K. Wong, J. A. Berenbeim, M. Hawkridge, E. Matthews and C. E. H. Dessent, *Phys. Chem. Chem. Phys.*, 2019, **21**, 14311–14321.

40   N. G. K. Wong, J. A. Berenbeim and C. E. H. Dessent, *ChemPhotoChem*, 2019, **3**, 1231–1237.

41   J. A. Berenbeim, N. G. K. Wong, M. C. R. Cockett, G. Berden, J. Oomens, A. M. Rijs and C. E. H. Dessent, *J. Phys. Chem. A*, 2020, **124**, 2919–2930.

42   J. A. Berenbeim, N. G. K. Wong, M. C. R. Cockett, G. Berden, J. Oomens, A. M. Rijs and C. E. H. Dessent, *Phys. Chem. Chem. Phys.*, 2020, **22**, 19522–19531.

43   N. G. K. Wong, C. D. Rankine and C. E. H. Dessent, *J. Phys. Chem. Lett.*, 2021, **12**, 2831–2836.

44   N. G. K. Wong, C. D. Rankine and C. E. H. Dessent, *J. Phys. Chem. A*, 2021, **125**, 6703–6714.

45   T. N. V. Karsili, B. Marchetti, M. N. R. Ashfold and W. Domcke, *J. Phys. Chem. A*, 2014, **118**, 11999–12010.

46   T. T. Abiola, A. L. Whittock and V. G. Stavros, *Molecules*, 2020, **25**, 3945.

47   P. Widsten, *Cosmetics*, 2020, **7**, 1–8.

48   D. Piccinino, E. Capecchi, E. Tomaino, S. Gabellone, V. Gigli, D. Avitabile and R. Saladino, *Antioxidants*, 2021, **10**, 274.

49   Y. Qian, X. Qiu and S. Zhu, *ACS Sustain. Chem. Eng.*, 2016, **4**, 4029–4035.

50   S. C. Lee, E. Yoo, S. H. Lee and K. Won, *Polymers (Basel).*, 2020, **12**, 699.

51   J. Luo, Y. Liu, S. Yang, A. L. Flourat, F. Allais and K. Han, *J. Phys. Chem. Lett.*, 2017, **8**, 1025–1030.

52   L. A. Baker, M. Staniforth, A. L. Flourat, F. Allais and V. G. Stavros, *ChemPhysChem*, 2020, **21**, 2006–2011.

53   M. Dole, R. L. Hines, L. L. Mack, R. C. Mobley, L. D. Ferguson and M. B. Alice, *Macromolecules*, 1968, **1**, 96–97.

54   S. Banerjee and S. Mazumdar, *Int. J. Anal. Chem.*, 2012, **2012**, 1–40.

55   P. Kebarle and U. H. Verkerk, *Mass Spectrom. Rev.*, 2009, **28**, 898–917.

56   J. V. Iribarne, *J. Chem. Phys.*, 1976, **64**, 2287.

57   M. Wilm, *Mol. Cell. Proteomics*, 2011, **10**, M111.009407.

58   W. Paul, *Angew. Chemie Int. Ed. English*, 1990, **29**, 739–748.

59   P. Gates, Quadrupole Mass Analysis, http://www.chm.bris.ac.uk/ms/quadrupole.xhtml, (accessed 2 November 2021).

60   N. V. Konenkov, M. Sudakov and D. J. Douglas, *J. Am. Soc. Mass Spectrom.*,

2002, **13**, 597–613.

61    amaZon Series User Manual Revision 1 Bruker Daltonics, 2009.

62    E. Matthews, A. Sen, N. Yoshikawa, E. Bergström and C. E. H. Dessent, *Phys. Chem. Chem. Phys.*, 2016, **18**, 15143–15152.

63    R. B. Cody, R. C. Burnier and B. S. Freiser, *Anal. Chem.*, 1982, **54**, 96–101.

64    R. A. Zubarev and A. Makarov, *Anal. Chem.*, 2013, **85**, 5288–5296.

65    R. H. Perry, R. G. Cooks and R. J. Noll, *Mass Spectrom. Rev.*, 2008, **27**, 661–699.

66    J. Y. Xie, Y. H. Yeung, C. K. Kwok, K. Kei, P. Ang, L. L. Chan, C. C. Cheang, W. Chow and J.-W. Qiu, *Mar. Pollut. Bull.*, 2020, **153**, 110950.

67    R. Danovaro, L. Bongiorni, C. Corinaldesi, D. Giovannelli, E. Damiani, P. Astolfi, L. Greci and A. Pusceddu, *Environ. Health Perspect.*, 2008, **116**, 441–447.

68    K. M. Hanson, S. Narayanan, V. M. Nichols and C. J. Bardeen, *Photochem. Photobiol. Sci.*, 2015, **14**, 1607–1616.

69    Y. Peperstraete, M. Staniforth, L. A. Baker, N. D. N. Rodrigues, N. C. Cole-Filipiak, W.-D. Quan and V. G. Stavros, *Phys. Chem. Chem. Phys.*, 2016, **18**, 28140–28149.

70    N. Serpone, A. Salinaro, A. V. Emeline, S. Horikoshi, H. Hidaka and J. Zhao, *Photochem. Photobiol. Sci.*, 2002, **1**, 970–981.

71    S. Pattanaargson, T. Munhapol, P. Hirunsupachot and P. Luangthongaram, *J. Photochem. Photobiol. A Chem.*, 2004, **161**, 269–274.

72    V. Lhiaubet-Vallet, M. Marin, O. Jimenez, O. Gorchs, C. Trullas and M. A. Miranda, *Photochem. Photobiol. Sci.*, 2010, **9**, 552.

73    L. A. MacManus-Spencer, M. L. Tse, J. L. Klein and A. E. Kracunas, *Environ. Sci. Technol.*, 2011, **45**, 3931–3937.

74    S. Pattanaargson and P. Limphong, *Int. J. Cosmet. Sci.*, 2001, **23**, 153–160.

75    P. B. Armentrout, *J. Am. Soc. Mass Spectrom.*, 2002, **13**, 419–434.

76    R. Cercola, K. C. Fischer, S. L. Sherman, E. Garand, N. G. K. Wong, L. A. Hammerback, J. M. Lynam, I. J. S. Fairlamb and C. E. H. Dessent, *Chem. – A Eur. J.*, 2020, **26**, 10297–10306.

77    S. Kinoshita, Y. Harabuchi, Y. Inokuchi, S. Maeda, M. Ehara, K. Yamazaki and T. Ebata, *Phys. Chem. Chem. Phys.*, 2021, **23**, 834–845.

78    S. Muramatsu, S. Nakayama, S. Kinoshita, Y. Onitsuka, H. Kohguchi, Y. Inokuchi, C. Zhu and T. Ebata, *J. Phys. Chem. A*, 2020, **124**, 1272–1278.

79    N. G. K. Wong, C. Rhodes and C. E. H. Dessent, *Molecules*, 2021, **26**, 6009.

80    J. Zelenka and J. Roithová, *ChemBioChem*, 2020, **21**, 2232–2240.

81    J. Mehara and J. Roithová, *Chem. Sci.*, 2020, **11**, 11960–11972.

82    R. Cercola, N. G. K. Wong, C. Rhodes, L. Olijnyk, N. S. Mistry, L. M. Hall, J. A. Berenbeim, J. M. Lynam and C. E. H. Dessent, *RSC Adv.*, 2021, **11**, 19500–19507.

83    M. Pahl, M. Mayer, M. Schneider, D. Belder and K. R. Asmis, *Anal. Chem.*, 2019, **91**, 3199–3203.

84    C. R. Sung, K.-B. Kim, J. Y. Lee, B.-M. Lee and S. J. Kwack, *Toxicol. Res.*, 2019, **35**, 131–136.

85    V. . Sakkas, D. . Giokas, D. . Lambropoulou and T. . Albanis, *J. Chromatogr. A*, 2003, **1016**, 211–222.

86    M. Pedrouzo, F. Borrull, R. M. Marcé and E. Pocurull, *J. Chromatogr. A*, 2009, **1216**, 6994–7000.

87    E. Magi, C. Scapolla, M. Di Carro, P. Rivaro and K. T. Ngoc Nguyen, *Anal. Methods*, 2013, **5**, 428–433.

88    P. Calza, D. Vione, F. Galli, D. Fabbri, F. Dal Bello and C. Medana, *Water Res.*, 2016, **88**, 235–244.

89    W. Studziński, A. Gackowska and E. Kudlek, *J. Hazard. Mater.*, 2021, **403**, 123856.

90    İ. Sıdır and Y. G. Sıdır, *J. Mol. Liq.*, 2018, **249**, 1161–1171.

91    C. Xu, X. Zeng, Z. Yang and H. Ji, *Polymers (Basel).*, 2021, **13**, 866.

92    V. Gabelica, E. De Pauw and M. Karas, *Int. J. Mass Spectrom.*, 2004, **231**, 189–195.

93    M. J. Van Stipdonk, M. P. Ince, B. A. Perera and J. A. Martin, *Rapid Commun. Mass Spectrom.*, 2002, **16**, 355–363.

94    A. J. Ingram, C. L. Boeser and R. N. Zare, *Chem. Sci.*, 2016, **7**, 39–55.

95    A. Guesmi, L. Ohlund and L. Sleno, *Rapid Commun. Mass Spectrom.*, , DOI:10.1002/rcm.8679.

96    H. V. Stein, C. J. Berg, J. N. Maung, L. E. O'Connor, A. E. Pagano, L. A. Macmanus-Spencer and M. G. Paulick, *Environ. Sci. Process. Impacts*, 2017, **19**, 851–860.

97    E. Damiani, P. Astolfi, J. Giesinger, T. Ehlis, B. Herzog, L. Greci and W. Baschong, *Free Radic. Res.*, 2010, **44**, 304–312.

98    A. A. Andrianova, T. DiProspero, C. Geib, I. P. Smoliakova, E. I. Kozliak and A. Kubátová, *J. Am. Soc. Mass Spectrom.*, 2018, **29**, 1044–1059.

99    J. C. Dean, P. Navotnaya, A. P. Parobek, R. M. Clayton and T. S. Zwier, *J.*

*Chem. Phys.*, , DOI:10.1063/1.4824019.

100  J. D. Young, M. Staniforth, J. C. Dean, G. M. Roberts, F. Mazzoni, T. N. V. Karsili, M. N. R. Ashfold, T. S. Zwier and V. G. Stavros, *J. Phys. Chem. Lett.*, 2014, **5**, 2138–2143.

101  T. A. Gawargy, B. Wang and J. C. Scaiano, *Photochem. Photobiol.*, , DOI:10.1111/php.13520.

102  M. Dubois, P. Gilard, P. Tiercet, A. Deflandre and M. A. Lefebvre, *J. Chim. Phys. Physico-Chimie Biol.*, 1998, **95**, 388–394.

103  G. J. Mturi and B. S. Martincigh, *J. Photochem. Photobiol. A Chem.*, , DOI:10.1016/j.jphotochem.2008.09.007.

104  N. Rajendiran and T. Balasubramanian, *Spectrochim. Acta Part A Mol. Biomol. Spectrosc.*, , DOI:10.1016/j.saa.2007.04.035.

105  B. Wang, D. Sun, H.-M. Wang, T.-Q. Yuan and R.-C. Sun, *ACS Sustain. Chem. Eng.*, 2019, **7**, 2658–2666.

106  H. Lambers, S. Piessens, A. Bloem, H. Pronk and P. Finkel, *Int. J. Cosmet. Sci.*, 2006, **28**, 359–370.

107  K. Kulthanan, P. Nuchkull and S. Varothai, *Asia Pac. Allergy*, 2013, **3**, 155.

108  J. Wang, Y. Deng, Y. Qian, X. Qiu, Y. Ren and D. Yang, *Green Chem.*, 2016, **18**, 695–699.

109  H. Li, Y. Deng, H. Wu, Y. Ren, X. Qiu, D. Zheng and C. Li, *Holzforschung*, 2016, **70**, 725–731.